Inkjet printing: bubble entrainment and satellite formation

Arjan Fraters

INKJET PRINTING: BUBBLE ENTRAINMENT AND SATELLITE FORMATION

Arjan Fraters

Samenstelling promotiecommissie:

Prof. dr. ir. J.W.M. Hilgenkamp (voorzitter)	Universiteit Twente
Prof. dr. A.M. Versluis (promotor)	Universiteit Twente
Prof. dr. rer. nat. D. Lohse (promotor)	Universiteit Twente
Dr. T.J. Segers (assistent promotor)	Universiteit Twente
Prof. dr. J.C.T. Eijkel	Universiteit Twente
Dr. E.S. Kooij	Universiteit Twente
Prof. dr. ir. J. van der Gucht	Wageningen Universiteit
Prof. dr. ir. H.M.A. Wijshoff	Technische Universiteit Eindhoven & Océ Technologies B.V.
Dr. M. van den Berg	Océ Technologies B.V.
Ir. H. Reinten	Océ Technologies B.V.

The work in this thesis was carried out at the Physics of Fluids group of the Faculty of Science and Technology of the University of Twente, and at Océ Technologies B.V.. It is part of the research program ”High Tech Systems and Materials” (HTSM) with project number 12802, and part of the Industrial Partnership Program number i43, of the Dutch Technology Foundation (STW) and the Foundation for Fundamental Research on Matter (FOM), which are part of the Netherlands Organisation for Scientific Research (NWO). The research was co-financed by Océ Technologies B.V., University of Twente, and Eindhoven University of Technology.

Nederlandse titel:
Inkjet printen: invanging van bellen en vorming van satellieten

Publisher:
Arjan Fraters, Physics of Fluids, University of Twente,
P.O. Box 217, 7500 AE Enschede, The Netherlands
pof.tnw.utwente.nl

Cover design: Arjan Fraters
Printed by: Gildeprint - Enschede

ISBN: 978-90-365-4664-5 DOI: 10.3990/1.9789036546645

INKJET PRINTING: BUBBLE ENTRAINMENT AND SATELLITE FORMATION

PROEFSCHRIFT

ter verkrijging van
de graad van doctor aan de Universiteit Twente,
op gezag van de rector magnificus,
Prof. dr. T.T.M. Palstra,
volgens besluit van het College voor Promoties
in het openbaar te verdedigen
op vrijdag 21 december 2018 om 16.45 uur

door

Arjan Bernard Fraters
geboren op 21 november 1987
te Wageningen

Dit proefschrift is goedgekeurd door de promotoren:

Prof. dr. A.M. Versluis

en

Prof. dr. rer. nat. D. Lohse

en de assistent promotor:

Dr. T.J. Segers

Contents

1
Introduction

1.1 Piezo inkjet printing

Inkjet printing [1–4] is the art of depositing ink droplets in a controlled and precise manner at predefined locations on a substrate without being in direct contact with the substrate. It allows for on-demand personalized printing. The main categories in inkjet printing are continuous inkjet and drop-on-demand (DOD) inkjet. The first method creates a constant stream of droplets, of which some are used for printing, and the others are electrostatically deflected towards an ink recycling system. The second method produces a single droplet on demand. The latter method is less complicated because it does not need a droplet deflection system and ink recycling system.

The two main methods within DOD inkjet are thermal inkjet and piezo inkjet. They differ in the method by which they produce the pressure pulse to drive the droplet formation at the nozzle. Thermal inkjet uses a vapor bubble created by a heating element, while piezo inkjet uses a piezoelectric element that deforms when an electrical pulse is provided. The first method is more common in low-end printers because of the lower production costs, while the second method is more common in high-end printers because of its higher reliability, and because it is not restricted to inks that are compatible with the heating mechanism.

Piezo inkjet is used for industrial printing of documents, graphic art, and packaging. Typical ink types that are used in these applications are water-based and solvent-based inks, that solidify by drying through evaporation, hotmelt inks, that solidify by crystallization through cooling, and UV inks, that solidify by curing through exposure to ultraviolet (UV) light. Piezo inkjet is also used in additive manufacturing of for example electronics [5–13], pharmaceutics [14], and biomaterials [15–18]. During the continuous development of the piezo inkjet printing process to jet smaller droplet at faster rates, technical and physical limitations are being encountered, including bubble entrainment and satellite droplet formation. To overcome or avoid such limitations a good understanding of the underlying physics is required. For the encountered limitations related to fluid dynamics the research topics stretch from the printhead to the substrate, including ink channel acoustics, bubble entrainment, droplet formation, droplet in flight, droplet-substrate and droplet-droplet interaction, and droplet evaporation. This thesis focusses on bubble entrainment and on droplet formation, which will be further introduced in the next two sections. The last section gives an overview of the research that was done in this thesis on these two topics.

1.2 Bubble Entrainment

The entrainment of air bubbles into the ink channel is a well-known, but not fully understood phenomenon [19–26]. Bubbles are entrained at the nozzle, and are forced into oscillation by the acoustic pressure waves generated by the piezo. The bubbles move into the ink channel and towards the wall due to acoustic radiation forces, through the primary- and secondary Bjerkness force [27–31]. Furthermore, they grow by rectified diffusion [28–30, 32]. The bubbles on their part affect the pressure field at the nozzle entrance and thereby disrupt the droplet formation process, and as such reduce print quality.

The main open question is as follows: by what physical mechanisms can bubbles get entrained? It was shown before that dirt particles and an ink layer flowing on the nozzle plate can trigger bubble entrainment by disturbing the droplet formation process at the nozzle exit [19]. However, it was found that bubble entrainment can still occur, even when dirt particles and ink are prevented from reaching a jetting nozzle, e.g. by using an anti-wetting coating on the nozzle plate.

The working hypothesis at the start of this project was that a Rayleigh-Taylor instability [33, 34] or a parametrically driven capillary instability [35] on the meniscus is responsible for the unexplained bubble entrainment events. This hypothesis finds its roots in the finding that the likelihood of air entrainment increases with stronger driving and a higher drop-on-demand frequency. The first step required in understanding the unexplained entrainment process is experimental visualization. To date, this has not been done because of three challenges that need to be tackled simultaneously. First, because the entrainment process takes place at the microsecond time scale and micrometer length scale, high-speed imaging at frame rates ranging from 1 Mfps to 10 Mfps is required in combination with microscopic imaging and powerful illumination. Second, because the high speed cameras work in the visible light range, the nozzle needs to be optically accessible to visible light, which is not the case for commercial printheads. Finally, because the bubble entrainment process behind the unexplained bubble entrainment events is stochastic in nature, a real-time monitoring system is required that triggers the high-speed camera upon the occurrence of the bubble entrainment event.

1.3 Droplet formation

Fig 1.1 shows a typical droplet formation process from a nozzle of an experimental printhead described in Chapter 4. During piezo actuation the ink is first retracted into the nozzle and then pushed out of the nozzle. A head droplet forms on the emerging jet, which is connected to the meniscus at the nozzle exit through what is called its primary tail. Towards pinch-off a neck develops between the meniscus and the primary tail, and this neck is stretched into a thinner tail, a secondary tail [36–38]. When such a secondary tail breaks up, it may produce femtoliter-sized droplets that pollute the printing machine. To minimize this type of pollution, a good understanding of the secondary tail formation process and its breakup is required. However, this process is experimentally challenging as the smaller length-scales reach the diffraction limit.

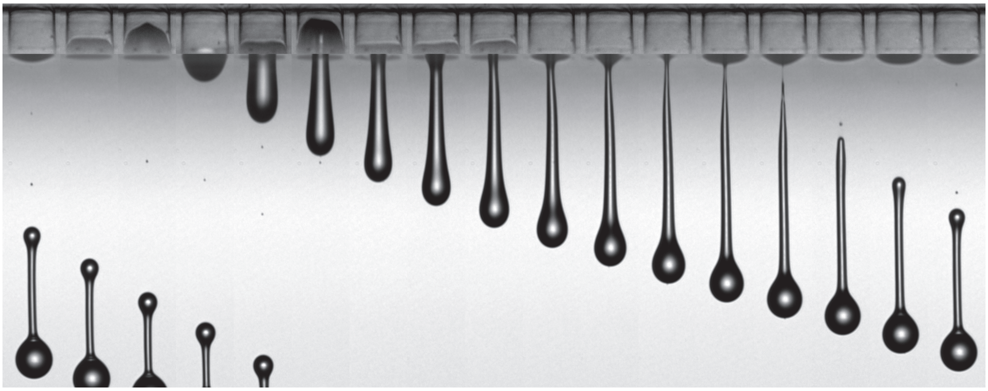

Figure 1.1: Droplet formation from a 30 µm diameter nozzle of the experimental printhead described in Chapter 4. Recorded using 8 ns single-flash stroboscopic imaging with illumination by laser-induced fluorescence (iLIF) [37]. The nozzle and the droplet were imaged at a different focal distance during separate recordings, and were stitched together in this image. Thus, each image of the nozzle and each image of a droplet shows a different droplet formation.

1.4 Guide through the thesis

The first three chapters of this thesis concern bubble entrainment, while the last chapter describes secondary tail formation. Chapter 2 presents a bubble pinch-off mechanism in a printhead from Microdrop Technologies, that is deterministic in nature and occurs only for some specific piezo actuation settings. The process prior to pinch-off was imaged in detail using stroboscopic imaging with iLIF, and the driving mechanism behind this process was revealed by numerical simulations using a boundary integral method. Chapter 3 presents a short-wave infrared imaging setup that is capable of visualizing the ink channels of a Micro-Electro-Mechanical-System (MEMS) printhead. This system revealed details of multiple entrained air bubbles from shortly after entrainment to fully grown state. In Chapter 4 the stochastic bubble entrainment mechanism is visualized for the first time in a silicon-based printhead. For this purpose an experimental printhead was produced consisting of a silicon-based functional acoustic part and a fused silica nozzle plate chip. A monitoring system was used to trigger the high speed camera upon changes in the channel acoustics due to bubble entrainment. In the second but last chapter, 5, the secondary tail formation and breakup are studied by comparing the secondary tail length and the satellite size distributions for a range of piezo driving conditions and ink viscosities. The thesis end with conclusions and a general outlook to future work (Chapter 6).

References

[1] H. Wijshoff, “The dynamics of the piezo inkjet printhead operation”, Physics Reports **491**, 77–177 (2010).

[2] J. Castrejon-Pita, W. Baxter, J. Morgan, S. Temple, G. Martin, and I. Hutchings, “Future, opportunities and challenges of inkjet technologies”, Atomization and Sprays **23**, 541–565 (2013).

[3] C. Ru, J. Luo, S. Xie, and Y. Sun, “A review of non-contact micro- and nano-printing technologies”, Journal of Micromechanics and Microengineering **24**, 053001 (2014).

[4] S. D. Hoath, *Fundamentals of Inkjet Printing: The Science of Inkjet and Droplets* (Wiley-VCH Verlag GmbH & Co. KGaA) (2015).

[5] S. Majee, M. Song, S.-L. Zhang, and Z.-B. Zhang, “Scalable inkjet printing of shear-exfoliated graphene transparent conductive films”, Carbon **102**, 51–57 (2016).

[6] S. Majee, C. Liu, B. Wu, S.-L. Zhang, and Z.-B. Zhang, “Ink-jet printed highly conductive pristine graphene patterns achieved with water-based ink and aqueous doping processing”, Carbon **114**, 77–83 (2017).

[7] S. Eshkalak, A. Cinnappan, W. Jayathilaka, M. Khatibzadeh, E. Kowsari, and S. Ramakrishna, “A review on inkjet printing of CNT composites for smart applications”, Applied Materials Today **9**, 372–386 (2017).

[8] M. Vilardell, X. Granados, S. Ricart, I. V. Driessche, A. Palau, T. Puig, and X. Obradors, “Flexible manufacturing of functional ceramic coatings by inkjet printing”, Thin Solid Films **548**, 489–497 (2013).

[9] A. Moya, G. Gabriel, R. Villa, and F. J. del Campo, “Inkjet-printed electrochemical sensors”, Current Opinion in Electrochemistry **3**, 29–39 (2017).

[10] T. Eggenhuisen, Y. Galagan, E. Coenen, W. Voorthuijzen, M. Slaats, S. Kommeren, S. Shanmuganam, M. Coenen, R. Andriessen, and W. Groen, “Digital fabrication of organic solar cells by inkjet printing using non-halogenated solvents”, Solar Energy Materials and Solar Cells **134**, 364–372 (2015).

[11] S. Hashmi, M. Ozkan, J. Halme, K. Misic, S. Zakeeruddin, J. Paltakari, M. Grätzel, and P. Lund, “High performance dye-sensitized solar cells with inkjet printed ionic liquid electrolyte”, Nano Energy **17**, 206–215 (2015).

[12] T. Shimoda, K. Morii, S. Seki, and H. Kiguchi, “Inkjet printing of light-emitting polymer displays”, Inkjet Printing of Functional Materials **28**, 821–827 (2003).

[13] C. Jiang, L. Mu, J. Zou, Z. He, Z. Zhong, L. Wang, M. Xu, J. Wang, J. Peng, and Y. Cao, “Full-color quantum dots active matrix display fabricated by ink-jet printing”, Science China Chemistry **60**, 1349–1355 (2017).

[14] R. Daly, T. Harrington, G. Martin, and I. Hutchings, “Inkjet printing for pharmaceutics - a review of research and manufacturing”, International Journal of Pharmaceutics **494**, 554–567 (2015).

[15] A. Simaite, F. Mesnilgrente, B. Tondu, P. Souères, and C. Bergaud, “Towards inkjet printable conducting polymer artifical muscles”, Sensors and Actuators B: Chemical **229**, 425–433 (2016).

[16] S. Hewes, A. Wong, and P. Searson, “Bioprinting microvessels using and inkjet printer”, Bioprinting **7**, 14–18 (2017).

[17] M. Nakamura, A. Kobayashi, F. Takagi, A. Watanabe, Y. Hiruma, K. Ohuchi, Y. Iwasaki, M. Horie, I. Morita, and S. Takatani, “Biocompatible inkjet printing technique for designed seeding of individual living cells”, Tissue Engineering **11**, 1658–1666 (2005).

[18] G. Villar, A. Graham, and H. Bayley, “A tissue-like printed material”, Science **340**, 48–52 (2013).

[19] J. de Jong, G. de Bruin, H. Reinten, M. van den Berg, H. Wijshoff, M. Versluis, and D. Lohse, “Air entrapment in piezo-driven inkjet printheads”, Journal of the Acoustical Society of America **120**, 1257–1265 (2006).

[20] J. de Jong, R. Jeurissen, H. Borel, M. van den Berg, H. Wijshoff, H. Reinten, M. Versluis, A. Prosperetti, and D. Lohse, “Entrapped air bubbles in piezo-driven inkjet printing: their effect on the droplet velocity”, Physics of Fluids **18**, 121511 (2006).

[21] R. Jeurissen, J. de Jong, H. Reinten, M. van den Berg, H. Wijshoff, M. Versluis, and D. Lohse, “Effect of an entrained air bubble on the acoustics of an ink channel”, Journal of the Acoustical Society of America **123**, 2496–2505 (2008).

[22] R. Jeurissen, A. van der Bos, H. Reinten, M. van den Berg, H. Wijshoff, J. de Jong, M. Versluis, and D. Lohse, “Acoustic measurement of bubble size in an inkjet printhead”, Journal of the Acoustical Society of America **126**, 2184–2190 (2009).

[23] S. Lee, D. Kwon, and Y. Choi, “Dynamics of entrained air bubbles inside a piezodriven inkjet printhead”, Applied Physics Letters **95**, 221902 (2009).

[24] B.-H. Kim, T.-G. Kim, T.-K. Lee, S. Kim, S.-J. Shin, S.-J. Kim, and S.-J. Lee, “Effects of trapped air bubbles on frequency responses of the piezo-driven inkjet printheads and visualization of the bubbles using synchrotron X-ray”, Sensors and Actuators A: Physical **154**, 132–139 (2009).

[25] R. Jeurissen, H. Wijshoff, M. van den Berg, H. Reinten, and D. Lohse, “Regimes of bubble volume oscillations in a pipe”, Journal of the Acoustical Society of America **130**, 3220–3232 (2011).

[26] A. van der Bos, T. Segers, R. Jeurissen, M. van den Berg, H. Reinten, H. Wijshoff, M. Versluis, and D. Lohse, “Infrared imaging and acoustic sizing of a bubble inside a micro-electro-mechanical system piezo ink channel”, Journal of Applied Physics **110**, 034503 (2011).

[27] L. Crum, “Bjerknes forces on bubbles in a stationary sound field”, Journal of the Acoustical Society of America **57**, 1363–1370 (1975).

[28] T. Leighton, *The Acoustic Bubble* (Academic Press) (1994).

[29] C. Brennen, *Cavitation and Bubble Dynamics* (Oxford University Press, New York) (1995).

[30] M. Brenner, S. Hilgenfeldt, and D. Lohse, “Single-bubble sonoluminescence”, Reviews of Modern Physics **74**, 425–484 (2002).

[31] V. Garbin, B. Dollet, M. Overvelde, D. Cojoc, E. D. Fabrizio, L. van Wijngaarden, A. Prosperetti, N. de Jong, D. Lohse, and M. Versluis, “History force on coated microbubbles propelled by ultrasound”, Physics of Fluids **21**, 092003 (2009).

[32] L. Crum, “Rectified diffusion”, Ultrasonics **22**, 215–223 (1984).

[33] Rayleigh, “Investigation of the character of the equilibrium of an incompressible heavy fluid of variable density”, Proceedings of the London Mathematical Society **14**, 170–177 (1883).

[34] G. Taylor, “The instability of liquid surfaces when accelerated in a direction perpendicular to their planes. i”, Proceedings of the Royal Society of London A **201**, 192–196 (1950).

[35] M. Faraday, “On a peculiar class of acoustical figures; and on certain forms assumed by groups of particles upon vibrating elastic surfaces”, Philosophical Transactions of the Royal Society of London **121**, 299–340 (1831).

[36] H. Wijshoff, “Drop formation mechanisms in piezo-acoustic inkjet”, Proceedings Nanotech 2007 **3**, 448–451 (2007).

[37] A. van der Bos, A. Zijlstra, E. Gelderblom, and M. Versluis, “iLIF: illumination by laser-induced fluorescence for single flash imaging on a nanoseconds timescale”, Experiments in Fluids **51**, 1283–1289 (2011).

[38] A. van der Bos, M.-J. van der Meulen, T. Driessen, M. van den Berg, H. Reinten, H. Wijshoff, M. Versluis, and D. Lohse, “Velocity profile inside piezoacoustic inkjet droplets in flight: comparison between experiment and numerical simulation”, Physical Review Applied **1**, 014004 (2014).

2

Bubble pinch-off from an acoustically driven meniscus in a piezo drop-on-demand inkjet nozzle *

In piezo-acoustic drop-on-demand (DOD) inkjet printing a single droplet is produced for each piezo driving pulse. A phenomenon that may disturb the droplet formation process is the entrainment of bubbles in the ink channel. Here, bubble pinch-off from an acoustically driven meniscus in a DOD printhead was studied for various acoustic driving waveforms. The piezo actuation pulse sets into motion a slosh mode of the printhead, resulting in a large amplitude meniscus motion with a frequency on the order of 10 kHz. It also actuates a piezo longitudinal resonance mode, which introduces a low-amplitude 100 kHz component to the meniscus motion. The slosh mode, piezo longitudinal resonance mode, and the falling edge of the rectangular piezo driving pulse destabilize the retracted concave meniscus when propelled outward, by jet formation due to a combination of geometrical focusing of the flow and an inhomogeneous pressure gradient field. Two well-timed outward accelerations of the meniscus result in the formation of a central jet surrounded by a toroidal jet. A phase mismatch of the oscillatory behavior of the two jets leads to the enclosure of an air cavity leading to bubble entrainment through pinch-off. It is shown that, next to pulse timing, the driving pressure is a control parameter of the entrainment process

---

[*] To be submitted as: Arjan Fraters, Maaike Rump, Tim Segers, Roger Jeurissen, Marc van den Berg, Youri de Loore, Hans Reinten, Herman Wijshoff, Detlef Lohse, and Michel Versluis, ”Bubble pinch-off from an acoustically driven meniscus in a piezo drop-on-demand inkjet nozzle”.

and that the threshold for bubble pinch-off can be increased by suppressing the piezo longitudinal resonance mode by waveform design.

2.1 Introduction

Piezo inkjet printing [1, 2] is an accurate and contactless method to deposit ink droplets on a substrate. Droplets are formed on-demand from a nozzle by actuating a piezoelectric element. The piezo deforms the channel wall upon electrical stimulation, resulting in acoustic pressure waves that jet the ink out of the nozzle. Piezo inkjet printing is used in high-end industrial printers for on-demand personalized printing of documents, graphic art, and packaging. It is used for these applications because of its high reliability, high print quality, and its compatibility with a wide range of inks. The aforementioned properties make piezo inkjet printing also an excellent technique for several emerging additive manufacturing applications such as printing electronics [3–11], pharmaceutics [12], and biomaterials [13–16].

Piezo inkjet printing is a highly reliable droplet deposition technique, however, the droplet formation process is sometimes compromised by the entrainment of air bubbles [17–24]. The entrained air bubbles disturb or even stop the jetting process and thereby dramatically reduce the printing quality and reliability. Previously it has been found that dirt particles or an ink layer on the nozzle plate can trigger bubble entrainment by disturbing the jetting process at the nozzle exit [17]. However, bubbles can also be entrained without the presence of dirt particles or an ink layer, i.e. by another physical mechanism. Figure 2.1 shows such a bubble pinch-off event that was observed in a squeeze type piezo inkjet printhead with a 70 µm diameter nozzle exit (Microdrop Technologies GmbH, Autodrop Pipette AD-K-501), driven by a rectangular push-pull pulse (amplitude: 150 V, width: 30 µs). First, a droplet is ejected, and subsequently, the meniscus retracts back into the nozzle and a bubble pinches off when the meniscus motion reverses from an inward motion, toward the ink channel, to an outward motion, away from the ink channel. The bubble pinch-off event is shown in more detail in Fig. 2.1(b). The figure shows that the central region of the meniscus moves inward while the outer region of the meniscus moves outward. As a result, an air cavity forms that eventually closes, thereby pinching off an air bubble.

Bubble pinch-off as shown in Fig. 2.1 was only observed to occur within certain windows of the piezo operating range. This is illustrated in Fig. 2.2, where two examples of a bubble pinch-off window are given for a rectangular pull-push pulse with amplitude A and width Δt (Fig. 2.2(a)). In the first example in Fig. 2.2(b), the pulse amplitude A was varied with all other parameters fixed. A window of bubble pinch-off was observed between pulse amplitudes of 140 V and 150 V. Given the nature of meniscus instabilities, meaning that the growth time shortens and the oscillation amplitude increases with increasing acceleration [25–27], it was expected that bubble

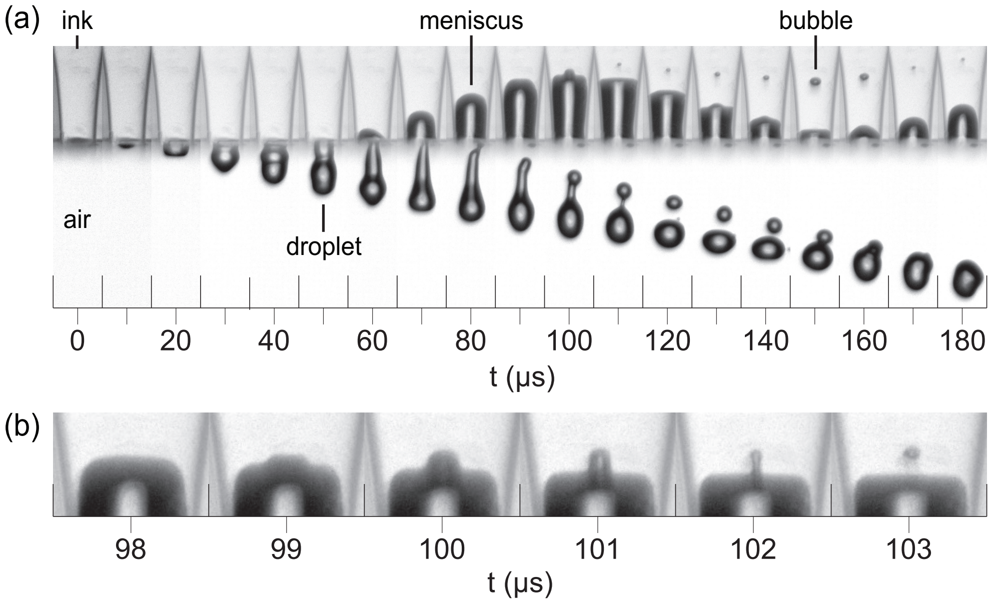

Figure 2.1: (a) Bubble pinch-off and entrainment in a 70 μm diameter nozzle of a piezo drop-on-demand inkjet printhead. The piezo actuation pulse was a rectangular push-pull pulse with a 150 V amplitude and a 30 μs width. The images were recorded using 8 ns single-flash stroboscopic imaging with illumination by laser-induced fluorescence (iLIF) [28] (b) Details of the bubble pinch-off process: The center of the meniscus moves inwards while the outer region of the meniscus moves outward, leading to the formation of an air cavity that eventually pinches off.

pinch-off would always occur above a certain threshold amplitude. Surprisingly, no bubble pinch-off was observed at amplitudes larger than 160 V. In the second example, see Fig. 2.2(c), the pulse width was varied. Bubble pinch-off was observed between pulse widths of 70 μs and 75 μs. The bubble size initially increases and then decreases, with a maximum radius between 72 μs and 73 μs. The observed bubble pinch-off phenomena may indicate resonance behavior or positive interference of acoustic waves.

An oscillating meniscus can be destabilized by several mechanisms, including the classical Rayleigh-Taylor instability [25, 26] and the parametrically driven meniscus instability [27, 29]. A Rayleigh-Taylor instability grows on a flat interface between two fluids with different density, i.e. the ink and air. The two fluids are accelerated into one another at a rate high enough such that the inertial forces overcome the restoring surface tension. The parametrically driven meniscus instability grows on an initially flat meniscus at the subharmonic of the frequency at which the meniscus is driven

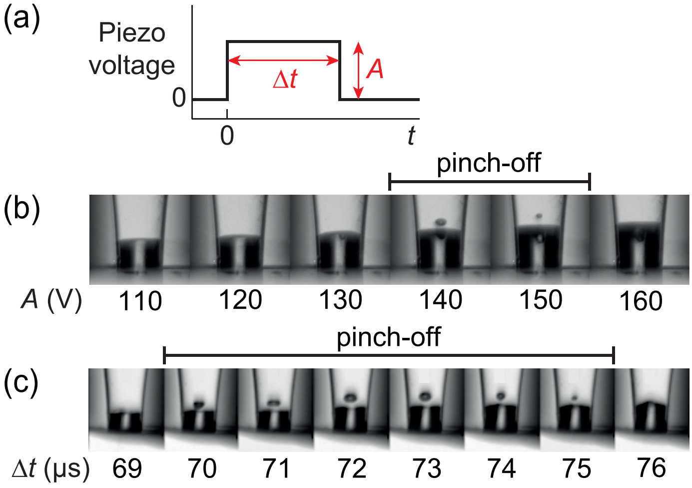

Figure 2.2: (a) Rectangular piezo actuation pulse with its amplitude A and length Δt as the control parameters. Window of bubble pinch-off for (b) a pull-push pulse with a pulse width of 30 μs and a varying amplitude, and (c) a pull-push pulse with an amplitude of 94 V and a varying pulse width.

(period doubling). The meniscus can also be destabilized at intermediate Ohnesorge number by an inhomogeneous velocity field at the meniscus due to the finite transport time of viscous-drag-induced vorticity from the wall to the center of the nozzle [30]. Finally, the meniscus can be destabilized by an inhomogeneous pressure gradient field in combination with geometrical focusing of flow when a concave meniscus is propelled forward [31]. It is difficult to say a priori which of these mechanisms drives bubble pinch-off as observed in Fig. 2.1 because they are all capable of producing a meniscus shape similar to the one in Fig. 2.1(b).

The goal of the present study is to find the underlying physical mechanisms that drive bubble pinch-off as observed in Figs. 2.1 and 2.2, and to gain fundamental insight into the stability of an acoustically driven meniscus. To that end, the meniscus and bubble dynamics shown in Fig. 2.1 are analyzed in more detail by tracking the meniscus position over time. The acoustic driving of the meniscus by the piezo actuator is further characterized by measuring the piezo ring-down signal. Then, the meniscus dynamics of two other experiments are analyzed to identify the process during which the inner and outer region of the meniscus develop their destabilizing out-of-phase motion. Finally, the mechanisms that drive the development of this out-of-phase motion are identified using numerical simulations with the Boundary Integral (BI) method.

2.2 Experimental and numerical methods

2.2.1 Printhead and ink

A 70 µm nozzle diameter Autodrop Pipette from Microdrop Technologies GmbH (AD-K-501 and AD-H-501) was used, see Fig. 2.3(a). Figure 2.3(b) shows the approximate inner dimensions of the functional acoustic part of the printhead. More details about this type printhead can be found in refs. [32, 33].

A 4:1 (v/v) mixture of water with glycerol (Sigma-Aldrich, G9012, 1,2,3-Propanetriol, $\geq$99.5%) was used as a model ink. All experiments were performed at room temperature. The density, viscosity, and surface tension were estimated from literature to be 1050 kg/m^3, 2.1 mPa·s, and 71 mN/m, respectively [34, 35]. The model ink was supplied from a plastic syringe to the top of the Autodrop Pipette holder via flexible plastic PEEK tubing (Upchurch Scientific), and the meniscus was positioned at the nozzle exit by manually adjusting the piston of the syringe.

2.2.2 Imaging setup

Bubble pinch-off was recorded using a stroboscopic imaging setup, see Fig. 2.3(a). The microscope (Olympus) had a 5× objective (LMPLFLN5x), a tube lens (U-TLU), and a high-resolution CCD camera (Lumenera, Lw135m, 1392×1040 pixels, 4.65 µm pixel size). The resulting optical resolution was 0.93 µm/pixel. The images captured by the camera were saved by custom-made software on a Personal Computer (PC) programmed in the graphical programming language Labview (National Instruments).

The tip of the Autodrop Pipette was illuminated by incoherent 8 ns illumination pulses with a wavelength of 577 nm from a Laser-Induced Fluorescence (iLIF) system [28]. The iLIF system consisted of a pulsed laser (Quantel EverGreen, dual cavity Nd:YAG, λ= 532 nm, 7 ns), a fluorescent plate embedded in a highly efficient diffuser (Lavision, part nr. 1108417 and 1003144), and a lens to condense the light pulses onto the imaging plane of the microscope.

2.2.3 Measurement procedure

A programmable pulse-delay generator (Berkeley Nucleonics Corp., BNC 575) triggered the laser, the camera, and the printhead actuation system with nanosecond precision. The jetting process was kept reproducible by jetting the entrained bubble outward after each bubble pinch-off event. To do so, the piezo was actuated by rectangular pulses from two arbitrary waveform generators: one waveform generator (Agilent 33220A, 20 MHz, 14 bit, 50 MSa/s) produced one high amplitude pulse to entrain an air bubble, and the other waveform generator (Wavetek 195, 16 MHz, 12 bit, 40 MSa/s) produced successively 49 low amplitude pulses to jet the entrained air bubbles out of the nozzle. For every actuation cycle, a custom-made Labview

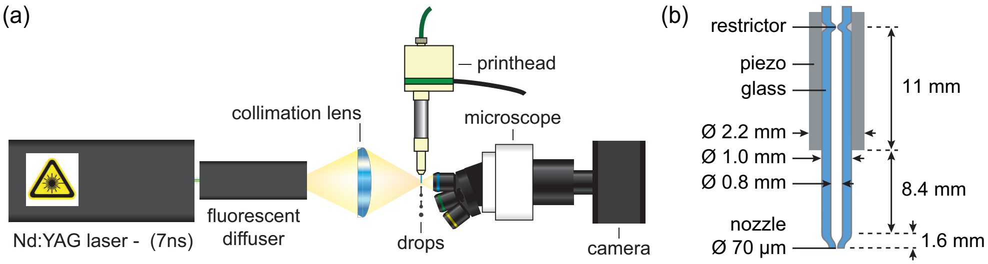

Figure 2.3: (a) Setup to image bubble pinch-off in the drop-on-demand piezo-acoustic inkjet nozzle, using illumination by laser-induced fluorescence (iLIF) [28]. (b) Schematic layout of the functional acoustic part of the inkjet nozzle.

program captured one image during the high-amplitude piezo actuation pulse. The timing of image exposure was controlled by varying the delay of the laser flash with respect to the start of the piezo driving pulse. The delay was varied over a range from 0 μs to 200 μs with steps of 1 μs to capture the complete drop formation and bubble pinch-off process. A laboratory amplifier (Falco System WMA-300, 5 MHz, 2000 V/μs) amplified the pulses from the waveform generators by a factor of 50. Given the 5 MHz amplifier bandwidth, the rise- and fall time of the rectangular pulses was 0.2 μs. The rectangular piezo driving pulses had an amplitude between 0 V and 160 V, and the printhead could be driven in either the push-pull mode or pull-push mode by switching the polarity of the electrical connections at the printhead. With the complete system, droplets were produced with diameters in the range of 70 μm to 100 μm, corresponding to volumes of 180 pL to 520 pL, and droplet velocities in the range of 1 m/s to 3 m/s.

2.2.4 Image analysis

The motion of the meniscus and that of the bubble were tracked as a function of time. First the contrast in each image was enhanced using ImageJ (http://imagej.nih.gov/ij) by subtracting the original image from the image taken at $t = 0$ μs, and by adding the inverted result to the original image. Second, the edges of the meniscus and bubble were detected using a script programmed in Python (Python Software Foundation, https://www.python.org/). The script applied a Scikit-Image Canny Edge Detector to each image, extracted the edges of interest, and calculated its positions. The meniscus was separated in an inner and outer region to quantify the meniscus shape deformation, see Fig. 2.4. The inner region was chosen such that it always confined the bubble, and had a width of 0.6 times the nozzle diameter. The outer region was set to a width of 0.9 times the nozzle diameter. The position of the outer region of the meniscus y_o was the average position of the detected edge in that region. The position of the inner

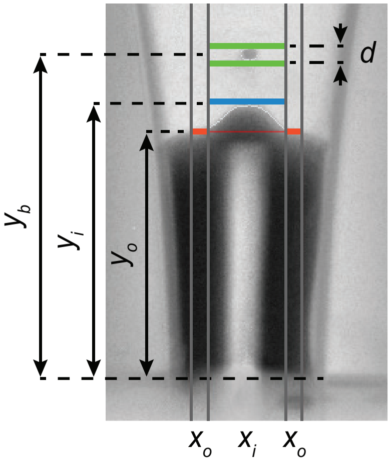

Figure 2.4: Example of an image analysis result, showing the meniscus positions y_o of the outer region x_o and y_i of inner region x_i, the bubble position y_b, and the bubble diameter d.

region of the meniscus y_i was the maximum or minimum position of the detected edge in that region depending on whether it had a concave or convex shape, respectively. When a bubble was present, its center position y_b and diameter d were determined. The bubble diameter was only measured in axial direction to minimize the error in the bubble radius due to the refraction of light at the cylindrical walls of the glass nozzle. The time dependent y_o, y_i, and y_b were filtered to extract the amplitudes and dynamics of the low- and high-frequency components of the meniscus motion.

2.2.5 Piezo eigenfrequency characterization through ring-down measurements

To characterize the eigenfrequency of the piezo, the ring-down of the piezo was measured using a piezo sensing technique described in refs. [1, 17]. The piezo was set into motion using an electrical pulse. Subsequently, the piezo was connected to an oscilloscope that recorded the oscillations in the voltage across the piezo resulting from the piezo deformation during the ring-down oscillations.

2.2.6 Boundary Integral simulations

To study the bubble pinch-off process and the underlying physical mechanisms in greater detail, Boundary Integral (BI) simulations were performed [31]. The utilized BI code is axisymmetric, and assumes irrotational, incompressible, and inviscid flow [36–39]. The inviscid assumption is appropriate here as in the experiments it was observed that the meniscus shape deformation is the largest at low viscosity, and decreases as the ink viscosity increases. The numerical setup consisted of a nozzle wall (solid boundary), and a meniscus (free boundary). The flow in the nozzle was driven by applying a stream velocity boundary condition to the nodes at the entrance of the nozzle.

Two methods were used sequentially to describe the contact line dynamics of the meniscus; a fixed contact line, and a moving contact line based on contact angle hysteresis with a receding contact angle θ_r and an advancing contact angle θ_a. Combining these two methods provided a good balance between approximating the experimentally observed meniscus motion and preventing fatal instabilities on the meniscus due to numerical instabilities. These occurred when the distance between the free boundary and solid boundary became too small. At the start of each simulation the contact line was kept pinned. If during this first time period one of the nodes of the meniscus came within a distance from the wall that would cause numerical instability, the meniscus between that node and the contact line was cut off, and a new contact line was created near this node. This intervention did not have a significant effect on bubble pinch-off process in the simulation results that are presented here. Once the contact angle became larger than θ_a the moving contact line method was initiated. This method keeps the contact line pinned for $\theta_r < \theta < \theta_a$; moves the contact line to $\theta = \theta_r$ if $\theta < \theta_r$, and it moves the contact line to $\theta = \theta_a$ when $\theta > \theta_a$. θ_r and θ_a were set to the maximum angle away from 90° for which the meniscus motion near the wall remained stable during the simulations, i.e. $\theta_r = 72^\circ$ and $\theta_a = 108^\circ$. At larger angles away from 90° numerical instabilities would develop on the meniscus because of the too small distance between the free boundary and the solid boundary, as before.

2.3 Results

2.3.1 Meniscus and bubble dynamics

The data shown in Fig. 2.1 is now analyzed in more detail. Figure 2.5(a) shows the position of the outer and inner region of the meniscus (y_o, y_i) and that of the bubble (y_b) as a function of time. Note that just before pinch-off a phase difference $\Delta\phi$ develops between the inner and outer region of the meniscus. This is the crucial opposing motion between the central cavity and the outer region of the meniscus that leads to bubble pinch-off, as was observed in Fig. 2.1(b). The process that is responsible for this phase difference is analysed in Section 2.3.3. Also note in Fig. 2.5(a) that both the meniscus position curve and the bubble position curve have a high-amplitude low-frequency motion of the order of 10 kHz (100 µs period, resulting from the slosh mode [33]) with superimposed a low-amplitude high-frequency motion of the order of 100 kHz (10 µs period). The low-frequency motion of the meniscus and bubble are indicated by the dashed curve and by the dash-dotted curve, respectively.

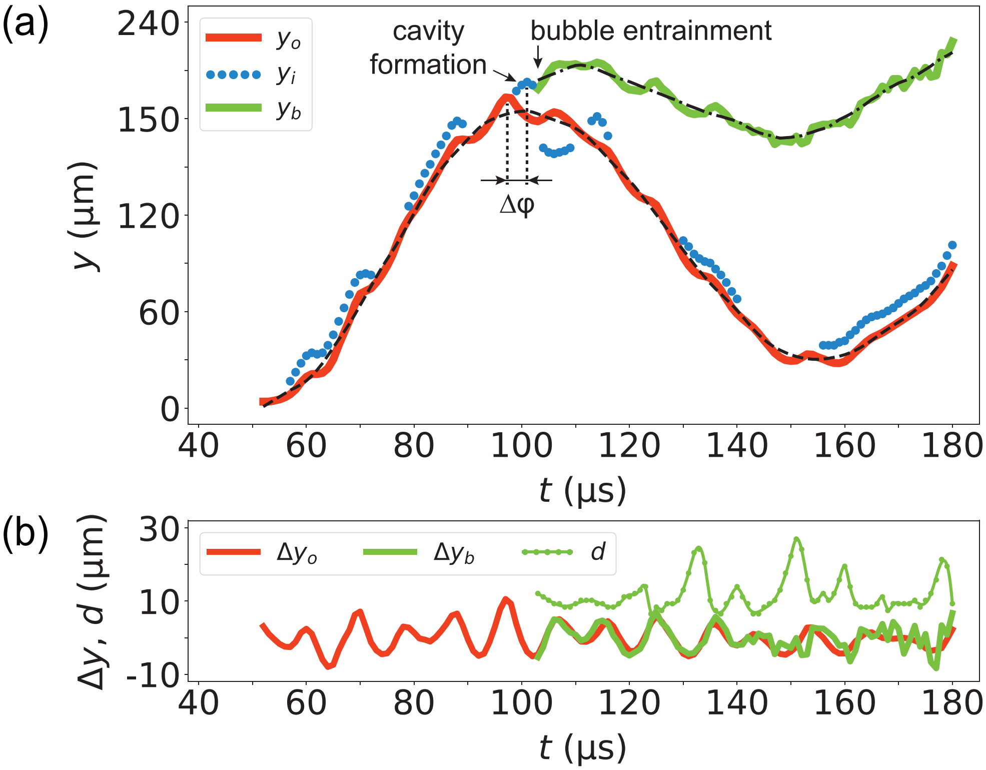

Figure 2.5: (a) Meniscus outer y_o and inner y_i positon, and bubble position y_b as function of time after the tart of piezo actuation. The black dashed line and the black dash-dotted line show the low-frequency motion of the meniscus outer region and that of the bubble, respectively. (b) High-frequency movement of the meniscus outer region position Δy_o and that of the bubble position Δy_b. Furthermore, the bubble diameter d is given as function of time.

The high-frequency component in the meniscus motion Δy_o and that of the bubble motion Δy_b are plotted in Fig. 2.5(b). In addition, in Fig. 2.5(b) the bubble diameter d is plotted as function of time. The bubble equilibrium radius was 5 ±1 µm, which corresponds to a Minneart eigenfrequency [40] of approx. 0.6 MHz. As this is much higher than the observed bubble oscillation frequency of 0.1 MHz, the radial dynamics of the bubble were considered to oscillate in phase with that of the acoustic pressure waves inside the ink channel [41]. Therefore, the bubble radius directly represents the channel acoustics, i.e. the maximum in bubble radius corresponds to a minimum pressure, and vice versa. Note in Fig 2.5(b) that the bubble diameter, the bubble position, and the meniscus position all oscillate at a frequency of 105 ±5 kHz. Also note that the meniscus and bubble are moving inward around the time that the bubble diameter is maximum (pressure minimum), while the meniscus and bubble start moving outward when the bubble diameter is minimum (pressure maximum). Thus, the meniscus and the bubble are driven by the same high-frequency pressure waves, and not by their individual eigenmodes.

2.3.2 Acoustic driving by the piezo

To determine whether the piezo actuator is the origin of the high-frequency pressure oscillations, the eigenmodes of the piezo were characterized by measuring the ring-down signal of the piezo for an empty ink channel. The piezo was first actuated using a pull-push pulse with an amplitude A of 10 V, a FWHM pulse width Δt of 72 µs, and a rise- and fall time Δe of 1 µs, see Fig. 2.6(a). The ring-down signal and its Fourier spectrum are plotted in Fig. 2.6(b) and 2.6(c). Indeed, in the ring-down signal the same 105 kHz high-frequency component was present as in the meniscus motion, bubble motion, and radial dynamics in Fig. 2.5(b). The piezo eigenmode frequencies were calculated to be 111 ±12 kHz in longitudinal direction and 3.4 ±0.1 MHz in radial direction [42, 43]. Thus, the 105 kHz high-frequency component in the piezo ring-down signal originated from the longitudinal resonance mode of the piezo, and the pressure waves produced by this resonance mode drive the high-frequency motion of the meniscus in the nozzle. Indeed, when the high-frequency component is suppressed by using a Δe of 9 µs, see Fig. 2.6(b) and 2.6(c), also the high-frequency motion of the meniscus is suppressed, see Fig. 2.6(d).

Notably, the absence of the 105 kHz high-frequency pressure waves also prevents bubble pinch-off, see Fig. 2.6(f) in comparison to Fig. 2.6(e). In the experiment shown in Fig. 2.6(f) an air cavity was still formed, but it did not pinch off. This cavity could be forced to pinch-off in the same way as before, but at a different position and time, by increasing the amplitude of the piezo driving to 120 V, see Fig. 2.6(g). Thus, suppressing the high-frequency pressure waves effectively increased the threshold for bubble pinch-off from 95 V to 120 V. In other words, the high-frequency pressure waves from the longitudinal resonance mode of the piezo promote bubble pinch-off,

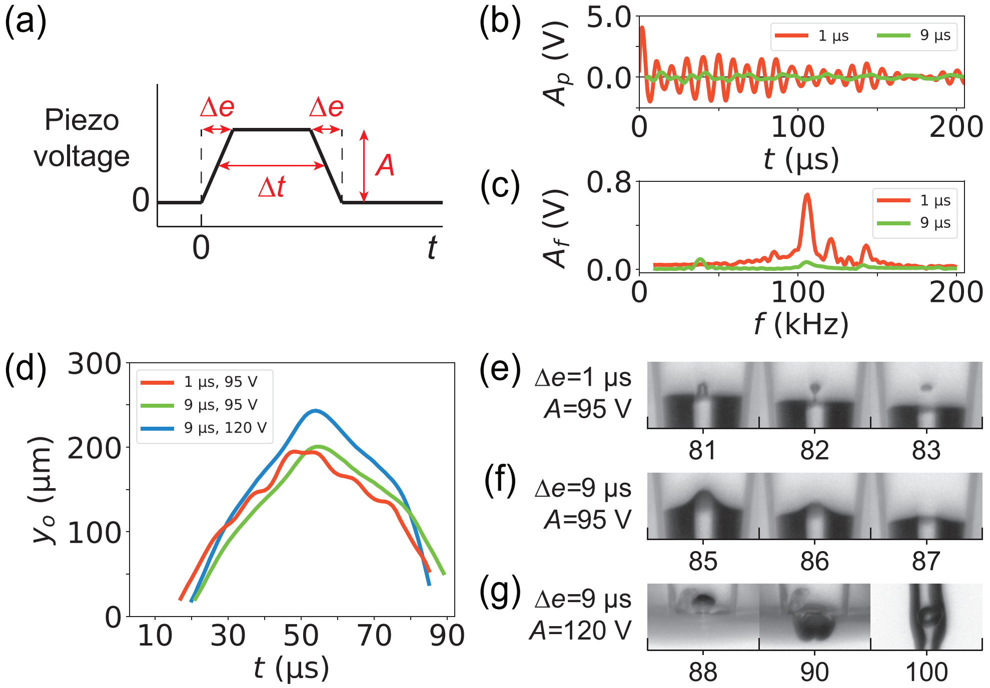

Figure 2.6: (a) Piezo actuation pulse with amplitude A, FWHM pulse width Δt, and rise- and fall time Δe. (b) Piezo ring-down measurements with (c) the corresponding Fourier spectra, for a pull-push pulse with A = 10 V, Δt = 72 μs, and values of Δe as indicated in the legend. (d) Meniscus motion for three pulses with a Δt of 72 μs, and with Δe and A as given in the legend. (e, f, g) Images of the nozzle for the measurements in (d), showing whether or not bubble pinch-off took place.

but are not an absolutely essential ingredient to the observed pinch-off phenomenon. Nevertheless, through suppression of the 105 kHz waves, the driving amplitude can be increased, which allows for stable inkjet printing at a higher droplet velocity.

2.3.3 Meniscus shape deformation process

Now that the driving mechanisms of the meniscus are identified, next the process responsible for the development of the phase difference between the inner and outer region of meniscus, eventually leading to bubble pinch-off, can be identified. The phase difference $\Delta\phi$ (Fig. 2.5(a)) develops through the meniscus shape deformation process that can be observed in Fig 2.7: it develops by jet formation at a concave meniscus. The universality of the meniscus shape deformation process prior to bubble pinch-off is demonstrated in Fig. 2.7 by its presence in two bubble pinch-off experiments with entirely different driving conditions, i.e. with piezo driving pulses with opposite polarity. In the first experiment the piezo was actuated using a rectangular push-pull pulse (A= 160 V, Δt = 30 μs). A bubble was entrained after droplet formation, and it remained inside the nozzle, see Fig. 2.7(a). In the second experiment the piezo was actuated using a rectangular pull-push pulse (A = 150 V, Δt = 30 μs). In contrast to the first experiment, a bubble was entrained before droplet formation, and it was ejected with the droplet shortly after entrainment, see Fig. 2.7(b). Despite the large differences between the two experiments, the image sequences and graphs in Fig. 2.7(c-f) show that the meniscus shape deformation process is qualitatively the same for the two experiments. Initially, upon retraction, the meniscus has a concave shape. Then, during the advancing of the meniscus, a liquid jet is formed in outward direction. Later, this jet recoils back inward, while the outer region of the meniscus is forced to move outward again, in the opposite direction of the movement of the jet. Similar to the experiment in Fig. 2.1, the opposing motion of the outer and inner region of the meniscus leads to the formation and closure of a cavity, and thereby to the pinch-off of a bubble. Thus, the phase difference between the inner and outer region of the meniscus is a consequence of jet formation at the central part of the concave meniscus.

2.3.4 Jet formation mechanism

The mechanism by which the observed jets are formed is now identified. From literature it is known that when a pressure wave propels a concave-shaped meniscus forward, a jet forms due to geometrical focusing of the flow at the meniscus and due to an inhomogeneous pressure gradient field along the meniscus [31]. The pressure gradient and resulting velocity are larger at the center of a concave meniscus than at its edge, see also ref. [44]. Thus, in the inkjet nozzle, first, the inward motion of ink results in a concave shaped meniscus, then, a first outward acceleration creates a

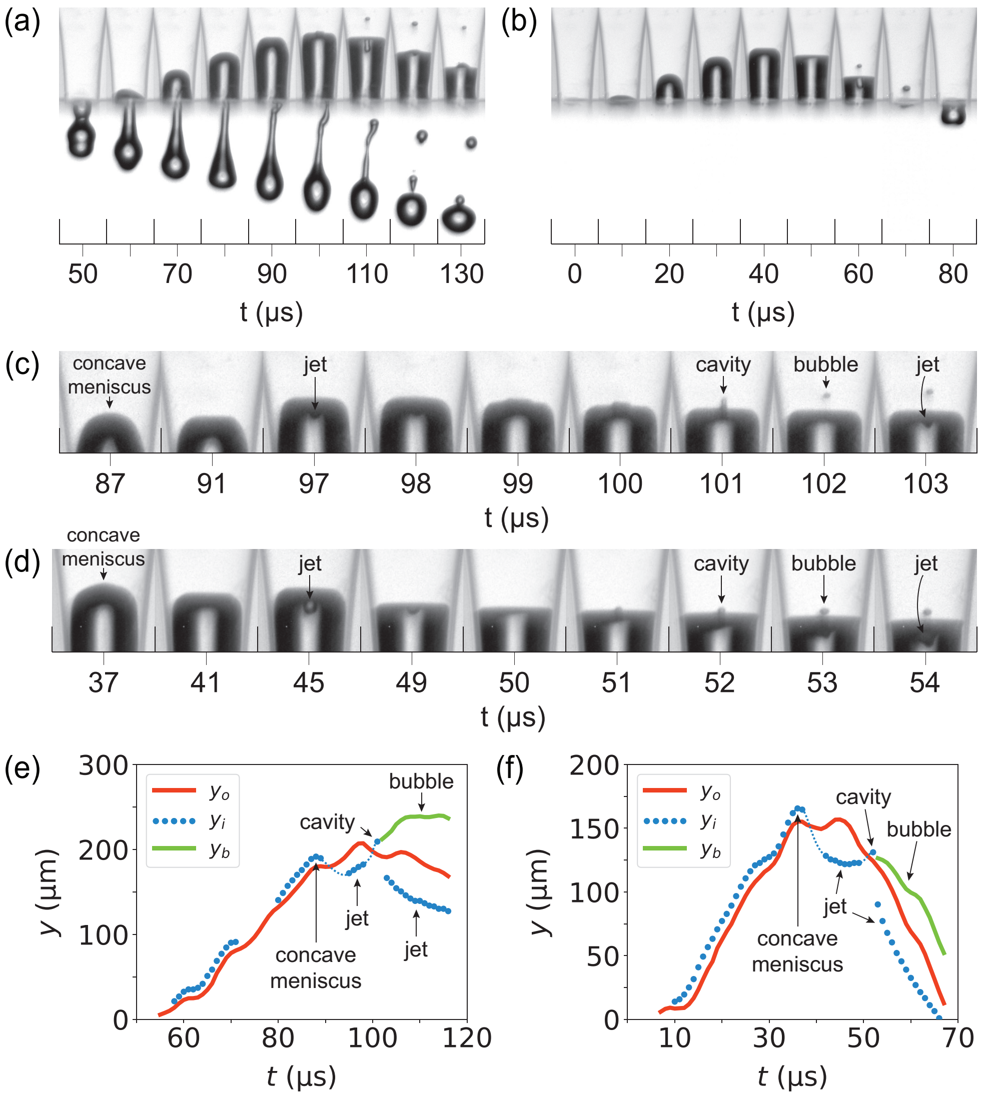

Figure 2.7: Bubble pinch-off for (a) a rectangular push-pull pulse with an amplitude of 160 V and a width of 30 μs, and (b) a rectangular pull-push pulse with an amplitude of 150 V and a width of 30 μs. (c, d) Details of the meniscus shape deformation process prior to, during, and after bubble pinch-off for the push-pull and the pull-push pulse, respectively. (e, f) Meniscus outer region position y_o, inner region position y_i, and bubble position y_b as function of time for the push-pull and pull-push pulse, respectively. The thin red dashed line was added to guide the eye in the parts of the jet formation and jet recoil process were the position of the inner region of the meniscus could not be tracked.

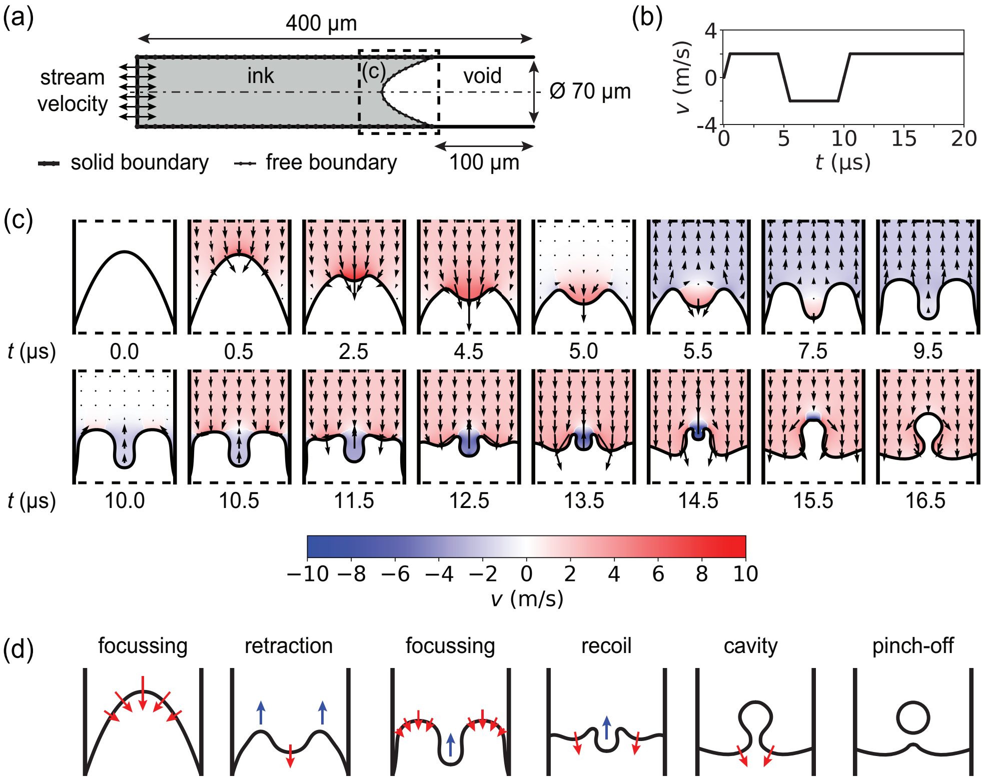

Figure 2.8: (a) Numerical setup for the Boundary Integral (BI) simulation. The initial meniscus shape is a parabola with a depth of 0.75 times the nozzle diameter. (b) Stream velocity boundary condition v for the numerical setup as function of time, mimicing a 100 kHz pressure oscillation, followed by an outward directed flow. (c) Meniscus shape deformation process prior to bubble pinch-off, simulated using the BI method. (d) Schematic summary of the main steps in (c).

phase difference between the inner and outer region of the meniscus by the formation of a central outward-moving liquid jet, and, finally, a well-timed second outward acceleration enhances this phase difference by the formation of a toroidal outward-moving liquid jet. The central liquid jet recoils inward and forms an air cavity that is enclosed by the toroidal outward-moving liquid jet, and as a consequence, a bubble pinches off.

To further demonstrate the details of the proposed pinch-off mechanism, numerical simulations were performed using the boundary integral (BI) method. The results are shown in Fig. 2.8. The geometry of the numerical setup in Fig. 2.8(a), and the stream velocity boundary condition v in Fig. 2.8(b), were chosen such that they follow the experimental conditions. The simulation results in Fig. 2.8(c) reveal the amplitude and the direction of the ink velocity, and they demonstrate how the velocity field inhomogeneity and the focusing of the flow at the concave part of the meniscus drive jet formation. Moreover, the results highlight the opposing motion between the central jet and the toroidal jet, and show in detail how this opposing motion leads to the formation of a cavity that closes and pinches off a bubble. The main steps in this process, which were discussed in detail before, are now schematically summarized in Fig. 2.8(d): a central jet forms at the concave meniscus during the first outward acceleration. Then a toroidal jet forms at the concave meniscus around the central jet during the second outward acceleration. The recoiling central jet forms a cavity, and the progressing toroidal jet encloses this cavity, with bubble pinch-off as a result.

2.4 Discussion

The experiments and simulations have revealed a mechanism by which bubbles can pinch-off from an acoustically driven meniscus in a piezo inkjet nozzle. The acquired knowledge about the underlying physics makes it possible to globally explain the observed parameter windows of bubble pinch-off in Fig. 2.2. In Fig. 2.2(b) the pulse width Δt was fixed and the amplitude A was varied. At an amplitude of 130 V and lower, the velocity difference between the recoiling central jet and the progressing toroidal jet was not high enough to form a sufficiently deep cavity at the right moment in time and to enclose this cavity. At an amplitude of 160 V the central jet had such a length and inertia that it was too slow to recoil before the toroidal jet reached the central axis. As a result the toroidal jet enclosed the base of the central jet, which in multiple experiments and simulations has been observed to result in formation of a toroidal bubble (data not presented here). In Fig. 2.2(c) A was fixed, and Δt was varied. In other words, the control parameter in these experiments was the timing of the outward acceleration of the meniscus by the falling edge of the piezo driving pulse. In the experiments shown in Fig. 2.2(c) the central jet had already been formed before the falling edge of the pulse. At the different times of meniscus acceleration, the meniscus shape was different, and thus the toroidal jet formation process was different. At $\Delta t = 69$ μs the acceleration was too early, i.e. the central jet was not able to develop sufficient opposing motion with respect to the toroidal jet because of its early formation. At $\Delta t = 76$ μs acceleration was too late, i.e. the meniscus was propelled outward while the cavity was already present, thus, the central cavity was propelled outward faster than the outer region of the meniscus.

Despite the acquired knowledge on the underlying physics of the bubble pinch-off mechanism, it remains difficult to predict where exactly in the piezo driving parameter space bubble pinch-off will occur. The main two reasons for this are the sensitivity of the mechanism to the operating conditions and the unavailability of information about the exact printhead dimensions and its acoustic properties, which is required for accurate modelling of the acoustic driving of the meniscus. However, bubble pinch-off can be suppressed with relative ease by suppressing the high-frequency component in the acoustics through the edge duration of the piezo driving pulse. Another simple and effective method, which was not discussed here, is to damp out the meniscus shape deformations by increasing the ink viscosity. However, this requires higher driving amplitudes to produce droplets at equal velocity and reduces the universal applicability of the technique.

2.5 Conclusion

An acoustically driven meniscus in a piezo inkjet nozzle can pinch off an air bubble under specific driving conditions. Pinch-off is the result of the closure of a central air cavity in the meniscus that forms due to opposing motion between a central region and an outer region of the meniscus. The physical mechanism responsible for bubble pinch-off was investigated. By analyzing the meniscus-, bubble-, and piezo dynamics, it was found that the meniscus is mainly driven by the edges of the piezo driving pulse, the slosh mode of the printhead with a frequency on the order of 10 kHz, and the piezo longitudinal resonance mode with a frequency on the order of 100 kHz. Furthermore, it was found that the opposing motion between the central region and outer region of the meniscus is the result of jet formation at the concave meniscus. When the concave shaped meniscus is propelled forward, a jet forms as a result of geometrical focusing of the flow at the concave meniscus, and as a result of an inhomogeneous pressure gradient field along the meniscus, which was confirmed by Boundary Integral simulations. Hence, the process that is responsible for the bubble pinch-off can be summarized as follows: the meniscus gains a concave shape due to inward motion. Then, a first outward acceleration produces a central jet at the concave meniscus. A well-timed second outward acceleration produces a toroidal jet at the concave meniscus around the central jet. The recoiling central jet forms a central air cavity while the progressing toroidal jet encloses this air cavity. Eventually this leads to pinch-off of an air bubble. These results help gaining fundamental understanding of the stability of an acoustically driven meniscus in an inkjet printhead and thereby provide ways to increase the stability of inkjet printing.

References

[1] H. Wijshoff, “The dynamics of the piezo inkjet printhead operation”, Physics Reports **491**, 77–177 (2010).

[2] S. D. Hoath, *Fundamentals of Inkjet Printing: The Science of Inkjet and Droplets* (Wiley-VCH Verlag GmbH & Co. KGaA) (2015).

[3] S. Majee, M. Song, S.-L. Zhang, and Z.-B. Zhang, “Scalable inkjet printing of shear-exfoliated graphene transparent conductive films”, Carbon **102**, 51–57 (2016).

[4] S. Majee, C. Liu, B. Wu, S.-L. Zhang, and Z.-B. Zhang, “Ink-jet printed highly conductive pristine graphene patterns achieved with water-based ink and aqueous doping processing”, Carbon **114**, 77–83 (2017).

[5] S. Eshkalak, A. Cinnappan, W. Jayathilaka, M. Khatibzadeh, E. Kowsari, and S. Ramakrishna, “A review on inkjet printing of CNT composites for smart applications”, Applied Materials Today **9**, 372–386 (2017).

[6] M. Vilardell, X. Granados, S. Ricart, I. V. Driessche, A. Palau, T. Puig, and X. Obradors, “Flexible manufacturing of functional ceramic coatings by inkjet printing”, Thin Solid Films **548**, 489–497 (2013).

[7] A. Moya, G. Gabriel, R. Villa, and F. J. del Campo, “Inkjet-printed electrochemical sensors”, Current Opinion in Electrochemistry **3**, 29–39 (2017).

[8] T. Eggenhuisen, Y. Galagan, E. Coenen, W. Voorthuijzen, M. Slaats, S. Kommeren, S. Shanmuganam, M. Coenen, R. Andriessen, and W. Groen, “Digital fabrication of organic solar cells by inkjet printing using non-halogenated solvents”, Solar Energy Materials and Solar Cells **134**, 364–372 (2015).

[9] S. Hashmi, M. Ozkan, J. Halme, K. Misic, S. Zakeeruddin, J. Paltakari, M. Grätzel, and P. Lund, “High performance dye-sensitized solar cells with inkjet printed ionic liquid electrolyte”, Nano Energy **17**, 206–215 (2015).

[10] T. Shimoda, K. Morii, S. Seki, and H. Kiguchi, “Inkjet printing of light-emitting polymer displays”, Inkjet Printing of Functional Materials **28**, 821–827 (2003).

[11] C. Jiang, L. Mu, J. Zou, Z. He, Z. Zhong, L. Wang, M. Xu, J. Wang, J. Peng, and Y. Cao, “Full-color quantum dots active matrix display fabricated by ink-jet printing”, Science China Chemistry **60**, 1349–1355 (2017).

[12] R. Daly, T. Harrington, G. Martin, and I. Hutchings, “Inkjet printing for pharmaceutics - a review of research and manufacturing”, International Journal of Pharmaceutics **494**, 554–567 (2015).

[13] A. Simaite, F. Mesnilgrente, B. Tondu, P. Souères, and C. Bergaud, “Towards inkjet printable conducting polymer artifical muscles”, Sensors and Actuators B: Chemical **229**, 425–433 (2016).

[14] S. Hewes, A. Wong, and P. Searson, “Bioprinting microvessels using and inkjet printer”, Bioprinting **7**, 14–18 (2017).

[15] M. Nakamura, A. Kobayashi, F. Takagi, A. Watanabe, Y. Hiruma, K. Ohuchi, Y. Iwasaki, M. Horie, I. Morita, and S. Takatani, “Biocompatible inkjet printing technique for designed seeding of individual living cells”, Tissue Engineering **11**, 1658–1666 (2005).

[16] G. Villar, A. Graham, and H. Bayley, “A tissue-like printed material”, Science **340**, 48–52 (2013).

[17] J. de Jong, G. de Bruin, H. Reinten, M. van den Berg, H. Wijshoff, M. Versluis, and D. Lohse, “Air entrapment in piezo-driven inkjet printheads”, Journal of the Acoustical Society of America **120**, 1257–1265 (2006).

[18] J. de Jong, R. Jeurissen, H. Borel, M. van den Berg, H. Wijshoff, H. Reinten, M. Versluis, A. Prosperetti, and D. Lohse, “Entrapped air bubbles in piezo-driven inkjet printing: their effect on the droplet velocity”, Physics of Fluids **18**, 121511 (2006).

[19] R. Jeurissen, J. de Jong, H. Reinten, M. van den Berg, H. Wijshoff, M. Versluis, and D. Lohse, “Effect of an entrained air bubble on the acoustics of an ink channel”, Journal of the Acoustical Society of America **123**, 2496–2505 (2008).

[20] R. Jeurissen, A. van der Bos, H. Reinten, M. van den Berg, H. Wijshoff, J. de Jong, M. Versluis, and D. Lohse, “Acoustic measurement of bubble size in an inkjet printhead”, Journal of the Acoustical Society of America **126**, 2184–2190 (2009).

[21] S. Lee, D. Kwon, and Y. Choi, “Dynamics of entrained air bubbles inside a piezodriven inkjet printhead”, Applied Physics Letters **95**, 221902 (2009).

[22] B.-H. Kim, T.-G. Kim, T.-K. Lee, S. Kim, S.-J. Shin, S.-J. Kim, and S.-J. Lee, “Effects of trapped air bubbles on frequency responses of the piezo-driven inkjet printheads and visualization of the bubbles using synchrotron X-ray”, Sensors and Actuators A: Physical **154**, 132–139 (2009).

[23] R. Jeurissen, H. Wijshoff, M. van den Berg, H. Reinten, and D. Lohse, “Regimes of bubble volume oscillations in a pipe”, Journal of the Acoustical Society of America **130**, 3220–3232 (2011).

[24] A. van der Bos, T. Segers, R. Jeurissen, M. van den Berg, H. Reinten, H. Wijshoff, M. Versluis, and D. Lohse, “Infrared imaging and acoustic sizing of a bubble inside a micro-electro-mechanical system piezo ink channel”, Journal of Applied Physics **110**, 034503 (2011).

[25] Rayleigh, “Investigation of the character of the equilibrium of an incompressible heavy fluid of variable density”, Proceedings of the London Mathematical Society **14**, 170–177 (1883).

[26] G. Taylor, “The instability of liquid surfaces when accelerated in a direction perpendicular to their planes. i”, Proceedings of the Royal Society of London A **201**, 192–196 (1950).

[27] M. Faraday, “On a peculiar class of acoustical figures; and on certain forms assumed by groups of particles upon vibrating elastic surfaces”, Philosophical Transactions of the Royal Society of London **121**, 299–340 (1831).

[28] J. van der Bos, A. Zijlstra, E. Gelderblom, and M. Versluis, “iLIF: illumination by laser-induced fluorescence for single flash imaging on a nanoseconds timescale”, Experiments in Fluids **51**, 1283–1289 (2011).

[29] D. Tence, S. Berger, and R. Burr, “Method and apparatus for producing dot size modulation ink jet printing”, Patent. US 5689291. November 2007.

[30] A. Chen and O. Basaran, “A new method for significantly reducing drop radius without reducing nozzle radius in drop-on-demand drop production”, Physics of Fluids **14**, L1–L4 (2002).

[31] I. Peters, Y. Tagawa, N. Oudalov, C. Sun, A. Prosperetti, D. Lohse, and D. van der Meer, “Highly focused supersonic microjets: numerical simulations”, Journal of Fluid Mechanics **719**, 587605 (2013).

[32] J. Dijksman, “Hydrodynamics of small tubular pumps”, Journal of Fluid Mechanics **139**, 173–191 (1984).

[33] J. Dijksman, “Hydro-acoustics of piezoelectrically driven ink-jet print heads”, Flow, Turbulence and Combustion **61**, 211–237 (1998).

[34] J. Segur and H. Oberstar, “Viscosity of glycerol and its aqueous solutions”, Industrial and Engineering Chemistry **43**, 2117–2120 (1951).

[35] G. P. Association, *Physical properties of glycerine and its solutions* (1963).

[36] H. N. Oĝuz and A. Prosperetti, “Dynamics of bubble growth and detachment from a needle”, Journal of Fluid Mechanics **257**, 111145 (1993).

[37] H. Power and L. Wrobel, *Boundary Integral Methods in Fluid Mechanics* (Computational Mechanics Publications) (1995).

[38] R. Bergmann, D. van der Meer, S. Gekle, A. van der Bos, and D. Lohse, “Controlled impact of a disk on a water surface: Cavity dynamics”, Journal of Fluid Mechanics **633**, 381–409 (2009).

[39] S. Gekle, J. M. Gordillo, D. van der Meer, and D. Lohse, “High-speed jet formation after solid object impact”, Physical Review Letters **102**, 034502 (2009).

[40] M. Minnaert, “XVI. On musical air-bubbles and the sounds of running water”, The London, Edinburgh, and Dublin Philosophical Magazine and Journal of Science **16**, 235–248 (1933).

[41] T. Leighton, *The Acoustic Bubble* (Academic Press) (1994).

[42] APC International, Ltd, *Piezoelectric Ceramics: Principles and Applications* (APC International) (2011).

[43] APC International, Ltd., “APC Piezo Calculator”, https://www.americanpiezo.com/knowledge-center/apc-piezo-calc.html.

[44] A. Antkowiak, N. Bremond, S. L. Dizès, and E. Villermaux, “Short-term dynamics of a density interface following an impact”, Journal of Fluid Mechanics **577**, 241–250 (2007).

3

Shortwave infrared imaging setup to study entrained air bubble dynamics in a MEMS-based piezo-acoustic inkjet printhead *

Piezo-acoustic inkjet printing is the method of choice for high-frequency and high-precision drop-on-demand inkjet printing. However, the method has its limitations due to bubble entrainment into the nozzle, leading to jetting instabilities. In this work, entrained air bubbles were visualized in a micrometer scale ink channel inside a silicon chip of a MEMS-based piezo-acoustic inkjet printhead. As silicon is semi-transparent for optical imaging with shortwave infrared (SWIR) light, a highly sensitive SWIR imaging setup was developed which exploited the optical window of silicon at 1550 nm. Infrared recordings of entrained bubbles are presented, showing rich phenomena of acoustically driven bubble dynamics inside the printhead.

3.1 Introduction

Piezo-acoustic inkjet printing is a versatile drop deposition technique and a key technology in modern industrial digital printing. With this technique, a piezo-acoustic printhead can jet single droplets on demand out of the nozzles, by driving the ink out of the nozzle thanks to the deformation of a piezoelectric element and the resulting

---

[*] Submitted as: Arjan Fraters, Tim Segers, Marc van den Berg, Hans Reinten, Herman Wijshoff, Detlef Lohse, and Michel Versluis, ”Shortwave infrared imaging setup to study entrained air bubble dynamics in a MEMS-based piezo-acoustic inkjet printhead”.

pressure field. The technique provides accurate contactless deposition of ink droplets onto a wide variety of substrates, and it can handle inks within a large range of viscosities, surface tensions, and (chemical) compositions. Typically, droplets can be produced with a volume of 1 - 32 pL, the jetting frequency ranges between 10 - 100 kHz, and the final droplet velocity ranges from 5 m/s to 10 m/s [1, 2]. These capabilities make it an attractive technique both for classical applications such as document printing, packaging, and graphic arts, as well as for novel applications such as 3D printing [3], electronic components [4–12], and (artificial) biological material [13–16].

Competition with offset printing in the large volume printing market and the rapid developments in the previously mentioned novel printing applications lead to a constant pursuit for higher productivity, higher printing quality, higher reliability and robustness, and lower costs. Therefore droplet size and production tolerances and costs must decrease, while at the same time jetting frequency, droplet velocity, and resolution (nozzles per inch) must increase. These demands led to a shift towards the use of the Micro-Electro-Mechanical Systems (MEMS) technology [17–19] that is most well known for its widespread use in the silicon-based semiconductor industry for the miniaturization of computer chips and sensors. MEMS technology is replacing classic printheads with ink channels made in for example graphite, using bulk piezos and a metal nozzle plates [1], by printheads with ink channels etched in silicon, having thin film piezos [19]. The main advantages of MEMS technology in silicon are a lower fabrication cost, a higher fabrication precision, a higher nozzle density, and shorter ink channels, allowing more efficient and controlled high DOD frequency jetting.

Figure 3.1 shows a schematic drawing of an ink channel in a MEMS printhead developed at Océ Technologies. MEMS printheads have shorter ink channels than classic printheads, i.e. of the order of 1 mm instead of 10 mm, and therefore the acoustic operating principle is also different, i.e. Helmholtz resonance [20] instead of the traveling wave principle [1].

An essential part of reliable printhead operation is the minimization of air bubble entrainment, which can occur at the nozzle, typically at a timescale of the order of 1 μs, and with an initial bubble radius of the order of 1 μm. As described in [19, 21–26], entrained air bubbles grow in the acoustic field inside the ink channel due to rectified diffusion [27–31], move to a wall due to acoustic radiation forces, and distort or even halt drop formation because their compressibility affects the acoustic pressure at the nozzle. Thus air entrainment has a detrimental effect on the printing quality and reliability. Therefore the ultimate goal is to fully understand the bubble entrainment mechanisms and subsequent bubble dynamics, so that printheads can be designed with a minimal chance of entrainment or at least a minimal influence of entrained bubbles on the droplet formation.

In classic printheads both dust particles and an ink layer on the nozzle plate

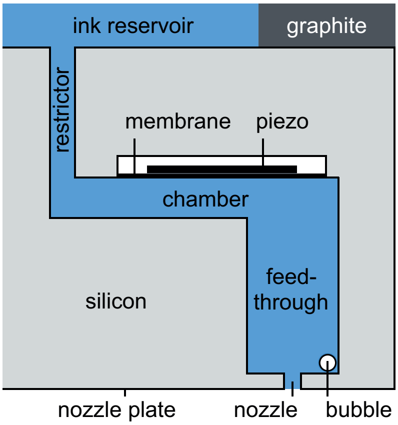

Figure 3.1: Layout of MEMS-based printhead ink channel with an entrained air bubble. The nozzle has a length and diameter of 30 µm.

have shown to induce air bubble entrainment [21]. Air entrainment through these mechanisms can be prevented by applying an anti-wetting coating to the nozzle plate, as this prevents transport of ink and dirt to jetting nozzles. Entrained bubbles were visualised in the classic printhead by replacement of the metal nozzle plate by a glass chip with ink channel-extensions terminated by nozzles. A major drawback of this method was its invasiveness, especially because of the hourglass shape of the ink channels and conical shape of the nozzles due to limitations of the powder-blasting method that was utilized to form the channels and nozzles in glass. The optically accessible glass channels were imaged using a high-speed camera at a framerate of 40 kfps and at a spatial resolution of 4 µm/pixel [22]. The bubble growth and translation could be studied from shortly after entrainment to its fully developed state. However, the imaging system was not capable of recording the entrainment process itself due to the short timescales of this process.

MEMS printheads can also suffer from bubbles that disrupt the drop formation process [18, 19]. As silicon is semi-transparent (50% - 60%) to infrared light with wavelengths between 1.1 µm and 6.0 µm, it is possible to look into a MEMS printhead using infrared imaging. In our prior work [19], this was done at a shortwave infrared (SWIR) wavelength of 1.2 µm. Entrained bubbles were observed in the feedthrough of a MEMS printhead that experienced jetting failure. The steady-state oscillations and the dissolution of fully grown bubbles were studied, and it was shown that the size of a single entrained bubble could be calculated based on only a measurement of the channel acoustics, measured through the piezo electronics. However, the entrainment process itself, and the subsequent bubble growth and translation from just after entrainment to a fully grown bubble, could not be imaged because of the limited (infrared) optical accessibility of the feedthrough through the nozzle plate, the lack of a side view into the nozzle and feedthrough, and the limited image quality, including resolution, sensitivity, and frame rate of the imaging system. So despite these previous efforts, a full understanding of the physical mechanisms involved in the bubble entrainment process and bubble dynamics is still lacking.

To overcome this shortcoming, in this work more details of the entrained air bubble dynamics in a MEMS printhead have been revealed using a newly developed, highly sensitive SWIR imaging setup, and a more recent MEMS printhead design of which the feedthroughs and nozzles are more accessible to SWIR imaging. With the new setup single bubbles were imaged in much more detail, as well as multiple bubbles and their mutual interactions. The observed phenomena include bubble growth and translation, merging of bubbles, steady-state dynamics of fully grown bubbles, long-term bubble stability, and acoustic streaming.

3.2 Experimental system

3.2.1 Printhead and ink

For this study an experimental MEMS printhead from Océ Technologies was selected and externally modified without making intrusive modifications to the functional acoustic part of the printhead. The most important requirement for this MEMS printhead was a good optical accessibility to SWIR imaging of the feedthroughs and nozzles (see Fig. 3.1) through both the bottom and side of the MEMS chip. Because of the large difference in refractive index n between the silicon ($n = 3.5$), the ink ($n = 1.5$) and the air ($n = 1.0$), the critical angles of total internal reflection for the silicon-air and the silicon-ink interfaces are only 16.6° and 25.4°, respectively [19]. Therefore the internal and external walls should ideally be smooth and oriented either perpendicular or parallel to the optical path. Deviations from the ideal orientation deteriorate the image quality and quickly result in total reflection. Therefore a MEMS chip design was chosen with all features either parallel or perpendicular to the nozzle plate, i.e. one that has no funnel between the feedthrough and the nozzle, as we had in ref. [19]. Furthermore, the feedthrough in the selected chip design has a rectangularly shaped cross-section with rounded corners instead of a circular one, as in ref. [19]. The optical path for the side view into the chip was created through a few special modifications. First, a layer of silicon was polished away from the side of the selected MEMS chip to minimize the optical path length in the silicon. Secondly, the modified chip was glued onto the printhead such that the bottom half of the polished side of the chip remained optically accessible. Lastly, an anti-wetting coating, consisting of self-assembled monolayers of (Tridecafluoro-1,1,2,2-tetrahydrooctyl)trichlorosilane (FOTS, abcr GmbH, CAS 78560-45-9), was applied to the polished side of the chip to prevent the formation of an ink layer that may distort the imaging process. The front of the nozzle plate, where the nozzle exits are located, did not suffer from the formation of an optically distorting ink layer, and therefore did not require an anti-wetting coating to achieve optical access. The nozzles were cylindrical and had a length and diameter of 30 µm. As model ink a non-colored version of the CrystalPoint$^{\mathrm{TM}}$ technology [32] was used, which is a hot melt ink that is jetted at 130°C. At this temperature the ink's viscosity, density, and surface tension are 10 mPa·s, 1080 kg/m^3, and 28 mN·m, respectively.

The printhead was actuated at a drop-on-demand (DOD) frequency of 20 kHz using a trapezoidal pulse with a rise- and fall time of 1.5 µs, and with a high time of 2 µs, optimized for an ink channel Helmholtz resonance frequency of 143 kHz. This piezo driving pulse was produced by an arbitrary waveform generator (Wavetek 195) and amplified by a broadband power amplifier (Krohn-Hite 7602M) to an actuation amplitude of 40 V, corresponding to a droplet velocity of 7 m/s. The ink channel acoustics could be monitored through a custom-made electronic device that measures the piezo current due to the piezo deformation by pressure fluctuations in the ink channel in between the actuation pulses. The piezo signals were recorded at maximum at 50 Hz, i.e. once every 400 actuation pulses, by an oscilloscope (Tektronix TDS5034B) at a sampling rate of 50 MHz. The recorded signals were stored onto a PC using a custom-made Labview program for offline processing.

3.2.2 SWIR imaging system

The shortwave infrared (SWIR) imaging system, shown in Fig. 3.2, consisted of a reflected light microscope (Olympus, BX-URA2) with SWIR compatible components, i.e. a 50:50 beamsplitter (Thorlabs, BSW29R, wavelength range: 600-1700 nm), a 50× microscope objective (Olympus, LCPLN50XIR, N.A. 0.65, working distance 4.5 mm) and a tube lens (Olympus, U-TLU IR). Illumination was provided by an infrared Light Emitting Diode (LED, Epitex, L1550-66-60-130, 1550 nm, 60 mW). A light source wavelength of 1550 nm, which is within the SWIR camera sensor range of 900 - 1700 nm and is widely used in optical communication systems, was chosen over 1200 nm as it resulted in higher quality images. The LED was used both in continuous mode by directly connecting it to a power supply unit (Delta, max. 60 V and 0.6 A), and in stroboscopic mode by connecting it to a custom-made electronic driving circuit. The stroboscopic driving circuit was designed to limit motion blur while maintaining sufficient light intensity. It delivered a large current to the LED during 500 ns pulses by discharging two capacitors (Philips, 0.68 µF, 100 V, 0.68/10/100 MKT 344 H0) via a fast switching power MOSFET with an ultra-low on-resistance (International Rectifier, HexFET Power MOSFET, IRF540Z, 29.5 mΩ, cont.: 34 A, pulsed: 140 A). Due to the short illumination time and limited brightness of the light source, every image required 1800 light flashes over a camera exposure time of 90 ms. A SWIR camera (Raptor Photonics, Ninox 640, SCD InGaAs PIN-Photodiode sensor, 640×512 pixels,

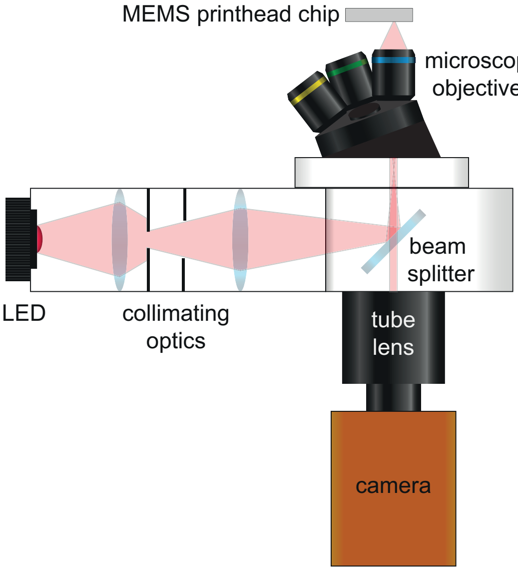

Figure 3.2: Reflected light shortwave infrared imaging setup for imaging entrained air bubbles in the ink channels of a MEMS-based printhead

15 µm pixel pitch) was attached to the microscope to record images at a resolution of 0.305 µm/pixel. The recorded images were stored onto a PC using a custom-made Labview program. Triggering of the printhead actuation, the stroboscopic illumination, and the camera recording was performed by a digital delay/pulse generator (Berkeley Nucleonics Corp, BNC 575) with nanosecond precision.

3.2.3 SWIR camera sensor selection

The camera of the SWIR imaging system was selected based on the results of a sensitivity and image quality characterization test for three different camera sensors. The three sensors were selected primarily based on their sensitivity (quantum efficiency, dynamic range, and dark current), the pixel pitch, and the number of pixels. The sensitivity is important in view of the short illumination times required to freeze the motion of an oscillating bubble of micrometer size. A small pixel pitch is desirable because it requires less magnification and resulting light loss. A large number of pixels is desirable to get high resolution images. All three sensors were Indium Gallium Arsenide (InGaAs) sensors. More information on architectural differences between the sensors was not publicly available. The basic characteristics of the tested camera sensors are summarized in Table 3.1.

The sensitivity of the sensors was tested using the setup illustrated in Fig. 3.3(a). Note that this characterization setup is different from the imaging setup presented in

Table 3.1: Demo camera sensor characteristics

	Sensor 1	**Sensor 2**	**Sensor 3**
Pixel array size (px)	1280x1024	640x512	640x512
Pixel pitch (µm)	12.5	15	20
Max. frame rate (fps)	60	90	400

Section 3.2.2. It had a transmitted light microscope (Olympus, BXFM-F + BXFM-ILHS + U-DP) with a 10× infrared microscope objective (Olympus, LMPLN10XIR, N.A. 0.3, working distance 18 mm) and an infrared tube lens (Olympus, U-TLU IR). The LED, the same as in the other setup, emitted light continuously at full power, and measurements were performed at neutral density (ND) filter fractional transmittance values between 1 (no filter) and 0.001 (Thorlabs, NENIRxxA where x = number between 0-9), and at exposure times between 50 µs and 10 ms. A test target (Thorlabs, R3L3S1N, Negative 1951 USAF Test Target, 3”×3”) was placed in the optical path to form an image with a light and dark region, separated by a sharp transition. All recordings were performed in the most sensitive mode of each sensor, usually called the high gain mode. The sensors were tested both with non-uniformity correction (NUC) off and on. The NUC corrects for bad pixels, and for differences between the pixel offset, gain, and dark current, because each pixel has its own A/D converter.

Figure 3.3(b) shows part of a typical recording by the sensitivity test setup, and illustrates how the signal and noise were determined from such an image using a script programmed in Python (Python Software Foundation, https://www.python.org/). For both the light section in between the black dashed lines and the dark section in between the white dashed lines the mean pixel value was calculated, and the difference between the two was defined as the signal. The noise was extracted from the dark pixel array section in between the white dashed lines. First the array was flattened by subtracting the baseline, a polyfit plane of order 10 fitted to this array, from it. Then the noise was obtained by calculating the standard deviation of the flattened array.

The measurement results are summarized in Figs. 3.3(c) and 3.3(d). From these results it was concluded that Sensor 3 could not compete with the other two sensors, because it had a much lower signal to noise ratio at the same light intensity. The differences between Sensor 1 and Sensor 2 were less evident. As a final test, a bottom view recording was made of an ink channel in the MEMS printhead with stroboscopic illumination using the imaging setup shown in Fig. 3.2, and using the same number of light flashes per image. Figures 3.3(e) and 3.3(f) show the nozzle and thin ink layers on the nozzle plate. The noise level of the image recorded using Sensor 2 was lower than that of the image recorded by Sensor 1. Therefore Sensor 2 was selected for the SWIR imaging setup.

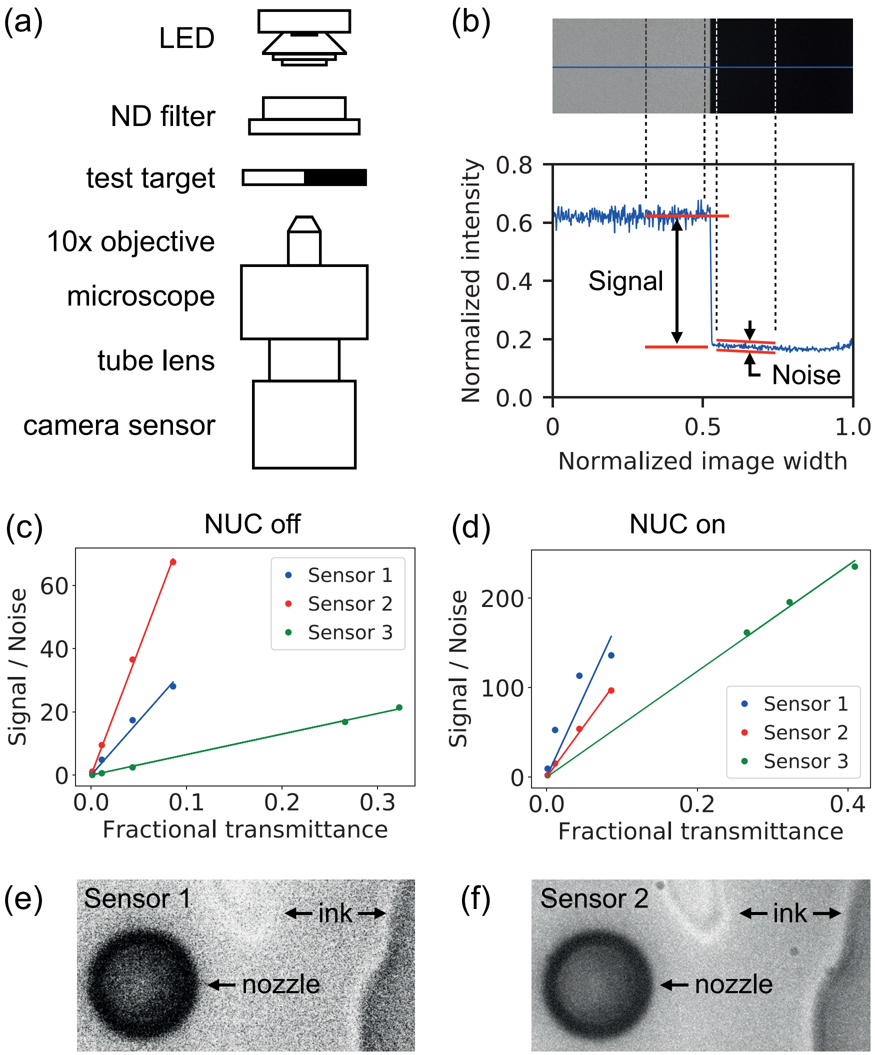

Figure 3.3: (a) Camera sensor sensitivity measurement setup. (b) Part of a sensitivity image with below it a plot of the intensity values of the pixels on the blue line. Signal and noise are extracted from the light and dark region in between the dashed lines. (c, d) signal to noise ratio at 500 μs exposure time with non-uniformity correction off and on, respectively. (e, f) Image quality at low light condition during stroboscopic imaging of an inkjet nozzle (30 μm diameter) in bottom view using the imaging setup in Fig. 3.2.

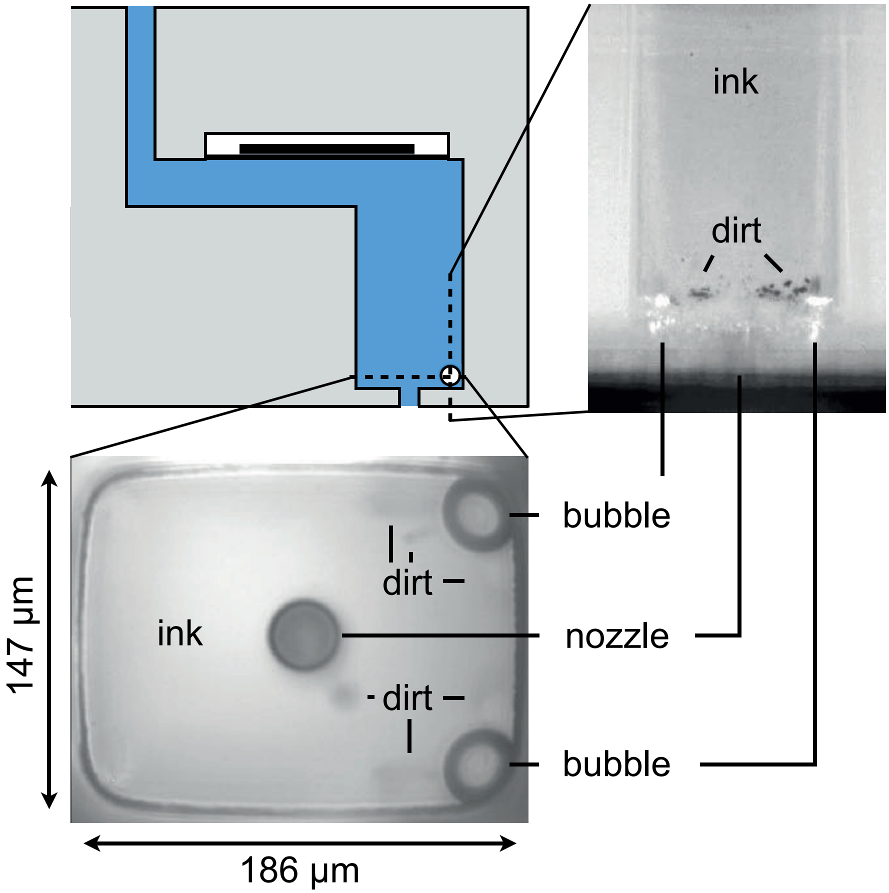

Figure 3.4: Typical bottom view and side view of an ink channel in the MEMS printhead imaged by the shortwave infrared imaging setup.

3.2.4 Image quality and optical accessibility

The SWIR imaging system's image quality and optical access to the feedthroughs and nozzles of the MEMS-based printhead are demonstrated in Fig. 3.4. In both the image of the bottom view and that of the side view two entrained air bubbles are visible, as well as dirt particles that collected around the bubbles and the nozzle. The bottom view shows an actuated channel with fast streaming around the bubbles and the nozzle due to acoustic streaming. So particles are blurred because of their motion, in contrast to the side view. In the side view, showing a non-actuated channel, the bubbles are not as clearly visible because the feedthrough side wall was not as straight and smooth as the bottom of the feedthrough. In the side view also the nozzle could not be clearly imaged and the meniscus could not be visualized, which is a result of the combination of a cylindrical nozzle shape with the small critical angles of total internal reflection of the silicon interfaces with ink and air. This underlines the imaging challenges involved.

3.2.5 Experimental settings and image processing

The growth, translation, and interaction of bubbles from just after entrainment to a fully grown state were captured by real-time imaging at a frame rate of 50 or 60 fps, using continuous SWIR illumination. The steady-state dynamics of fully grown bubbles during one drop-on-demand period of 50 µs were captured stroboscopically at a temporal resolution of 0.5 µs. In the stroboscopic recording mode an image and a piezo signal were captured once every 0.4 s, to allow the computer to store the data and change the settings of the pulse delay generator.

The contrast between the bubbles and the background in the recorded images was enhanced with the image processing program ImageJ (http://imagej.nih.gov/ij). In the experiments for which a reference image was available with an ink channel without bubbles and particles, the contrast between the feedthrough wall and the bubble was increased by first subtracting the bubble image from the reference image, and then subtracting the resulting image from the bubble image. Furthermore, the function ’subtract background’ in ImageJ was used to filter out the uneven illumination in some parts of the background. Finally, contrast was enhanced by adapting the image histogram.

3.3 Experimental observations

3.3.1 Bubble entrainment

A typical recording of bubble entrainment is shown in Fig. 3.5 and Supplementary Video 1. Initially, multiple bubbles of different sizes, here with diameters between 3 and 8 µm, were entrained and spread along the feedthrough wall at the intersection with the nozzle plate. The maximum frame rate of 90 fps was not high enough to capture the entrainment process and the origin of the observed multiple bubbles. The bubbles remained positioned at their initial location for at least 20 ms, grew by rectified diffusion [27–31], and at a certain moment moved to a corner. These movements are explained by secondary Bjerkness forces [29–31, 33] attracting bubbles to the wall and into the corner, and by wall roughness holding bubbles temporarily in place along the wall. Multiple bubbles located at a single corner interacted and either quickly merged or coexisted in a semi-stable equilibrium; some bubbles coexisted stably for up to at least several minutes.

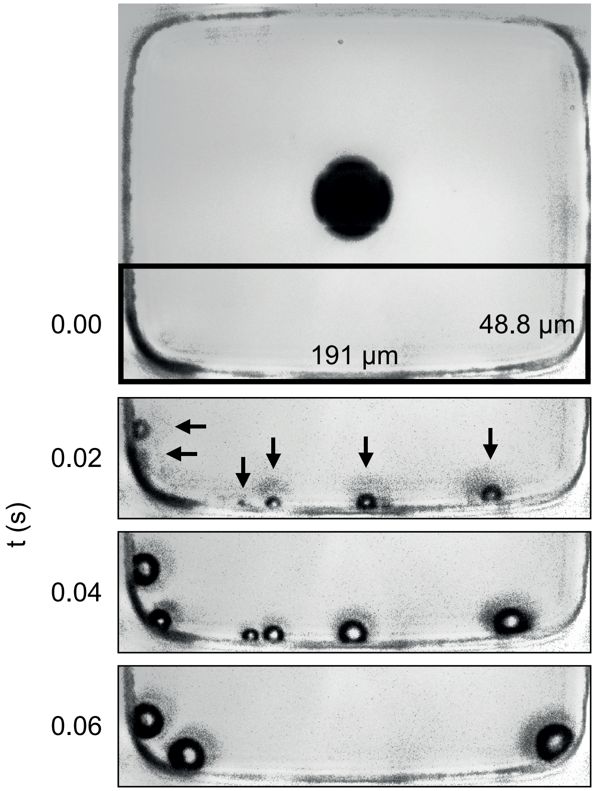

Figure 3.5: Real-time 50 fps bottom view recording of bubble entrainment, with *t* being the time after entrainment. The shadow around the bubbles is caused by motion blur due to oscillation of the bubbles at the microsecond timescale during actuation. See also Supplementary Video 1.

3.3.2 Merging of bubbles by Ostwald ripening

In the case that multiple bubbles were present in the same corner, and merged, it was not necessarily due to coalescence. In multiple occasions an Ostwald ripening [34–37] type of process was observed, i.e. exchange of gas between bubbles by diffusion of gas through the liquid. An example is shown in Fig. 3.6 and Supplementary Video 2. Initially, the two bubbles in the bottom-right corner of the channel approached each other and grew due to rectified diffusion. Between t = 0.28 s and t = 0.45 s bubble 2 shrunk, while bubble 1 grew, i.e. a large portion of the gas from bubble 2 diffused through the surrounding liquid into bubble 1. The gas exchange here was more complicated than in conventional Ostwald ripening, as not only the Laplace pressure in the bubbles played a role, but the bubbles were also prone to rectified diffusion, a process that is affected by the presence of the wall, bubble (shape) oscillations, surfactants, and acoustic streaming [38–40]. After t = 0.45 s bubble 2 moved behind bubble 1, and between t = 0.60 s and t = 0.62 s bubble 2 disappeared.

3.3.3 Steady-state dynamics of fully grown bubbles

Within a few seconds after entrainment, the bubbles reached an equilibrium state in which the number of bubbles, the bubble sizes, and the bubble positions remained constant. This allowed for the use of stroboscopic imaging to study the steady-state bubble dynamics. Figure 3.7(a) and Supplementary Video 3 show four of the observed equilibrium bubble configurations: Fig. 3.7(a)-a a single bubble, Fig. 3.7(a)-b two bubbles of different size, Fig. 3.7(a)-c two bubbles of a similar size, and Fig. 3.7(a)-d three bubbles of which two were of a similar size. The images in each column show the following five different states of the bubble dynamics: 1. at rest, 2. at the first maximum expansion, 3. first maximum compression, 4. asymmetric bubble collapse towards the wall, and 5. the second maximum expansion. The estimated total volumes of the bubbles at rest in the four cases were 22 pL, 8.9 pL, 4.9 pL, and 2.5 pL, respectively. Figures 3.7(b) and 3.7(c) show that in all four cases the presence of bubbles in the ink channel can be acoustically detected. Figure 3.7(b) presents the piezo signals of the four cases with bubbles and of one case without bubbles. Figure 3.7(c) displays the Fourier transform of these signals over the region between 7.5 and 50 µs, i.e. after the piezo actuation, as indicated by the region with the grey background in Fig. 3.7(b). Thus, the entrainment of a single bubble in a channel with initially no bubbles resulted in an increase of the peak frequency of 43%, from 142 kHz to 203 kHz, while the amplitude of the peak frequency increased by almost a factor of two.

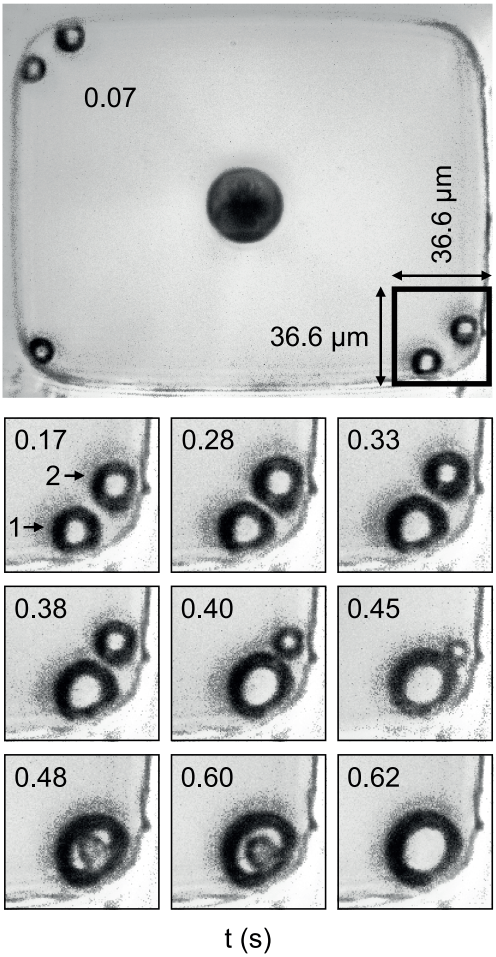

Figure 3.6: Real-time 60 fps recording of diffusive interaction between two bubbles in the same corner, with *t* being time after entrainment. The shadow around the bubbles is caused by motion blur due to the oscillations of the bubbles at the microsecond timescale during actuation. See also Supplementary Video 2.

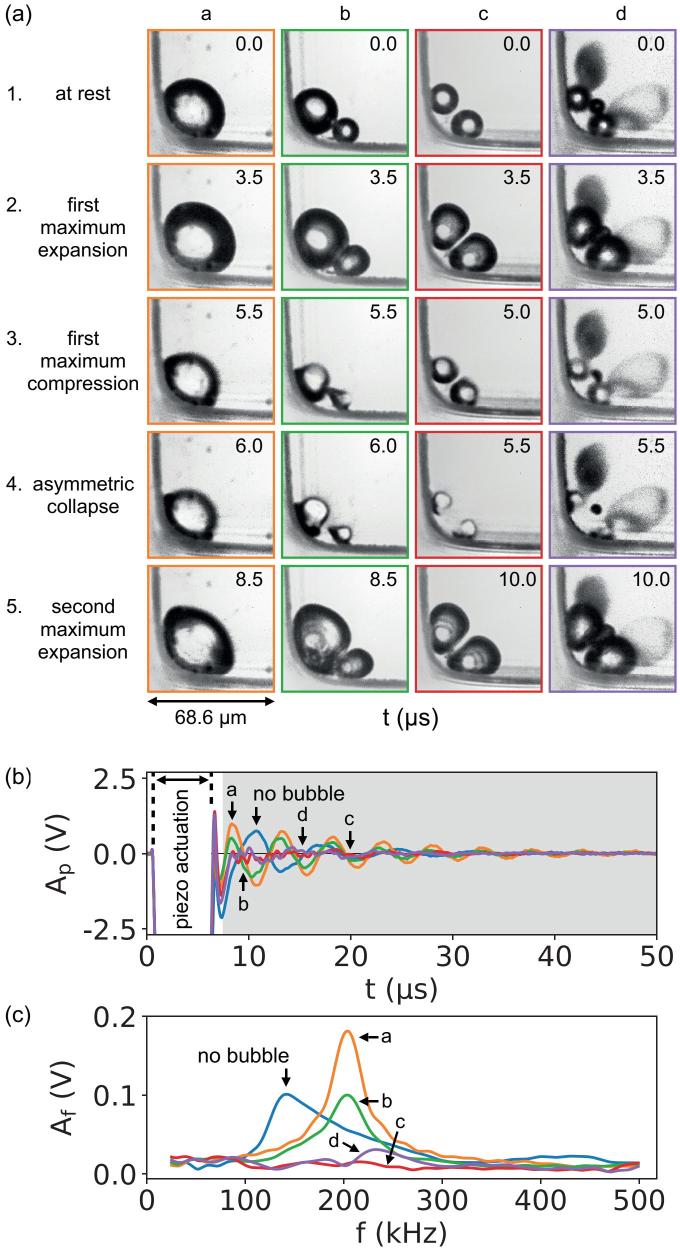

Figure 3.7: (a) Stroboscopically recorded images (68.6×68.6 μm) of four different bubble configurations, showing five different stages in their bubble dynamics. *t* is the time from the start of the actuation pulse in μs. See also Supplementary Video 3. (b) Piezo signals of the four different bubble configurations, and of a reference case with no bubbles in the channel. (c) Fourier transforms of the piezo signals

3.3.4 Stable coexistence of colliding bubbles

The image sequence in Fig. 3.8(a) and Supplementary Video 4 show details of the steady-state volume oscillations of two non-coalescing bubbles of a similar size. During every piezo actuation, the bubbles were acoustically driven into oscillation, and twice the bubbles collided, i.e. their surfaces flattened in the area of close proximity after having approached each other at a finite velocity: the first time for 2.5 µs starting at t = 2.5 µs, and the second time for 7.5 µs starting at t = 8.5 µs. During these two collisions the bubble surfaces approached each other at an approximate maximum velocity of 2 m/s and 5 m/s, which, with bubble radii of 8 µm and 10 µm, corresponds to Weber numbers of 1.2 and 9.6, respectively. In this high Weber number regime, where the bubble surfaces are flattened during collision, coalescence is delayed by the drainage of the liquid film in between the flat surfaces of the bubbles, especially because of the presence of surface-active components in the ink [41]. In between the collisions the bubbles asymmetrically collapsed in opposite direction, towards two different sides of the wall at the corner, thereby limiting the contact time between the bubbles and thus also hindering coalescence. This is visible in Fig. 3.8(a) at t = 5.0 µs to t = 6.0 µs, where the distance between the bubble surfaces increased rapidly and the bubble surfaces strongly deformed. During asymmetric collapse of a single bubble in one of the other corners, see Fig. 3.8(b), the deformation was even so large that a jet penetrated the bubble in the direction of the wall, resulting in a toroidal bubble. Asymmetric collapse and microjet formation for bubbles at a wall are well-known phenomena, and are described in detail in [29, 30, 42–48].

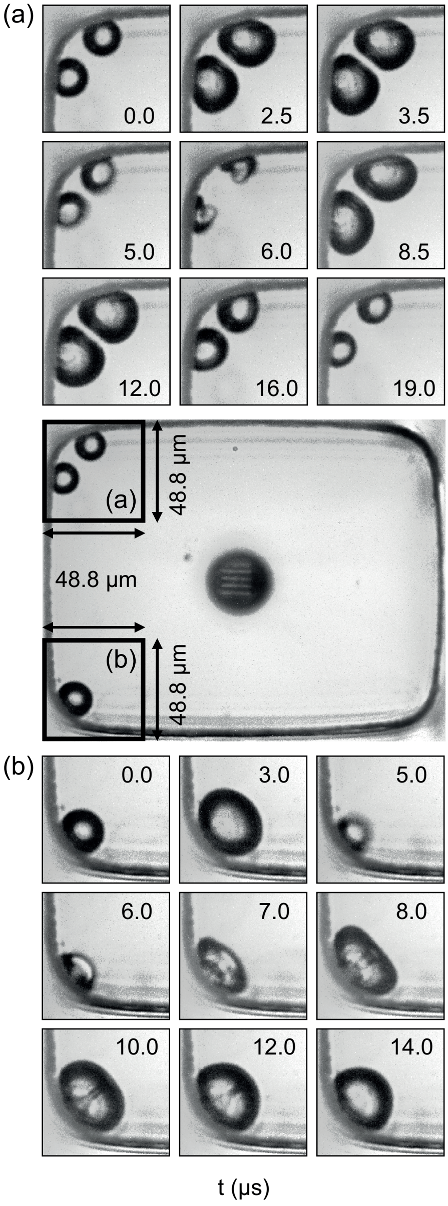

Figure 3.8: Two stroboscopically recorded image sequences, with *t* being the time from the start of the actuation pulse. (a) Two bubbles of a similar size colliding twice during one drop-on-demand period of 50 µs without coalescing. (b) Asymmetric collapse of a single bubble towards the wall, whereby a jet is formed in the bubble directed at the wall, and the bubble gets a toroidal shape. See also Supplementary Video 4.

3.3.5 Acoustic streaming

The flow induced by acoustic streaming [49, 50], driven by a phase difference between the volumetric and translational oscillations of the bubble [51–53], was visible in the experiments due to dirt particles that collected in the streamlines around the bubbles and above the nozzle. This was already briefly discussed in Fig. 3.4, and is shown in more detail in Fig. 3.9 and Supplementary Video 5. Here, bubbles were entrained into the channel after 7.5 s of printhead operation, and collected in two corners of which one is shown in the image sequence in Fig. 3.9(a). After having reached an equilibrium state at t = 8.77 s, dirt particles collected around the bubbles in streaming patterns as shown at t = 40.65 s. The motion blur in the images of the dirt particles is indicative of the high streaming velocity in this experiment. When the actuation was halted, the bubbles dissolved, and in the absence of acoustic streaming the dirt particles were trapped in the viscous surrounding, visible at t = 40.67 s and t = 41.92 s.

For the nozzle it was observed that during the jetting phase, when no bubbles were entrained, dirt particles were always present near the edge of the nozzle. For example, in Fig. 3.9 at t = 7.5 s a dirt particle is visible in the top right corner of the nozzle. These particles seemed to circle near the nozzle, while their trajectories slightly fluctuated in position around the circumference of the nozzle edge. After bubble entrainment it was observed that the dirt particle trajectories both had periods were they would constantly move around the circumference of the nozzle edge, and periods where they were more fixed at one location above the nozzle edge. Figure 3.9(b) shows a time interval were they were more fixed: the three particles visible at t = 31.67 s are still at the identical location at t = 40.67 s, which is 9.00 s later, or after approximately 180,000 actuations.

3.4 Discussion and Outlook

The SWIR imaging setup has revealed remarkably rich and complex phenomena of acoustically driven bubble dynamics inside a MEMS-based printhead, in particular the entrainment and interaction of multiple bubbles. However, it was not able to capture the bubble entrainment mechanism because of the limited camera framerate and the optical inaccessibility of the nozzle area.

The SWIR imaging setup could be further used to study the effect of the number of bubbles, and the bubble size and position on the channel acoustics. This allows improvement of the existing acoustic model for calculating the bubble size based on just the measured piezo signal [19, 23, 24, 26], which is currently based on the presence of only a single bubble in the channel. It is of interest to further investigate the interaction of two bubbles in the regime where the simultaneous occurrence of Ostwald ripening and rectified diffusion plays an important role. These topics will be part of a future more detailed study.

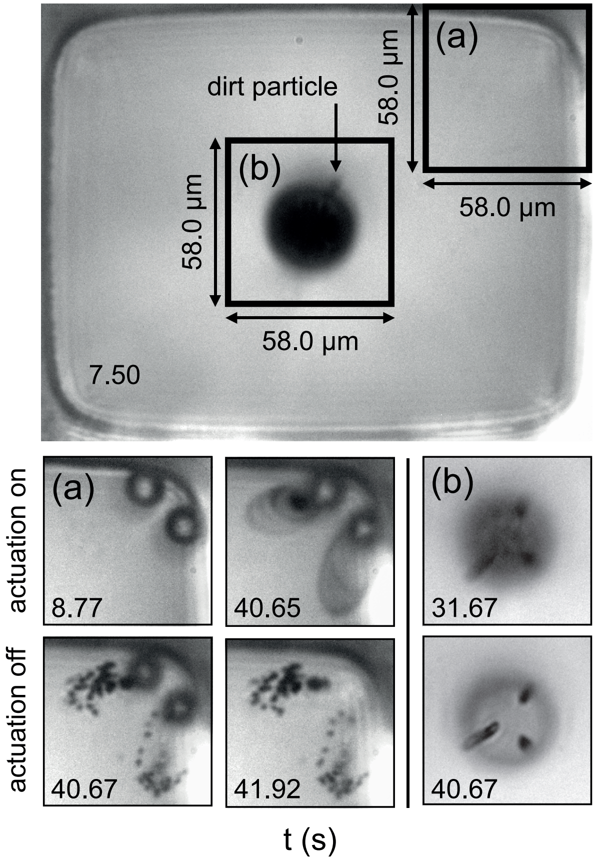

Figure 3.9: Real-time 60 fps recording of dirt particles captured in acoustic streaming streamlines, with t being the time after the start of actuation. After t = 40.65 s the piezo actuation is turned off. (a) Two coexisting bubbles in the same corner that dissolve once piezo actuation has stopped. (b) Dirt particles that are captured in fixed trajectories above the nozzle. See also Supplementary Video 5.

3.5 Conclusion

Entrained air bubbles and ink flow in a MEMS-based piezo-acoustic drop-on-demand printhead can be visualized using shortwave infrared (SWIR) imaging because the silicon walls of the ink channels are semi-transparent to infrared light. A highly sensitive SWIR imaging system and a SWIR accessible MEMS-based printhead were developed to study entrained air bubbles in the ink channel. The growth, translation, and interactions of bubbles shortly after entrainment were imaged in real-time at a framerate of 50 fps. The steady-state dynamics of fully grown bubbles were imaged stroboscopically at a temporal resolution of 0.5 µs. In both cases the piezo signal, representing the pressure fluctuations in the ink channel after actuation, was recorded each time an image was captured.

The recordings showed that, shortly after bubble entrainment, initially multiple bubbles of different size were spread along the feedthrough wall at the nozzle plate, and that eventually the bubbles collected at the corners of the feedthrough. The interactions of multiple bubbles in the same corner in some cases led to merging of the bubbles through Ostwald ripening, and in other cases to semi-stably coexisting bubbles. Bubbles coexisting in the same corner did not merge through coalescence because they collided at high Weber number during the expansion phase and collapsed asymmetrically towards the wall during the compression phase. Acoustic streaming near the nozzle and around entrained bubbles was visible due to the presence of dirt particles that were captured in the streamlines above the nozzle and around the bubbles. These observations demonstrate that with a highly sensitive SWIR imaging system the phenomena of fluid flow and acoustics in silicon devices, such as a MEMS-based piezo-acoustic inkjet printhead, can be studied in detail down the micrometer lengthscale and at the microsecond timescale.

References

[1] H. Wijshoff, “The dynamics of the piezo inkjet printhead operation”, Physics Reports **491**, 77–177 (2010).

[2] S. D. Hoath, *Fundamentals of Inkjet Printing: The Science of Inkjet and Droplets* (Wiley-VCH Verlag GmbH & Co. KGaA) (2015).

[3] B. Derby, “Additive manufacture of ceramic components by inkjet printing”, Engineering **1**, 113–123 (2015).

[4] S. Majee, M. Song, S.-L. Zhang, and Z.-B. Zhang, “Scalable inkjet printing of shear-exfoliated graphene transparent conductive films”, Carbon **102**, 51–57 (2016).

[5] S. Majee, C. Liu, B. Wu, S.-L. Zhang, and Z.-B. Zhang, “Ink-jet printed highly conductive pristine graphene patterns achieved with water-based ink and aqueous doping processing”, Carbon **114**, 77–83 (2017).

[6] S. Eshkalak, A. Cinnappan, W. Jayathilaka, M. Khatibzadeh, E. Kowsari, and S. Ramakrishna, “A review on inkjet printing of CNT composites for smart applications”, Applied Materials Today **9**, 372–386 (2017).

[7] M. Vilardell, X. Granados, S. Ricart, I. V. Driessche, A. Palau, T. Puig, and X. Obradors, “Flexible manufacturing of functional ceramic coatings by inkjet printing”, Thin Solid Films **548**, 489–497 (2013).

[8] A. Moya, G. Gabriel, R. Villa, and F. J. del Campo, “Inkjet-printed electrochemical sensors”, Current Opinion in Electrochemistry **3**, 29–39 (2017).

[9] T. Eggenhuisen, Y. Galagan, E. Coenen, W. Voorthuijzen, M. Slaats, S. Kommeren, S. Shanmuganam, M. Coenen, R. Andriessen, and W. Groen, “Digital fabrication of organic solar cells by inkjet printing using non-halogenated solvents”, Solar Energy Materials and Solar Cells **134**, 364–372 (2015).

[10] S. Hashmi, M. Ozkan, J. Halme, K. Misic, S. Zakeeruddin, J. Paltakari, M. Grätzel, and P. Lund, “High performance dye-sensitized solar cells with inkjet printed ionic liquid electrolyte”, Nano Energy **17**, 206–215 (2015).

[11] T. Shimoda, K. Morii, S. Seki, and H. Kiguchi, “Inkjet printing of light-emitting polymer displays”, Inkjet Printing of Functional Materials **28**, 821–827 (2003).

[12] C. Jiang, L. Mu, J. Zou, Z. He, Z. Zhong, L. Wang, M. Xu, J. Wang, J. Peng, and Y. Cao, “Full-color quantum dots active matrix display fabricated by ink-jet printing”, Science China Chemistry **60**, 1349–1355 (2017).

[13] A. Simaite, F. Mesnilgrente, B. Tondu, P. Souères, and C. Bergaud, “Towards inkjet printable conducting polymer artifical muscles”, Sensors and Actuators B: Chemical **229**, 425–433 (2016).

[14] S. Hewes, A. Wong, and P. Searson, “Bioprinting microvessels using and inkjet printer”, Bioprinting **7**, 14–18 (2017).

[15] M. Nakamura, A. Kobayashi, F. Takagi, A. Watanabe, Y. Hiruma, K. Ohuchi, Y. Iwasaki, M. Horie, I. Morita, and S. Takatani, “Biocompatible inkjet printing technique for designed seeding of individual living cells”, Tissue Engineering **11**, 1658–1666 (2005).

[16] G. Villar, A. Graham, and H. Bayley, “A tissue-like printed material”, Science **340**, 48–52 (2013).

[17] C. Menzel, A. Bibl, and P. Hoisington, “MEMS solutions for precision microfluidic dispensing application”, Technical Report, Fujifilm Dimatix Inc. (2004).

[18] B.-H. Kim, T.-G. Kim, T.-K. Lee, S. Kim, S.-J. Shin, S.-J. Kim, and S.-J. Lee, “Effects of trapped air bubbles on frequency responses of the piezo-driven inkjet printheads and visualization of the bubbles using synchrotron X-ray”, Sensors and Actuators A: Physical **154**, 132–139 (2009).

[19] A. van der Bos, T. Segers, R. Jeurissen, M. van den Berg, H. Reinten, H. Wijshoff, M. Versluis, and D. Lohse, “Infrared imaging and acoustic sizing of a bubble inside a micro-electro-mechanical system piezo ink channel”, Journal of Applied Physics **110**, 034503 (2011).

[20] H. von Helmholtz, *On the sensations of tone as a physiological basis for the theory of music* (London, New York: Longmans, Green, and Co.) (1895).

[21] J. de Jong, G. de Bruin, H. Reinten, M. van den Berg, H. Wijshoff, M. Versluis, and D. Lohse, “Air entrapment in piezo-driven inkjet printheads”, Journal of the Acoustical Society of America **120**, 1257–1265 (2006).

[22] J. de Jong, R. Jeurissen, H. Borel, M. van den Berg, H. Wijshoff, H. Reinten, M. Versluis, A. Prosperetti, and D. Lohse, “Entrapped air bubbles in piezo-driven inkjet printing: their effect on the droplet velocity”, Physics of Fluids **18**, 121511 (2006).

[23] R. Jeurissen, J. de Jong, H. Reinten, M. van den Berg, H. Wijshoff, M. Versluis, and D. Lohse, “Effect of an entrained air bubble on the acoustics of an ink channel”, Journal of the Acoustical Society of America **123**, 2496–2505 (2008).

[24] R. Jeurissen, A. van der Bos, H. Reinten, M. van den Berg, H. Wijshoff, J. de Jong, M. Versluis, and D. Lohse, “Acoustic measurement of bubble size in an inkjet printhead”, Journal of the Acoustical Society of America **126**, 2184–2190 (2009).

[25] S. Lee, D. Kwon, and Y. Choi, “Dynamics of entrained air bubbles inside a piezodriven inkjet printhead”, Applied Physics Letters **95**, 221902 (2009).

[26] R. Jeurissen, H. Wijshoff, M. van den Berg, H. Reinten, and D. Lohse, “Regimes of bubble volume oscillations in a pipe”, Journal of the Acoustical Society of America **130**, 3220–3232 (2011).

[27] A. Eller and H. Flynn, “Rectified diffusion during nonlinear pulsations of cavitation bubbles”, Journal of the Acoustical Society of America **37**, 493–503 (1965).

[28] L. Crum, “Rectified diffusion”, Ultrasonics **22**, 215–223 (1984).

[29] T. Leighton, *The Acoustic Bubble* (Academic Press) (1994).

[30] C. Brennen, *Cavitation and Bubble Dynamics* (Oxford University Press, New York) (1995).

[31] M. Brenner, S. Hilgenfeldt, and D. Lohse, “Single-bubble sonoluminescence”, Reviews of Modern Physics **74**, 425–484 (2002).

[32] Océ Technologies B.V., For more information on Océ CrystalPoint technology see `https://www.oce.com/products/crystalpoint/`.

[33] V. Garbin, B. Dollet, M. Overvelde, D. Cojoc, E. D. Fabrizio, L. van Wijngaarden, A. Prosperetti, N. de Jong, D. Lohse, and M. Versluis, “History force on coated microbubbles propelled by ultrasound”, Physics of Fluids **21**, 092003 (2009).

[34] W. Ostwald, “Studien über die bildung und umwandlung fester körper”, Zeitschrift für Physikalische Chemie **22**, 289–330 (1897).

[35] R. Lemlich, “Prediction of changes in bubble size distribution due to interbubble gas diffusion in foam”, Industrial and Engineering Chemistry Fundamentals **17**, 89–93 (1978).

[36] S. Tcholakova, Z. Mitrinova, K. Golemanov, N. Denkov, M. Vethamuthu, and K. Ananthapadmanabhan, “Control of Ostwald ripening by using surfactants with high surface modulus”, Langmuir **27**, 14807–14819 (2011).

[37] M. Lee, E. Lee, D. Lee, and B. Park, “Stabilization and fabrication of microbubbles: applications for medical purposes and functional materials”, Soft Matter **11**, 2067–2079 (2015).

[38] R. Gould, “Rectified diffusion in the presence of, and absence of, acoustic streaming”, Journal of the Acoustical Society of America **56**, 1740–1746 (1974).

[39] L. Crum, “Measurements of the growth of air bubbles by rectified diffusion”, Journal of the Acoustical Society of America **68**, 203–211 (1980).

[40] T. Leong, J. Collis, R. Manasseh, A. Ooi, A. Novell, A. Bouakaz, M. Ahokkumar, and S. Kentish, “The role of surfactant headgroup, chain length, and cavitation microstreaming on the growth of bubbles by rectified diffusion”, Journal of Physical Chemistry C **115**, 24310–24316 (2011).

[41] M. Postema, P. Marmottant, C. Lancée, S. Hilgenfeldt, and N. de Jong, “Ultrasound-induced microbubble coalescence”, Ultrasound in Medicine and Biology **30**, 1337–1344 (2004).

[42] T. Benjamin and A. Ellis, “The collapse of cavitation bubbles and the pressures thereby produced against solid boundaries”, Philosophical Transactions of the Royal Society of London A: Mathematical and Physical Sciences **260**, 221–240 (1966).

[43] M. Plesset and R. Chapman, “Collapse of an initially spherical vapour cavity in the neighbourhood of a solid boundary”, Journal of Fluid Mechanics **47**, 283–290 (1971).

[44] L. Crum, “Surface oscillations and jet development in pulsating bubbles”, Journal de Physique Colloques **40**, 285–288 (1979).

[45] W. Lauterborn, “Cavitation bubble dynamics - new tools for an intricate problem”, Applied Scientific Research **38**, 165–178 (1982).

[46] J. Blake, M. Hooton, P. Robinson, and R. Tong, “Collapsing cavities, toroidal bubbles and jet impact”, Philosophical Transactions of the Royal Society A: Mathematical, Physical and Engineering Sciences **355**, 537–550 (1997).

[47] M. Postema, A. van Wamel, F. ten Cate, and N. de Jong, “High-speed photography during ultrasound illustrates potential therapeutic applications of microbubbles”, Medical Physics **32**, 3707–3711 (2005).

[48] H. Vos, B. Dollet, M. Versluis, and N. de Jong, “Nonspherical shape oscillations of coated microbubbles in contact with a wall”, Ultrasound in Medicine and Biology **37**, 935–948 (2011).

[49] J. Lighthill, “Acoustic streaming”, Journal of Sound and Vibration **61**, 391–418 (1978).

[50] M. Longuet-Higgins, “Viscous streaming from an oscillating spherical bubble”, Proceedings of the Royal Society A: Mathematical, Physical and Engineering Sciences **454**, 725–742 (1998).

[51] P. Marmottant and S. Hilgenfeldt, “Controlled vesicle deformation and lysis by single oscillating bubbles”, Nature **423**, 153–156 (2003).

[52] P. Marmottant, M. Versluis, N. de Jong, S. Hilgenfeldt, and D. Lohse, “High-speed imaging of an ultrasound-driven bubble in contact with a wall: ”Narcissus” effect and resolved acoustic streaming”, Experiments in Fluids **41**, 147–153 (2006).

[53] G. Lajoinie, Y. Luan, E. Gelderblom, B. Dollet, F. Mastik, H. Dewitte, I. Lentacker, N. de Jong, and M. Versluis, “Non-spherical oscillations drive the ultrasound-mediated release from targeted microbubbles”, Communications Physics **1** (2018).

4

Dirt particles trigger nozzle failure: bubble nucleation, dynamics, and diffusive growth visualized in a piezo-acoustic printhead [*]

Piezo-acoustic drop-on-demand (DOD) inkjet printing is omnipresent in high-end digital printing due to unprecedented precision and reproducibility at which micron-sized droplets of a wide range of chemical compositions can be deposited. However, the stability of piezo DOD inkjet printing can in rare occasions be compromised through the stochastic entrainment of bubbles inside the ink channel. Here, bubble entrainment, translation, and growth in an experimental silicon-based printhead with glass nozzle plate were studied using high-speed imaging triggered by changes in the ink channel acoustics. The experimental printhead was produced using unconventional production methods, resulting in dirt particle polluted ink channels with a higher bubble entrainment probability than regular printheads. It was found that dirt particles trigger bubble nucleation upon their interaction with the oscillating meniscus. The entrained bubble was used as a sensitive pressure sensor with which channel pressure profiles could be measured, namely from fitting the measured radial bubble dynamics to the Rayleigh-Plesset equation. The ink jet length increase of 24% after bubble entrainment was shown to be a result of the bubble-induced decrease of the channel resonance frequency. We also traced the acoustically driven bubble inside the ink channel. It

---

[*] To be submitted as: Arjan Fraters, Tim Segers, Marc van den Berg, Youri de Loore, Hans Reinten, Herman Wijshoff, Detlef Lohse, and Michel Versluis, ”Dirt particles trigger nozzle failure: bubble nucleation, dynamics, and diffusive growth visualized in a piezo-acoustic printhead”.

translates towards the channel wall due to a combination of acoustic radiation forces and convective ink flow. Next, the ink velocity field was characterized using particle tracking velocimetry. The vortical flow next to the oscillating meniscus was shown to trap dirt particles, thereby increasing the particle-to-meniscus interaction probability. Both cavitation on a particle during the rarefaction pressure wave and direct contact of a particle with the meniscus during fast advancement and retraction of the meniscus were identified as possible mechanisms through which bubbles might nucleate.

4.1 Introduction

Inkjet printing is a successful industrial application of microfluidics [1–3]. It allows for highly controlled non-contact material deposition at picoliter volumes. The high versatility of piezo-driven drop-on-demand (DOD) inkjet printing results from the wide range of ink properties that can be jetted. Consequently, it is widely used in an industrial setting for document printing, for printing graphic arts, and for package printing [1]. More recently, inkjet technology was successfully employed for additive manufacturing of, e.g. electronic components [4–12], pharmaceuticals [13], biomaterials [14–17], and ceramic components [18].

Earlier piezo-driven printheads were fabricated through micro-machining. These ink channels had a typical length on the order of centimeters [1]. The pressure buildup at the nozzle entrance required to jet a droplet was generated through positive interference of traveling acoustic waves [1, 19]. More recently, the inkjet industry developed printheads using Micro-Electro-Mechanical-System (MEMS) technology [20–23]. MEMS technology allows for lower fabrication costs with respect to micromachining techniques, a higher fabrication precision, a higher nozzle density, and shorter ink channels, allowing for more efficient and well-controlled jetting at high DOD frequencies. MEMS-based ink channels have dimensions much smaller than the wavelength of the acoustic driving pulse. The resulting channel acoustics is that of a Helmholtz resonator [24], i.e. it is comparable to a classical mass-spring system. The resonance frequency is governed by the mass of ink in the nozzle and restrictor, and by the compressibility of the ink chamber, i.e. that of the total ink volume and that of the wall including the membrane with the thin film piezo actuator [1, 2].

The stability and reproducibility of droplet formation is crucial for reliable inkjet printing applications. Typically, billions of droplets can be jetted at a very high reproducibility. However, it has been shown that the jet reproducibility is sometimes compromised through the entrainment of air bubbles in the ink channel [21, 22, 25–30]. An entrained bubble disturbs the ink-channel acoustics and thereby droplet formation. At a later stage, when the bubble has grown through rectified diffusion [31–34], its compressibility can even counteract the pressure buildup to such an extent that the droplet formation stops. Once a bubble is entrained, it can be eliminated through diffusive dissolution, e.g. by switching off the piezo actuation for a period of the order of seconds to minutes [22, 26].

To increase the stability of the inkjet printing process, it is crucial to understand the physical mechanisms by which bubbles are entrained into the ink channel. Potential entrainment mechanisms include bubble cavitation [33] in the rarefaction pressure wave, bubble inclusion by direct contact of dirt particles in the ink channel with the meniscus, and bubble pinch-off from a meniscus instability, e.g. Rayleigh Taylor instability [35, 36], parametrically driven instability [37], or directional instability of the ink jet by defects in the nozzle [38]. For a classic micromachined printhead developed at Océ Technologies B.V., it was shown before that dirt particles, transported by a flow of ink on the wetted nozzle plate, and moving layers of ink on the nozzle plate can induce bubble entrainment upon their interaction with a jetting nozzle [25]. However, it has been observed by the authors that the probability of bubble entrainment remains non-zero even for printheads with an anti-wetting nozzle plate that prevents transport of dirt particles and ink to jetting nozzles. Thus, not all physical mechanisms for bubble entrainment have been revealed yet.

In order to understand the bubble entrainment mechanism, it is key to visualize the bubble entrainment process at the microsecond timescale. The stochastic nature of the bubble entrainment process requires precise triggering to such an entrainment event. It has been shown that the piezo actuator can be used as a pressure sensor, and that changes of the ink channel acoustics can trigger a high-speed imaging recording [25]. Visualization is challenging since printheads fabricated through micromachining and printheads fabricated in silicon are opaque to visible light. Silicon is partly transparent to infrared (IR) light, allowing for infrared visualization of the inside of a MEMS-based ink channel [22]. Nevertheless, the high refractive index of silicon ($n = 3.42$) complicates IR-imaging of the nozzle region due to total (internal) reflection at the silicon interfaces [22]. Furthermore, to date, the maximum temporal resolution achieved by IR-cameras is only on the order of 1 ms whereas the jetting process, and thus the bubble entrainment process, takes place at the microsecond time scale. Thus, IR-imaging cannot be used to study bubble entrainment in MEMS-based printheads in real time.

Optical access to visible light has previously been obtained for a classic micromachined printhead by invasively adding an extra glass channel with a nozzle to the printhead [26]. Thereby, bubble entrainment in the ink channel could be visualized. However, the temporal resolution of the imaging system at that time was only 25 μs, i.e. one order of magnitude too low to image the bubble entrainment process itself. Another limitation at that time was that the powder blasting method, with which the ink channels were formed in the glass, was not capable of forming ink channels in the glass with accurate dimensions and with the shape of that of typical ink channels. The ink channels had an hourglass shape instead of a cylindrical shape, and were therefore invasive to the ink channel acoustics and the bubble entrainment process.

Here, a printhead was produced with an optically transparent glass nozzle plate (4.2.1). Stochastic bubble entrainment in a jetting ink channel was imaged simultaneously with the jetting process by using two high-speed cameras triggered on changes in the ink-channel acoustics (4.2.2, 4.2.3, and 4.3.1). Entrained bubbles were used as a pressure sensor (4.2.5 and 4.3.2), and their translation (4.3.3), as well as their growth and effect on the jetting process (4.3.4) were studied. Furthermore, particle tracking velocimetry experiments were used to study the convective flow inside the ink channel (4.2.7 and 4.3.5). The obtained flow field is used to explain the trajectories of dirt particles in front of the nozzle entrance (4.2.6 and 4.3.5). Finally, bubble entrainment was imaged at high driving amplitudes (4.2.8 and 4.3.6), and failure statistics were measured (4.2.9 and 4.3.7) in a first attempt to reveal the physical mechanism through which disturbing bubbles are entrained.

4.2 Experimental methods

4.2.1 Printhead and ink

An experimental printhead was produced with the help of Océ Technologies B.V. and Philips Innovation Services. The printhead had a silicon-based functional acoustic part connected to a 500 μm thick fused silica nozzle plate chip, see Fig. 4.1. Due to the unconventional character of this assembly it was inevitable to make this outside the cleanroom. This resulted in dirt particle polluted ink channels with a higher bubble entrainment probability than regular printheads.

The channel features in the fused silica chip were fabricated at a precision of 1 μm through femtosecond laser pulse printing and subsequent chemical etching (FemtoPrint, Muzzano, Switzerland). The channel shapes in this fused silica part were kept as simple as possible to keep it well defined. An anti-wetting coating consisting of self-assembled monolayers of (Tridecafluoro-1,1,2,2-tetrahydrooctyl)trichlorosilane (FOTS, abcr GmbH, CAS 78560-45-9) was applied to one side of the fused silica chip through which the imaging was performed such that the formation of an optically disturbing ink layer was prevented.

Figures 4.1(b) and 4.1(c) show side- and bottom micrographs of the channels in the fused silica chip. The nozzles were cylindrical with a diameter and length of 30 μm. Hot-melt ink (non-pigmented CrystalPoint$^{\mathrm{TM}}$, Océ Technologies B.V.) was jetted from the nozzle at a temperature of 130°C. At this temperature, the ink viscosity, density, and surface tension are 10 mPa·s, 1080 kg/m^3, and 28 mN·m, respectively.

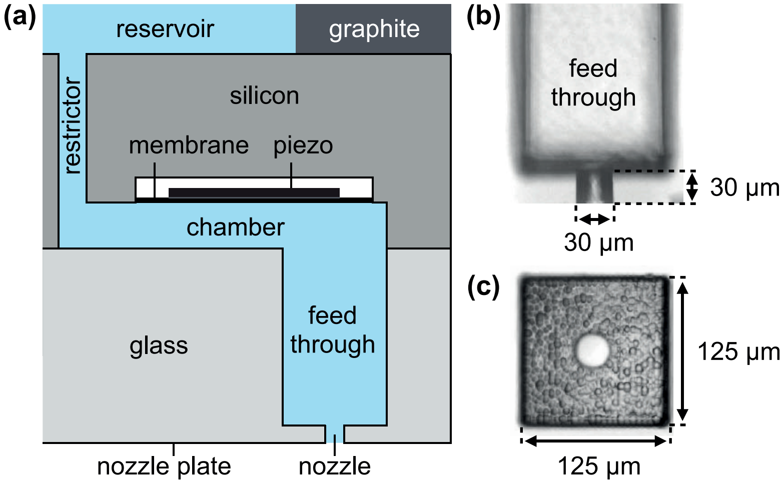

Figure 4.1: (a) Schematic side view of the ink channel in the silicon printhead with a glass nozzle plate. (b) Side view and (c) bottom view microscope images of the empty ink channel in the glass nozzle plate.

4.2.2 Imaging setup

The imaging setup, see Fig. 4.2, consisted of a modular microscope (BXFM-F, BXFM-ILHS, Olympus) equipped with a 20× (SLMPLN20x, Olympus) and a 50× (SLM-PLN50x, Olympus) magnifying objective. Due to the optical path length difference between the inside and the outside of the printhead, two high-speed cameras with a slightly different optical focus were used to image the inside of the ink-channel, and the droplet formation outside of the printhead, respectively. A 50-50% beamsplitter was used to display the microscope image on both high-speed camera 1 (HPV-X2, Shimadzu or FASTCAM SA-X2, Photron) and high-speed camera 2 (FASTCAM SA1.1, Photron). Camera 1 was optically focused on the inside of the printhead by adjusting the distance between the printhead and the microscope objective, while camera 2 was optically focused on the droplet formation by adjusting the length of tube lens 2. Illumination was provided by a continuous fiber-optic light source (Sumita LS-M352). During the experiments, the cameras were continuously recording using their ring memory. Once a trigger was received, the cameras stopped recording and the frames before and after the trigger pulse in their memory were used to reveal the bubble entrainment event. The temporal resolution at which the bubble entrainment could be visualized using the employed setup with the HPV-X2 camera and the continuous light source was 1 µs at a spatial resolution of 1.5 µm/pixel (20× magnification) and 2 µs at a spatial resolution of 0.6 µm/pixel (50× magnification). The temporal resolution was lower at the higher spatial resolution because of the limited available

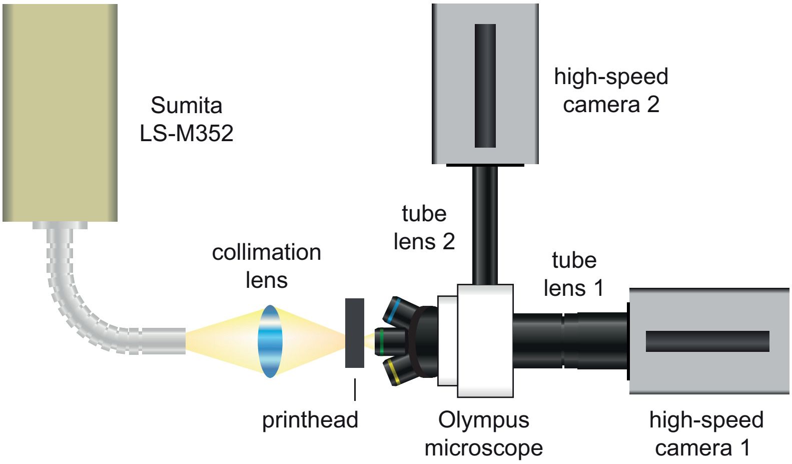

Figure 4.2: High-speed imaging setup employed to simultaneously visualize droplet formation and bubble entrainment.

illumination intensity. For the simultaneous recordings of bubble entrainment and droplet formation the SA-X2 and SA1.1 cameras were used, which both had a spatial resolution of 1.0 µm/pixel (20× magnification). The bubble entrainment was imaged by the SA-X2 camera at a temporal resolution of 5 µs, and the droplet formation was imaged by the SA1.1 camera at a temporal resolution of 12.5 µs, with a shutter time of 1 µs to avoid motion blur.

4.2.3 Piezo actuation and camera triggering system

A triggering system was developed that generates a trigger pulse once a bubble was entrained. Similarly to what has previously been reported [25], the trigger pulse was generated when a change in channel acoustics was detected. Here, a Field-Programmable Gate-Array (FPGA, National Instruments, NI PXI-7952R) was used to analyze the channel acoustics. The FPGA was programmed such that it generated a Pearson correlation factor for each piezo actuation pulse. Figure 4.3 shows a schematic representation of the triggering and piezo actuation system.

A pulse delay generator (Berkeley Nucleonics Corp., BNC 575) triggered an arbitrary waveform generator (AWB, Wavetek 195) at the 20 kHz DOD frequency. Furthermore, the pulse-delay generator sent a clock signal with a frequency of 10 MHz to the waveform generator to synchronize the two devices to avoid jitter on the FPGA sampling signal. Upon each trigger, the AWG produced three waveforms. The first waveform was the standby signal for the FPGA. The second waveform was a 2 MHz FPGA sampling signal consisting of 64 pulses corresponding to the 64 data points that the FPGA records per acoustic sensing signal. The third waveform was a trapezoidal

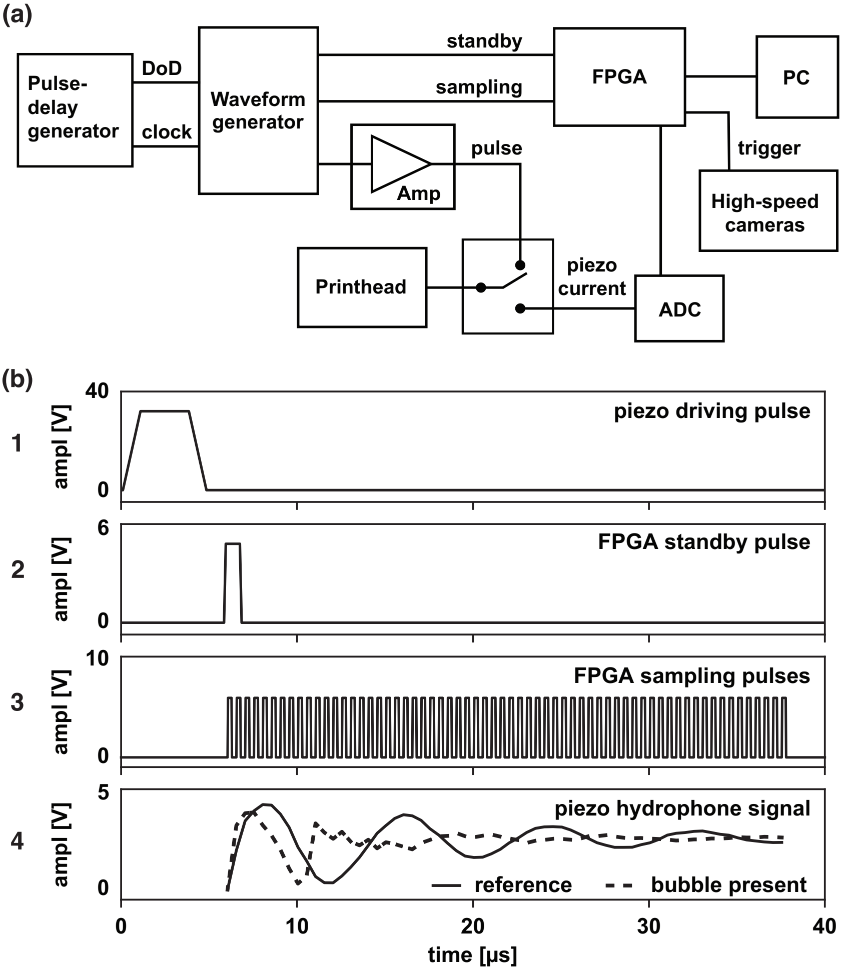

Figure 4.3: (a) Control system that actuates the printhead and monitors the ink channel acoustics to trigger the imaging system at a bubble entrainment event. (b-1-3) Waveforms created by the waveform generator. (b-4) Two piezo current signals measured by the FPGA, i.e. a reference signal and a signal in the case a bubble had been entrained

piezo-driving waveform with a rise and fall time of 1 µs and a high time of 3.0 µs, optimized for the ink channel Helmholtz resonance frequency of 125 kHz. The piezo actuation pulse was amplified to 38 V (10 m/s droplet velocity) by a wideband power amplifier (Krohn-Hite 7602M) during bubble entrainment experiments, and was connected to the printhead via a custom-made electronic switch. The switch connected the piezo driving pulse to the piezo and switched towards the analogue-digital-converter (ADC, National Instruments, NI 5732) once the piezo signal dropped below 1 V.

The digital signal was recorded by the FPGA and compared in real time to a reference signal that was obtained from a jetting nozzle before the experiment. A trigger pulse was generated once the correlation factor was smaller than 0.9. The FPGA firmware was programmed in the graphical programming language Labview (National Instruments) and compiled by a Xilinx compiler into a bit-file after which it was loaded to the FPGA. Moreover, during the experiments Labview was used to communicate with the FPGA via the PC.

4.2.4 Image analysis

The bubble dynamics was extracted from the high-speed movies using an automated image analysis algorithm programmed in MATLAB. The radius of a bubble was obtained from the inflection point of its intensity profile [39]. For each frame, the position of the bubble was stored to track its displacement over time.

The jet velocity was measured from high-speed recordings of the ink jet using a script programmed in MATLAB. The head of the droplet was carefully tracked over time and its velocity was measured at 500 µm distance from the nozzle exit.

4.2.5 Radial bubble dynamics

The radial dynamics of an acoustically driven bubble is described by a Rayleigh-Plesset type equation [32, 40]:

$$\rho\left(\ddot{R}R+\frac{3}{2}\dot{R}^2\right)=\left(P_0+\frac{2\sigma}{R_0}\right)\left(\frac{R_0}{R}\right)^{3\kappa}\left(1-\frac{3\kappa\dot{R}}{c}\right) \\ -P_0-P_A(t)-4\mu\frac{\dot{R}}{R}-\frac{2\sigma}{R}-\rho\frac{\partial}{\partial t}\left(\frac{\dot{R}R^2}{2d}\right) \quad (4.1)$$

where ρ is the ink density, R the instantaneous bubble radius, P_0 the hydrostatic pressure in the ink channel, σ the interfacial surface tension of the air-ink interface, R_0 the equilibrium bubble radius, κ the polytropic gas constant, c the speed of sound in the ink, $P_A(t)$ the acoustic pressure, μ the dynamic ink viscosity. The time-derivatives are denoted by the dots. The final term in Eq. 4.1 accounts for the vicinity of a rigid wall with d the distance of the bubble center to the wall [40], to approximate the effect of the ink channel wall. Here, d was taken as the distance between the center of the bubble and the nearest wall during the measurement, i.e. the bottom of the feedthrough.

Equation 4.1 can be linearized to obtain the resonance frequency f_R of a bubble at a wall, i.e. for $d = R$, as follows: [32, 40]

$$f_R = \frac{0.8}{2\pi}\sqrt{\frac{1}{\rho R_0^2}\left(3\kappa P_0 + (3\kappa - 1)\frac{2\sigma}{R_0}\right)} = 0.8 f_0. \tag{4.2}$$

With f_0 the resonance frequency of a bubble in an unbounded fluid. Thus the resonance frequency of the bubble at a rigid wall decreases by a factor of 0.8.

Equation 4.1 can be fitted to the measured radial dynamics of a bubble inside an ink channel to obtain the acoustic driving pressure. The trapezoidal piezo actuation pulse drives the ink channel into resonance such that the acoustic driving pressure pulse in the ink channel may be approximated by a sinusoid multiplied by a Gaussian, as follows:

$$P(t) = P_A \sin(\omega t) \exp\left[-\frac{1}{2}\left(\frac{t - t^*}{\Omega}\right)^2\right], \tag{4.3}$$

where P_A is the pressure amplitude, $\omega = 2\pi f$ the frequency of the sinusoid in radians, t is time. The variance of the Gaussian Ω and the time at which it is at maximum t^* were fitting parameters. The function *fminsearch* in Matlab was used to find the driving pressure pulse that resulted in a best fit of Eq. 4.1 to the measured radial bubble dynamics.

4.2.6 Dirt particle position probability distribution

Experiments were also performed in an undisturbed ink channel, to study the behavior of the dirt particles present in the ink. The probability distribution of the dirt particle positions in the ink channel was obtained from a 10-minute optical recording of an ink channel jetting droplets at a drop-on-demand frequency of 20 kHz and a velocity of 8 m/s. Imaging was performed using the SA-X2 camera at a spatial resolution of 0.4 µm/pixel (50× magnification), at a frame rate of 1 fps, and with an exposure time of 2.5 µs. The recorded images were processed offline in MATLAB to measure the particle positions. To that end, the images were first divided by a background image in which no dirt particles were present. Then the images were binarized and noise was removed by excluding regions smaller than 5 pixels (3 µm) for further analysis. It was verified that the typical dirt particle size was larger than 5 µm. The location of the detected particles were stored in a matrix. Finally, the number of particles detected in grid cells of 3 µm × 3 µm were measured from this position matrix to find the probability of the dirt particle positions in the ink channel.

4.2.7 Particle tracking velocimetry

To explain the observed dirt particle trajectories and position probability distribution, the flow of the ink in the channel was studied through particle tracking velocimetry measurements by adding 0.01 vol % of 1 µm diameter SiO particles to the hot-melt ink. For this purpose, the ink was first melted on a hotplate at 130°C. Then, the SiO particles were added and thoroughly dispersed using a tip sonicator (Branson Sonifier, etc). SiO particles were chosen since they do not melt at the operating temperature of the printhead of 130°C.

The ink channel filled with the particle-laden ink was imaged at a frame rate of 50 kfps and with a shutter time of 5 µs using the HPV-X2 camera at a spatial resolution of 0.6 µm/pixel (50× magnification). The velocity field was measured from the movie frames in an automated way using a custom-made MATLAB script. First, each image was divided by a background image of the ink channel without particles. The resulting image was binarized using an intensity threshold. For each high-speed movie frame, the detected particle positions were stored in a matrix. The resulting position matrix was processed using a tracking algorithm [41] to track individual particles over the frames. The time-averaged velocity field in the ink channel was obtained by averaging the calculated particle velocity over a grid of 10 × 10 pixels (6 × 6 µm).

4.2.8 Bubble nucleation at a high driving amplitude

The imaging setup with the continuous light source was not able to capture all important details of the bubble nucleation process because the maximum frame rate at which bubble nucleation could be recorded at sufficient image quality, 1 Mfps, was limited by the brightness of the continuous light source. Therefore additional bubble nucleation events were recorded at a higher frame rate of 5 Mfps using the HPV-X2 camera at a spatial resolution of 0.6 µm/pixel (50× magnification), and using a brighter light source, i.e. a xenon strobe. However, as a result of the limited maximum flash rate of the xenon strobe (10 Hz), the printhead had to be operated far outside the regular operating range for nozzle failure to occur within a reasonable amount of time. The flashes were fired exactly at the start of the first meniscus retraction during every actuation cycle, thereby limiting the DOD frequency to 10 Hz, which is 2000 times lower than the typical DOD frequency. The employed jet velocity was fixed at almost 20 m/s, twice the typical regular jet velocity, such that on average only 9000 droplets had to be jetted before nozzle failure, corresponding to 15 minutes.

4.2.9 Nozzle failure statistics

In an attempt to reveal the nature of the bubble nucleation mechanism, the statistics of nozzle failure was measured as a function of the jet velocity. Therefore, first, the jet velocity was characterized as a function of the piezo driving voltage using high-speed imaging. Failure statistics are typically plotted as a function of jet velocity to aid comparison of failure statistics measured for different printheads with a potentially different piezo sensitivity. Then, the number of successfully jetted droplets before nozzle failure was measured as a function of the piezo driving voltage. Therefore, first, a high-speed recording at 200 fps was started using the SA-X2 camera at a spatial resolution of 0.4 µm/pixel (50× magnification). Then, the jetting process and the acoustic triggering system were started. Once the correlation factor of the acoustic signal dropped below 0.8 for a duration of 10 actuation cycles, the camera was triggered to stop recording. Note that only the cases were the nozzle completely failed were considered, i.e. the cases for which the bubbles were jetted outward within 10 actuation cycles were not considered. The number of successfully jetted droplets was then calculated from the time between the frame number at which the channel was first actuated until the frame number at which a nucleated bubble was visible for the first time, and from the DOD frequency. Given the 20 kHz DOD frequency and 200 fps recording rate, the error in the number of jetted droplets was 100. At each driving voltage, the failure experiment was repeated ten times.

4.3 Results

4.3.1 Air entrainment by bubble nucleation on a dirt particle

Figures 4.4(a) and 4.4(c) show typical bubble entrainment events imaged at a temporal resolution of 2 µs using the continuous light source and a shutter time of 2 µs. The timing of the piezo actuation pulse, the meniscus position, and the entrainment events are shown in Fig. 4.4(b). Note that in both cases a dirt particle is present that translates towards the oscillating meniscus. Once the particle is located close to the meniscus, a bubble nucleates on the dirt particle. Note that for both nucleation events, the nucleation bubble becomes visible at the start of the second meniscus retraction of the actuation cycle. During the next actuation cycle, the bubble detaches from the particle and translates towards a wall of the ink channel. In total, more than 50 bubble nucleation events were imaged, and in all cases at least one dirt particle was present close to the meniscus during bubble nucleation (see Section 4.3.5 for more information on the dirt particles). Furthermore, in 83% of all imaged nucleation events, the bubble appeared at the start of the second meniscus retraction. In the rest of the cases the bubble appeared at the start of the first meniscus retraction of an actuation cycle.

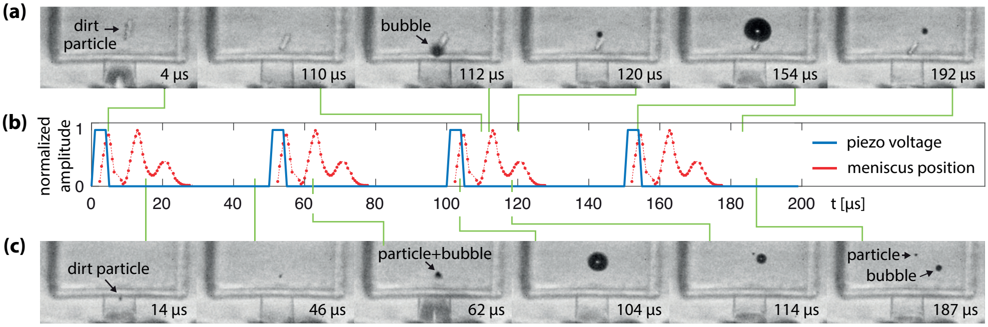

Figure 4.4: (a) and (c) show typical bubble nucleation events. A dirt particle translates towards the jetting meniscus and a bubble nucleates *on* the particle. After the next actuation cycle the bubble and particle separate. (b) Timing of the piezo actuation pulse and the meniscus position. The timing at which the images in (a) and (c) were taken with respect to the actuation pulse and corresponding meniscus motion is indicated by the solid green lines. The corresponding movies are included in the supplementary material.

4.3.2 The nucleated bubble as a pressure sensor

The radial dynamics of a nucleated bubble were measured at a temporal resolution of 1 µs using a shutter time of 500 ns, see Fig. 4.5(a), and were used to derive the driving pressure pulse inside the ink channel. The measured radial dynamics and the fitted radial dynamics are plotted in Fig. 4.5(b) for the first piezo actuation pulse at which the bubble was visible. Figures 4.5(c) and 4.5(d) show the measured and the fitted radial bubble dynamics for the second and fourth piezo actuation pulse after the bubble appeared. Note that the equilibrium bubble size R_0 increased over the 4 piezo actuations from 1.3 µm, to 1.7 µm, to 2.1 µm, to 2.2 µm, respectively, a result of rectified diffusion [31–34]. Also note that in all cases the second bubble expansion is of larger amplitude than the first one. Therefore, the rarefaction pressure is larger during the second meniscus retraction. Indeed, the obtained driving pressure pulses (Fig. 4.5(e)) show that the rarefaction pressure during the first meniscus retraction was 125 kPa and that during the second meniscus retraction was 150 kPa. The higher rarefaction pressure during the second meniscus retraction may explain the higher bubble nucleation probability that was reported in the previous section. Furthermore, note that the frequency of the acoustic driving pressure pulses decreased by 18%, namely from 125 kHz to 102 kHz, after the first actuation pulse. Thus the nucleated bubble decreased the eigenfrequency of the ink channel. The frequency and amplitude of the driving pressure pulse did not change during the 2 subsequent actuation pulses.

Figures 4.5(b)-(d) show that the bubble oscillations in the ink channel are highly nonlinear, with bubble expansions more than 7 times larger than the equilibrium

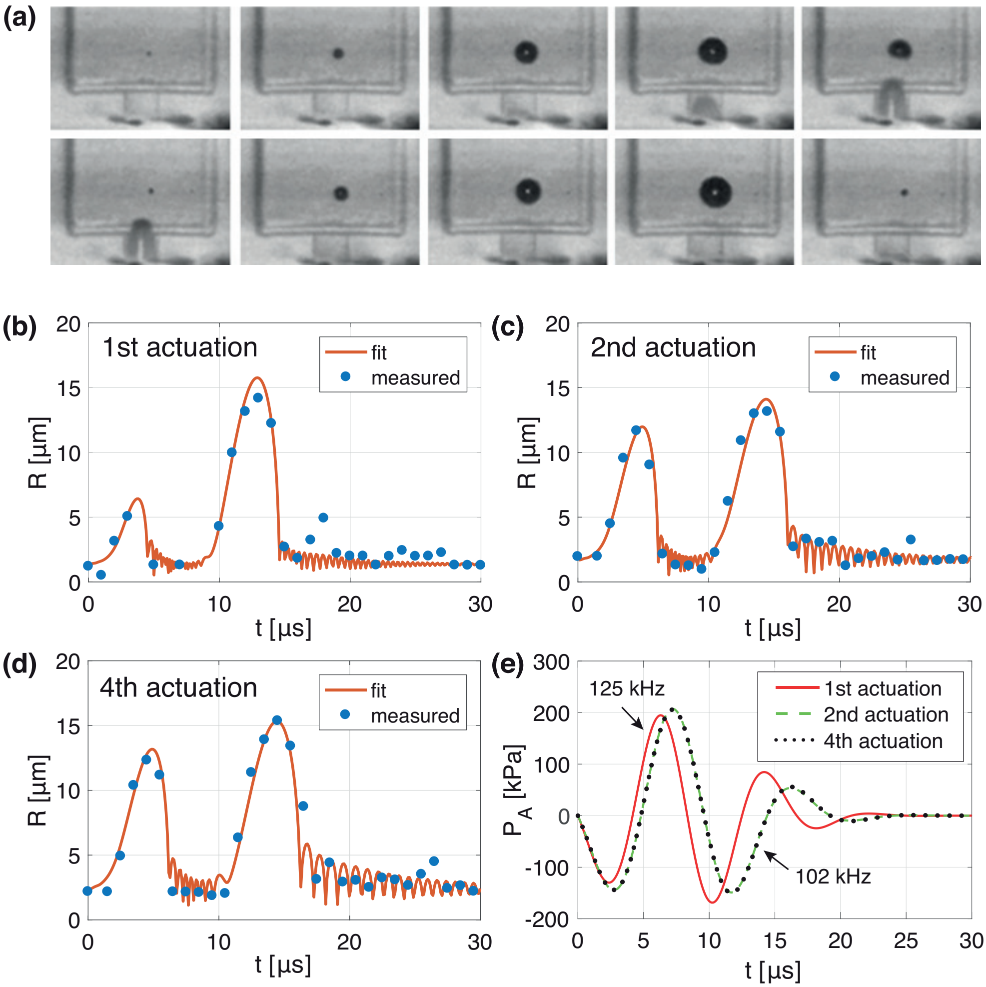

Figure 4.5: (a) Radial dynamics of a nucleated bubble recorded at a temporal resolution of 1 µs. (b) Measured and fitted radial dynamics for a nucleated bubble during (b) the first actuation, (c) the second actuation, and (d) the fourth actuation after bubble appearance. (e) Acoustic driving pressure as function of time, calculated with the Rayleigh-Plesset equation based on the fitted radial bubble dynamics.

bubble size, resulting in an inertial bubble collapse [34]. Note from the modelled curves that after the collapse, the bubbles ring down at a much higher frequency than the frequency of the driving ultrasound pulse. Indeed, using Eq. 4.2 it can be calculated that the resonance frequency of a microbubble with a radius on the order of 2 µm is 1.4 - 1.8 MHz, depending on the standoff distance to the wall, i.e. one order of magnitude higher than the frequency of the ink channel acoustics. In this calculation, a polytropic exponent of 1.4 was used, assuming air-filled bubbles and adiabatic bubble oscillations. Thus, as expected, the resonance frequency of the bubble is much larger than that of the Helmholtz resonance frequency of the ink channel.

4.3.3 Bubble translation

The initial location at which the bubble nucleates determines its translational path through the ink channel. Figure 4.6 shows the translation of the nucleation bubble for 6 different bubble nucleation events, imaged at a temporal resolution of 2 µs using a shutter time of 1 µs. The translation direction is indicated by the arrows. Note that the cross-section of the feedthrough is square and that the translational motion of the bubble may in part be out of the imaging plane. The nucleated bubbles first translate upstream into the ink channel (positive y-direction). During the subsequent actuation cycles, the bubble can be jetted outwards (purple, red, and blue curve) or it can be entrained into the ink channel through its translation towards a channel wall (light blue, green, and yellow curve). The distance between the grouped data points in Fig. 4.6 indicates the distance over which the nucleation bubbles translated during one actuation cycle. For the measurements given in Figure 4.6 the bubbles arrive at a channel wall within 15 actuation cycles, i.e. within 750 µs.

4.3.4 Jet formation during bubble nucleation and growth

In this section, the role of bubble nucleation and bubble growth on inkjet formation is investigated. Two high-speed cameras were used to image both the jet formation outside the printhead and the bubble nucleation events inside the ink channel. Figure 4.7(a) shows an image sequence of the inkjet before, during, and after the nucleation of a bubble. Figure 4.7(b) shows the inside of the ink channel with a dirt particle on which a bubble nucleates at t = 0.98 ms. The first droplet that is formed after bubble nucleation (t = 1.0 ms) is 24% longer than the droplet formed under normal conditions (t = 0.0 ms).

After nucleation, the bubble translates out of the imaging plane towards the channel wall where it arrives at t = 2.3 ms. The bubble grows over time (red dots in Fig. 4.7(c)) and at t = 12 ms it breaks up into two bubbles that both translate towards the left corner of the channel where they arrive at t = 14.9 ms. To show that the nucleation and growth of a bubble is a non-universal process, also a second bubble entrainment

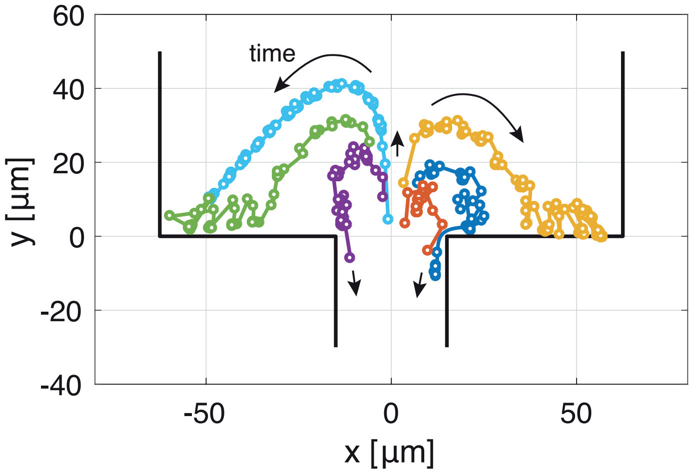

Figure 4.6: Translational movement of nucleated bubbles. The initial nucleation location determines whether bubbles are jetted outward (purple, red, and blue curve), or translate into the ink channel (light blue, green, and yellow curve).

case is plotted in Fig. 4.7(c). Qualitatively, case 1 and 2 correspond well, i.e. a bubble nucleates, grows, and breaks up into two bubbles. However, the growth rate and breakup time are different.

The growing bubbles decrease the jet velocity as can be seen in Fig. 4.7(d) where the jet velocity is plotted as a function of time for both nucleation cases. For case 1, after bubble nucleation, the jet velocity first slightly increases (3%) before it starts decreasing whereas for case 2 the jet velocity decreases directly after bubble nucleation. For case 1, the jet velocity increases at $t = 9$ ms and for case 2 it continues to decrease over time. Despite the measured differences in bubble growth and jet velocity, Fig. 4.7(e) shows that for both cases the total bubble volume versus jet velocity curves seem to be correlated, however more experimental data is required for verification. This shows that jet velocity is directly correlated to the total gas volume in the ink channel.

4.3.5 Dirt particle trapping and ink velocity field

In this subsection, we show that dirt particles present in the ink channel may get trapped in the region in front of the nozzle. A typical example of the translation of a dirt particle that was trapped is plotted in Fig. 4.8(a). Note that the dirt particle originated from the ink upstream of the feedthrough. Once the dirt particle approached the nozzle, it entered a spiral directed inwards to a fixed point in front of the nozzle. Also note in Fig. 4.8(a) that there are 2 more dirt particles present at the same distance

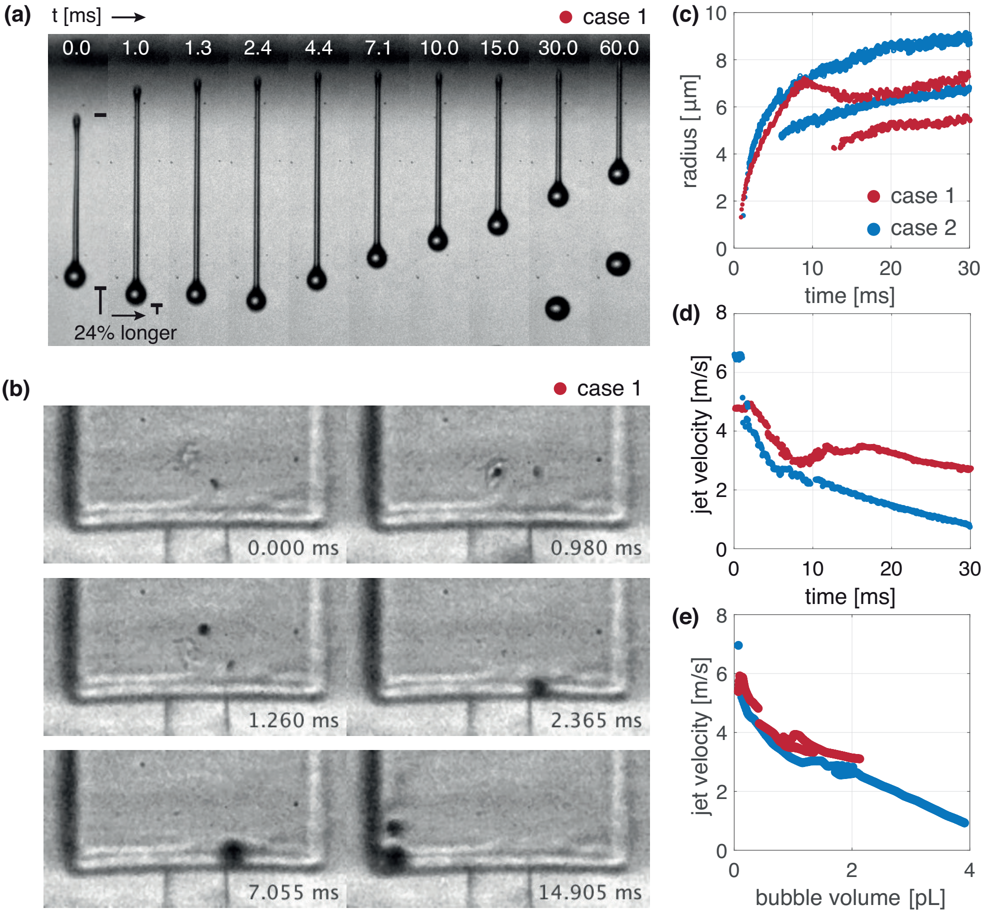

Figure 4.7: (a) Image sequence of a jetting nozzle during the nucleation and growth of a bubble. (b) The bubble nucleation and growth was imaged simultaneously with the jetting nozzle. The bubble nucleated at $t = 0.98$ ms. (c) Bubble radius as a function of time for two nucleation events. In both cases, the nucleated bubble splits into two bubbles after several ms, probably due to fragmentation as a result of jet formation in the bubble during strong asymmetric collapse towards the wall [33]. (d) Jet velocity as a function of time. (e) The total bubble volume versus the jet velocity curves of both cases seem to collapse on the same curve.

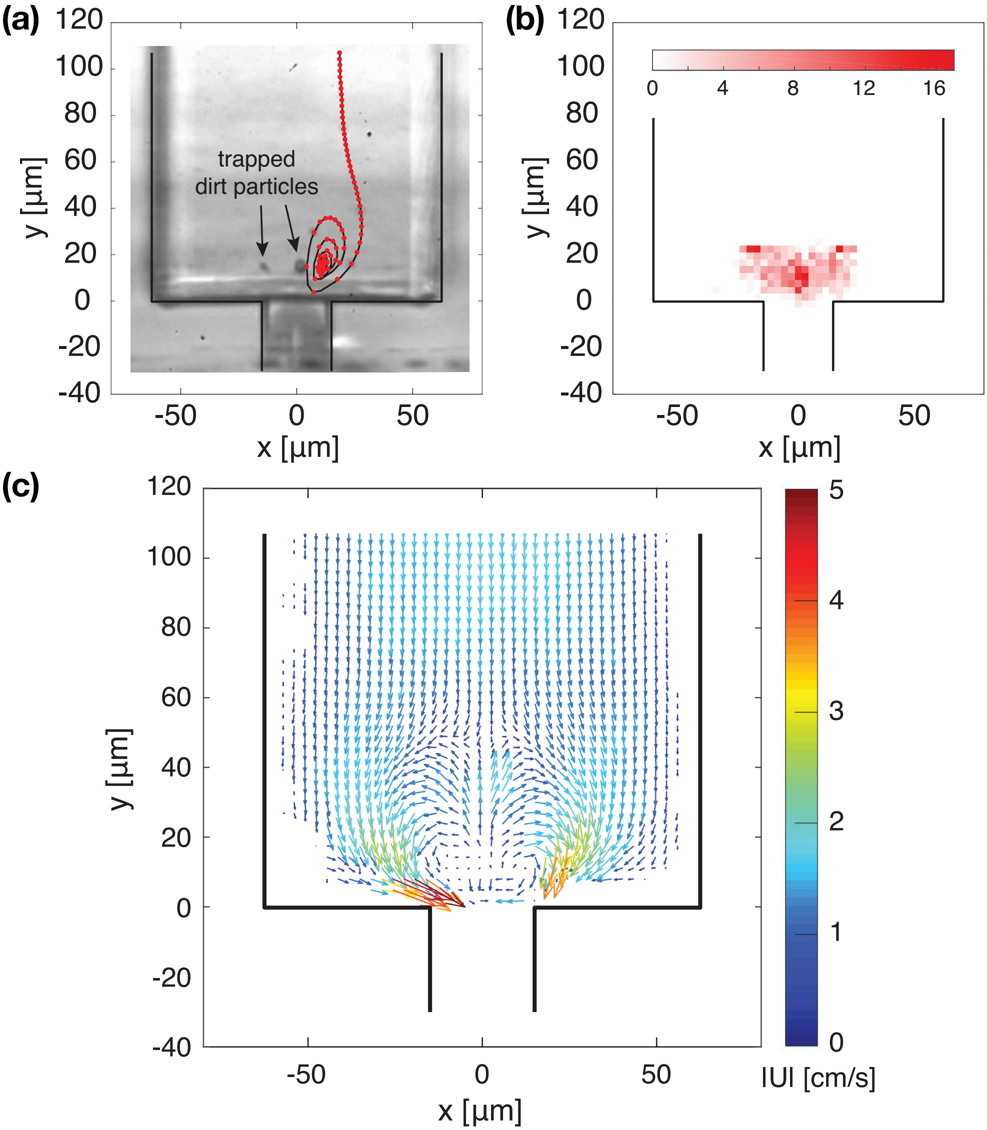

Figure 4.8: (a) Path of a dirt particle that gets trapped in a region in front of the nozzle, recorded at a framerate of 10 kfps and with a shutter time of 5 µs. (b) Dirt particle position probability distribution based on 680 dirt particle positions. The color indicates the number of particles found in the grid cell. (c) Time averaged velocity field inside the ink channel measured by PTV, showing a vortex ring in front of the nozzle.

from the nozzle entrance (indicated by the arrows).

In total, the location of 680 dirt particles was measured from images of a jetting nozzle. Figure 4.8(b) shows the probability of the dirt particle positions inside the ink channel. The color indicates the number of particles found in a grid cell. Clearly, dirt particles are trapped in front of the nozzle in a region with a projected area (h×w) of approximately 25 µm × 50 µm.

To explain the entrapment of dirt particles in front of the nozzle, the time averaged flow velocity field in an ink channel without bubbles was measured using particle tracking velocimetry (PTV). The results are presented in Fig. 4.8(c). In front of the nozzle with the oscillating meniscus, a vortex ring is observed, i.e. in the center of the ink channel, the flow is directed upwards in positive y-direction, and it recirculates off-axis. Such a vortex ring is a well-known phenomenon, and is described in detail in for example refs. [42–44]. Note, by comparison of Fig. 4.8(a) and 4.8(c), that the dirt particles were trapped in the center of the vortex ring where the recirculation velocity is at minimum.

To estimate the density of the dirt particles and the physical trapping mechanism, the terminal sedimentation velocity of approximately spherical dirt particles was measured at a frame rate of 60 fps in a non-actuated ink channel. The particles considered had diameters ranging from 5 µm to 12 µm. By equating the Stokes drag to the gravitational force, the particle density was calculated to be approximately 2500 kg/m^3, i.e. 2.3 times higher than the density of the surrounding ink. It is very surprising that these relatively heavy particles are stably trapped in the center of the vortical flow, because normally heavy particles are thrown out of a vortical flow by the centrifugal force. See also the discussion in Section 4.4.

4.3.6 Bubble nucleation by cavitation

In a first attempt to reveal the mechanism by which a bubble nucleates on a dirt particle, the nucleation event during a high amplitude driving pulse was imaged at 5 million fps using a xenon single flash light source and a shutter time of 110 ns. Figure 4.9 shows a typical image sequence of a bubble nucleation event. Note that the ink contains seeding particles, and note the dirt particle near the nozzle entrance in the first frame at t = 0 µs. During the first meniscus retraction, the dirt particle remains located at the channel wall and it does *not* come into direct contact with the meniscus. When the meniscus moves outwards, the inkjet is formed and the flow of ink drags along the dirt particle into the nozzle, see t = 6.2 µs. When the particle moves past the sharp corner into the nozzle, a bubble cavitates on the particle due the low local hydrostatic pressure resulting from the high local ink velocity. Thus, it is shown here that, at this extreme high driving amplitude, dirt particles do not have to be in direct contact with the ink-air meniscus to nucleate a bubble.

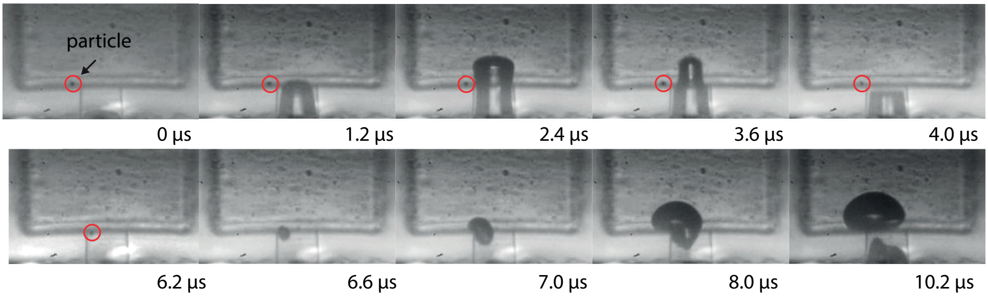

Figure 4.9: Cavitation on a particle. The meniscus retracts for the first time and subsequently ejects a droplet. The ejection of an ink jet results in the acceleration of the ink. The particle, initially located at the wall, is dragged along by the ink, first towards the nozzle, then around the edge into the nozzle. The increased ink velocity in the nozzle results in a low hydrostatic pressure initiating bubble nucleation on the dirt particle starting at $t = 6.6$ µs.

4.3.7 Nozzle failure statistics

To further characterize the bubble nucleation mechanism, the nucleation probability was studied as a function of the driving amplitude of the ink channel. Before the nucleation probability was studied, the dependence of the jet velocity and the meniscus amplitude were studied as a function of the piezo driving amplitude. First, Fig. 4.10(a) shows that the jet velocity is approximately linearly dependent on the driving amplitude of the piezo. Figure 4.10(b) shows the maximum meniscus retraction, or inward amplitude, with respect to the nozzle exit. The figure shows that the inward meniscus amplitude is also approximately linearly dependent on the driving voltage of the piezo.

The nozzle failure probability measured as a function of the jet velocity is shown in the boxplot in Fig. 4.10(c). The stability of the inkjet printing process was measured at 7 different jet velocities by measuring at each jet velocity, for 10 times, the number of droplets that could be successfully jetted before bubble nucleation. In Fig. 4.10(c), for each data set per jet velocity, the lowest measured probability is represented by the lower horizontal bar, the first quartile by the lower value of the box, the median by the bar inside the box, the 3th quartile by the upper limit of the box, and the maximum measured value by the upper horizontal bar. Note that the nozzle failure probability increases approx. exponentially with the jet velocity over the measured jet velocity range. In a future study it could be investigated whether this exponential relation can be explained using the classical nucleation theory [45, 46]. This theory predicts the bubble nucleation rate through an exponential function of which the value of the exponent depends on the liquid pressure. Experimentally, the applicability of the classical nucleation theory could be tested in an acoustic characterization setup.

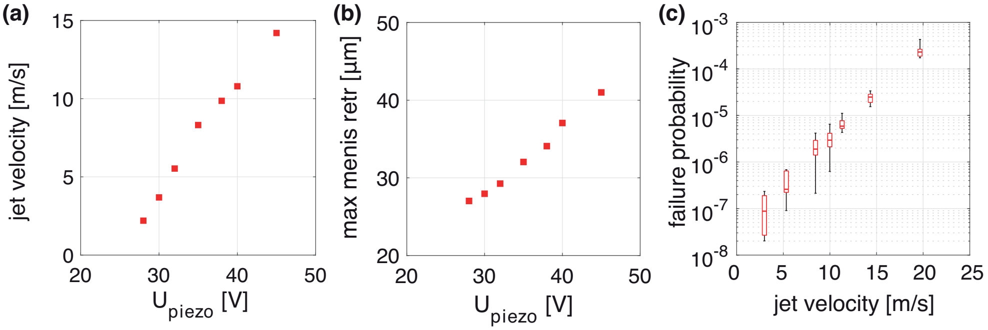

Figure 4.10: (a) Jet velocity and (b) maximum meniscus retraction as function of piezo driving pulse amplitude. (c) Measured failure statistics as a function of the jet velocity. For each data set per jet velocity, the lowest measured probability is represented by the lower horizontal bar, the first quartile by the lower value of the box, the median by the bar inside the box, the 3th quartile by the upper limit of the box, and the maximum measured value by the upper horizontal bar. The high dirt particle concentration resulted in a high failure probability as compared to standard printheads produced using cleanroom facilities.

This setup needs to contain ink from the printhead, including dirt particles, and send pressure pulses into the ink using a ultrasound transducer. The amplitude and length of these pressure pulses then need to be varied to obtain the nucleation rate as function of acoustic pressure.

4.4 Discussion

In this work, it was shown that bubbles nucleate on dirt particles (Fig 4.4). The affinity of the gas with the dirt particles, and the observed cavitation on the particles, suggests that the dirt particles were inkophobic or at least only partially wetting. As a result, nucleation sites are always present on the particles, i.e. formed through diffusion of dissolved gas towards the dirt particles. Moreover, the measured density of 2500 kg/m^3 suggests that the dirt particles were composed of silicon or glass, likely originating from the unconventional printhead assembly.

Due to the density mismatch of the dirt particles with the surrounding ink, the dirt particles may penetrate the meniscus interface to directly grab air from outside the ink. To investigate this, the Stokes number is calculated, as follows [47]: $Stk = t_0 u_0 / l_0$, where $t_0 = \rho_p d_p^2 / 18\mu$ is the relaxation time of the particle, u_0 the ink velocity, and l_0 the particle diameter (6 to 8 µm). The maximum ink velocity is assumed to be twice the jet velocity (5 to 10 m/s). The resulting Stokes number is 1.0 to 2.0. Thus, indeed, a dirt particle close to the nozzle may get into direct contact with the meniscus since it does not closely follow the streamlines during fast advancement and retraction of the meniscus.

Apart from bubble nucleation through direct interaction of dirt particles with the meniscus, it was shown in Figure 4.9 that bubble nucleation is also possible through cavitation, i.e. without direct interaction. The increased ink velocity in the nozzle decreases the pressure according to Bernoulli's law [48], and the pressure drop triggers the nucleation. However, these cavitation experiments were performed at twice the normal driving amplitude and therefore, the nucleation mechanism may be different for a printhead operated under normal conditions.

In this work, dirt particles were shown to be trapped in the vortex in front of the nozzle. This trapping is surprising since the centrifugal force on the particles with a density higher than that of the ink is directed away from center of the vortex [49]. A possible explanation for this discrepancy is that that the shear gradient lift force and/or the rotational lift force [49–51] are the dominating trapping forces. Future work should focus on understanding the trapping forces using numerical simulations.

The translational paths of the nucleated bubbles can be qualitatively explained from a combination of acoustic radiation forces and hydrodynamic forces [32, 52, 53]. The freshly nucleated bubble is pushed into the ink channel by two mechanisms. First, the primary radiation force pushes the non-resonant bubble into the ink channel, towards the pressure node at the piezo, where the acoustic pressure amplitude is higher than that at the nozzle entrance. Second, the convective ink flow (Fig. 4.8(c)) drags along the nucleation bubble upwards into the ink channel. Then, the secondary radiation force becomes dominant on the bubble that has now grown due to rectified diffusion such that it is forced towards the acoustically reflective channel walls [54]. This hypothesis, and the relative influence of acoustic and hydrodynamic forces will be validated through numerical modelling in future work.

The length of the jet formed after bubble nucleation was observed to increase by 24% whereas the jet velocity increased by only 3% (Fig. 4.7). The increased jet length can be explained from the decrease in the frequency of the acoustic driving pressure wave inside the ink channel. The acoustic driving frequency was measured to decrease by 18% after bubble nucleation. The decreased driving frequency and corresponding meniscus motion result in an extension of the time window over which ink is ejected out of the ink channel by 18%; in other words the droplet formation process takes 18% longer. Together with the 3% higher jet velocity, also resulting in a longer ink jet, a 22% longer jet is expected which agrees well with the measured 24% increase in jet length. At longer timescales, the jet velocity decreases due to the compressibility of the bigger gas bubble which prevents pressure buildup at the nozzle [26].

4.5 Conclusions

Stochastic air bubble entrainment and droplet formation were visualized simultaneously in an optically transparent piezo-acoustic inkjet printhead through high-speed imaging. The high speed cameras were triggered on the changes in the ink channel acoustics due to bubble entrainment. It was found that dirt particles trigger bubble nucleation upon their interaction with the oscillating meniscus. The driving pressure pulse in the ink channel was measured from a fit of the measured radial bubble dynamics to the Rayleigh-Plesset equation. After nucleation, the bubble translates into the ink channel, separates from the dirt particle, and either moves to a corner of the ink channel or returns to the nozzle where it is jetted outward. The nucleated bubble causes the ink jet to be temporarily 24% longer, mainly due to a corresponding decrease in the ink channel resonance frequency.

The dirt particles originated from inside the ink channel. Moreover, they were trapped in a vortex flow in front of the nozzle thereby increasing the particle-meniscus interaction probability. The ink velocity field was characterized using particle tracking velocimetry. The measured nozzle failure statistics reveal an exponential relation between jet velocity and the nozzle failure probability. Cavitation on a particle during a rarefaction pressure wave, and direct contact of a particle with the meniscus during fast advancement and retraction of the meniscus, were identified as possible mechanisms through which a bubble nucleates.

References

[1] H. Wijshoff, “The dynamics of the piezo inkjet printhead operation”, Physics Reports **491**, 77–177 (2010).

[2] S. D. Hoath, *Fundamentals of Inkjet Printing: The Science of Inkjet and Droplets* (Wiley-VCH Verlag GmbH & Co. KGaA) (2015).

[3] N.-T. Nguyen and S. Wereley, *Fundamentals and Applications of Microfluidics* (Artech House, Inc.) (2002).

[4] S. Majee, M. Song, S.-L. Zhang, and Z.-B. Zhang, “Scalable inkjet printing of shear-exfoliated graphene transparent conductive films”, Carbon **102**, 51–57 (2016).

[5] S. Majee, C. Liu, B. Wu, S.-L. Zhang, and Z.-B. Zhang, “Ink-jet printed highly conductive pristine graphene patterns achieved with water-based ink and aqueous doping processing”, Carbon **114**, 77–83 (2017).

[6] S. Eshkalak, A. Cinnappan, W. Jayathilaka, M. Khatibzadeh, E. Kowsari, and S. Ramakrishna, “A review on inkjet printing of CNT composites for smart applications”, Applied Materials Today **9**, 372–386 (2017).

[7] M. Vilardell, X. Granados, S. Ricart, I. V. Driessche, A. Palau, T. Puig, and X. Obradors, “Flexible manufacturing of functional ceramic coatings by inkjet printing”, Thin Solid Films **548**, 489–497 (2013).

[8] A. Moya, G. Gabriel, R. Villa, and F. J. del Campo, “Inkjet-printed electrochemical sensors”, Current Opinion in Electrochemistry **3**, 29–39 (2017).

[9] T. Eggenhuisen, Y. Galagan, E. Coenen, W. Voorthuijzen, M. Slaats, S. Kommeren, S. Shanmuganam, M. Coenen, R. Andriessen, and W. Groen, “Digital fabrication of organic solar cells by inkjet printing using non-halogenated solvents”, Solar Energy Materials and Solar Cells **134**, 364–372 (2015).

[10] S. Hashmi, M. Ozkan, J. Halme, K. Misic, S. Zakeeruddin, J. Paltakari, M. Grätzel, and P. Lund, “High performance dye-sensitized solar cells with inkjet printed ionic liquid electrolyte”, Nano Energy **17**, 206–215 (2015).

[11] T. Shimoda, K. Morii, S. Seki, and H. Kiguchi, “Inkjet printing of light-emitting polymer displays”, Inkjet Printing of Functional Materials **28**, 821–827 (2003).

[12] C. Jiang, L. Mu, J. Zou, Z. He, Z. Zhong, L. Wang, M. Xu, J. Wang, J. Peng, and Y. Cao, “Full-color quantum dots active matrix display fabricated by ink-jet printing”, Science China Chemistry **60**, 1349–1355 (2017).

[13] R. Daly, T. Harrington, G. Martin, and I. Hutchings, “Inkjet printing for pharmaceutics - a review of research and manufacturing”, International Journal of Pharmaceutics **494**, 554–567 (2015).

[14] A. Simaite, F. Mesnilgrente, B. Tondu, P. Souères, and C. Bergaud, “Towards inkjet printable conducting polymer artifical muscles”, Sensors and Actuators B: Chemical **229**, 425–433 (2016).

[15] S. Hewes, A. Wong, and P. Searson, “Bioprinting microvessels using and inkjet printer”, Bioprinting **7**, 14–18 (2017).

[16] M. Nakamura, A. Kobayashi, F. Takagi, A. Watanabe, Y. Hiruma, K. Ohuchi, Y. Iwasaki, M. Horie, I. Morita, and S. Takatani, “Biocompatible inkjet printing technique for designed seeding of individual living cells”, Tissue Engineering **11**, 1658–1666 (2005).

[17] G. Villar, A. Graham, and H. Bayley, “A tissue-like printed material”, Science **340**, 48–52 (2013).

[18] B. Derby, “Additive manufacture of ceramic components by inkjet printing”, Engineering **1**, 113–123 (2015).

[19] A. Khalate, X. Bombois, G. Scorletti, R. Babuska, S. Koekebakker, and W. de Zeeuw, “A waveform design method for a piezo inkjet printhead based on robust feedforward control”, Journal of Microelectromechanical Systems **21**, 1365–1374 (2012).

[20] C. Menzel, A. Bibl, and P. Hoisington, “MEMS solutions for precision microfluidic dispensing application”, Technical Report, Fujifilm Dimatix Inc. (2004).

[21] B.-H. Kim, T.-G. Kim, T.-K. Lee, S. Kim, S.-J. Shin, S.-J. Kim, and S.-J. Lee, “Effects of trapped air bubbles on frequency responses of the piezo-driven inkjet printheads and visualization of the bubbles using synchrotron X-ray”, Sensors and Actuators A: Physical **154**, 132–139 (2009).

[22] A. van der Bos, T. Segers, R. Jeurissen, M. van den Berg, H. Reinten, H. Wijshoff, M. Versluis, and D. Lohse, “Infrared imaging and acoustic sizing of a bubble inside a micro-electro-mechanical system piezo ink channel”, Journal of Applied Physics **110**, 034503 (2011).

[23] B.-H. Kim, H.-S. Lee, S.-W. Kim, P. Kang, and Y.-S. Park, “Hydrodynamic responses of a piezoelectric driven MEMS inkjet print-head”, Sensors and Actuators A: Physical **210**, 131–140 (2014).

[24] J. Dijksman, “Hydro-acoustics of piezoelectrically driven ink-jet print heads”, Flow, Turbulence and Combustion **61**, 211–237 (1998).

[25] J. de Jong, G. de Bruin, H. Reinten, M. van den Berg, H. Wijshoff, M. Versluis, and D. Lohse, “Air entrapment in piezo-driven inkjet printheads”, Journal of the Acoustical Society of America **120**, 1257–1265 (2006).

[26] J. de Jong, R. Jeurissen, H. Borel, M. van den Berg, H. Wijshoff, H. Reinten, M. Versluis, A. Prosperetti, and D. Lohse, “Entrapped air bubbles in piezo-driven inkjet printing: their effect on the droplet velocity”, Physics of Fluids **18**, 121511 (2006).

[27] R. Jeurissen, J. de Jong, H. Reinten, M. van den Berg, H. Wijshoff, M. Versluis, and D. Lohse, “Effect of an entrained air bubble on the acoustics of an ink channel”, Journal of the Acoustical Society of America **123**, 2496–2505 (2008).

[28] R. Jeurissen, A. van der Bos, H. Reinten, M. van den Berg, H. Wijshoff, J. de Jong, M. Versluis, and D. Lohse, “Acoustic measurement of bubble size in an inkjet printhead”, Journal of the Acoustical Society of America **126**, 2184–2190 (2009).

[29] S. Lee, D. Kwon, and Y. Choi, “Dynamics of entrained air bubbles inside a piezodriven inkjet printhead”, Applied Physics Letters **95**, 221902 (2009).

[30] R. Jeurissen, H. Wijshoff, M. van den Berg, H. Reinten, and D. Lohse, “Regimes of bubble volume oscillations in a pipe”, Journal of the Acoustical Society of America **130**, 3220–3232 (2011).

[31] L. Crum, “Rectified diffusion”, Ultrasonics **22**, 215–223 (1984).

[32] T. Leighton, *The Acoustic Bubble* (Academic Press) (1994).

[33] C. Brennen, *Cavitation and Bubble Dynamics* (Oxford University Press, New York) (1995).

[34] M. Brenner, S. Hilgenfeldt, and D. Lohse, “Single-bubble sonoluminescence”, Reviews of Modern Physics **74**, 425–484 (2002).

[35] Rayleigh, “Investigation of the character of the equilibrium of an incompressible heavy fluid of variable density”, Proceedings of the London Mathematical Society **14**, 170–177 (1883).

[36] G. Taylor, “The instability of liquid surfaces when accelerated in a direction perpendicular to their planes. i”, Proceedings of the Royal Society of London A **201**, 192–196 (1950).

[37] M. Faraday, “On a peculiar class of acoustical figures; and on certain forms assumed by groups of particles upon vibrating elastic surfaces”, Philosophical Transactions of the Royal Society of London **121**, 299–340 (1831).

[38] J. Castrejón-Pita, G. Martin, and I. Hutchings, “Experimental study of the influence of nozzle defects on drop-on-demand ink jets”, Journal of Imaging Science and Technology **55**, 40305 (2011).

[39] T. Segers and M. Versluis, “Acoustic bubble sorting for ultrasound contrast agent enrichment”, Lab on a Chip **14**, 1705–1714 (2014).

[40] M. Overvelde, H. Vos, N. de Jong, and M. Versluis, chapter Ultrasound Contrast Agent Micro Bubble Dynamics (Springer-Verlag Italia) (2010).

[41] D. Blair and E. Dufresne, “The Matlab particle tracking code repository”, `http://site.physics.georgetown.edu/matlab/`.

[42] P. Marmottant and S. Hilgenfeldt, “A bubble-driven microfluidic transport element for bioengineering”, Proceedings of the National Academy of Sciences of the United States of America **101**, 9523–9527 (2004).

[43] G. Lajoinie, Y. Luan, E. Gelderblom, B. Dollet, F. Mastik, H. Dewitte, I. Lentacker, N. de Jong, and M. Versluis, “Non-spherical oscillations drive the ultrasound-mediated release from targeted microbubbles”, Communications Physics **1** (2018).

[44] R. Bolanos-Jimenéz, M. Rossi, D. F. Rivas, C. J. Kähler, and A. Marin, “Streaming flow by oscillating bubbles: quantitative diagnostics via particle tracking velocimetry”, Journal of Fluid Mechanics **820**, 529–548 (2017).

[45] M. Blander and J. Katz, “Bubble nucleation in liquids”, AIChE Journal **21**, 833–848 (1975).

[46] K. Tanaka, H. Tanaka, R. Angélil, and J. Diemand, “Simple improvement to classical bubble nucleation models”, Physical Review E **92**, 022401 (2015).

[47] H. Herrmann, J. A. Jr., A. Araújo, and M. Almeida, “Particles in fluids”, European Physical Journal Special Topics **143**, 181–189 (2007).

[48] B. Munson, D. Young, T. Okiishi, and W. Huebsch (Wiley) (2009).

[49] A. Mach, J. Kim, A. Arshi, S. Hur, and D. D. Carlo, “Automated cellular sample preparation using a centrifuge-on-a-chip”, Lab on a Chip **11**, 2827–2834 (2011).

[50] T. Karino and H. Goldsmith, “Flow behaviour of blood cells and rigid spheres in an annular vortex”, Philosophical Transactions of the Royal Society of London B: Biological Sciences **279**, 413–445 (1977).

[51] J. Zhang, S. Yan, D. Yuan, G. Alici, N.-T. Nguyen, M. Warkiani, and W. Li, “Fundamentals and applications of inertial microfluidics: a review”, Lab on a Chip **16**, 10–34 (2016).

[52] J. Rensen, D. Bosman, J. Magnaudet, C.-D. Ohl, A. Prosperetti, R. Tögel, M. Versluis, and D. Lohse, “Spiraling bubbles: how acoustic and hydrodynamic forces compete”, Physical Review Letters **86**, 4819–4822 (2001).

[53] D. Lohse, “Bubble puzzles: from fundamentals to applications”, Physical Review Fluids **3**, 110504 (2018).

[54] L. Crum, “Bjerknes forces on bubbles in a stationary sound field”, Journal of the Acoustical Society of America **57**, 1363–1370 (1975).

5

Secondary tail formation and breakup in piezo-acoustic inkjet printing: femtoliter droplets captured in flight *

Piezo-acoustic inkjet printing is the method of choice for the precise, reproducible, and fast delivery of micron-sized droplets for drop-on-demand high-end printing applications, but even further control of the process is desirable, including the breakup of the (secondary) tail. In this chapter the role of the meniscus motion and ink viscosity on secondary tail formation and its breakup in the picoliter droplet formation process of a MEMS piezo-acoustic inkjet printhead were studied experimentally using single-flash stroboscopic imaging at a temporal resolution of 100 ns through 8 ns laser-induced fluorescence illumination. First a trapezoidal pulse and a multi-component pulse were compared to investigate the influence of the meniscus motion on the secondary tail and its satellites. The multi-component pulse produces an approximately four times larger meniscus retraction velocity during the lifetime of the secondary tail than the trapezoidal pulse, resulting in increased stretching and stabilization of the secondary tail. The maximum secondary tail length for the multi-component pulse was found to be 2.2 times larger than for the trapezoidal pulse, leading to a 3.0 times larger number of satellites. By increasing the length of the multi-component pulse, the retracting meniscus motion can be postponed and damped

---

*Submitted as: Arjan Fraters, Tim Segers, Roger Jeurissen, Marc van den Berg, Hans Reinten, Herman Wijshoff, Detlef Lohse, and Michel Versluis, ”Secondary tail formation and breakup in piezo-acoustic inkjet printing: femtoliter droplets captured in flight”.

out which was shown to decrease the secondary tail length and thereby the total volume of secondary satellites. A further reduction in secondary satellite volume was achieved through a reduction of the ink viscosity, which decreased the mean satellite volume. Finally, here, a cascade of the secondary tail into a tertiary tail was observed for the first time in inkjet printing. The cascade results in a bimodal satellite size distribution, where the satellites with a volume ≥ 4 *fL are located closer to the primary tail droplet, while satellites with a volume* < 4 *fL and are located closer to the nozzle.*

5.1 Introduction

Drop-on-demand (DoD) inkjet printing facilitates highly controlled non-contact material deposition at picoliter volumes [1, 2]. Drop formation can be driven by a piezo electric actuator allowing for the deposition of fluids and suspensions with a broad range of surface tensions and viscosities. This enabled inkjet technology to be used not only for classic document printing on paper but also for electronics, e.g. for display fabrication [3, 4] and solar panel printing [5, 6], for life science [7–11], and for 3D printing [12]. An extension of the application range demands higher printing precision and higher deposition rates. Thus, droplet speed, DoD frequency and nozzle integration density must increase, while the droplet size must decrease. To this end, printheads have been developed in silicon, using the Micro-electro-mechanical-system (MEMS) technology [13–15].

The geometry of a typical ink channel in a MEMS-based printhead developed at Océ Technologies B.V. is shown in Fig. 5.1(a). The Helmholtz resonance frequency [16] related to the optimum driving waveform of an ink channel, typically having a value in the range of 100 - 250 kHz, and in this particular study around 240 kHz, can be excited through actuation of the piezoelectric film deposited on a thin flexible membrane. A basic piezo driving waveform that can be used to produce an inkjet is the monopolar trapezoidal pulse shown in Fig. 5.1(b). During the rising edge of the pulse (blue lines), the ink is retracted and forms a concave meniscus at the nozzle exit. Moreover, ink is pulled from the ink reservoir during this so-called fill-before-fire action, or pull-phase [1]. The falling edge of the piezo driving pulse (red lines) pushes the ink outward in resonance with the channel acoustics, through the nozzle, to form a jet with a head droplet and a long primary tail, see Fig. 5.1(c) (1-14 µs). After pinch-off, the primary tail drop is pulled towards its larger head drop due to surface tension, see Fig. 5.1(c) (19-30 µs). The length of the primary tail increases with an increase in head drop velocity [1]. The long primary tail generated at high droplet velocity may breakup due to a Rayleigh-Plateau instability, see Fig. 5.1(c) (29-30 µs). In the ideal case, the primary tail and its primary satellites fully merge with the head droplet before the substrate is reached. However, at high jet velocities the velocity of

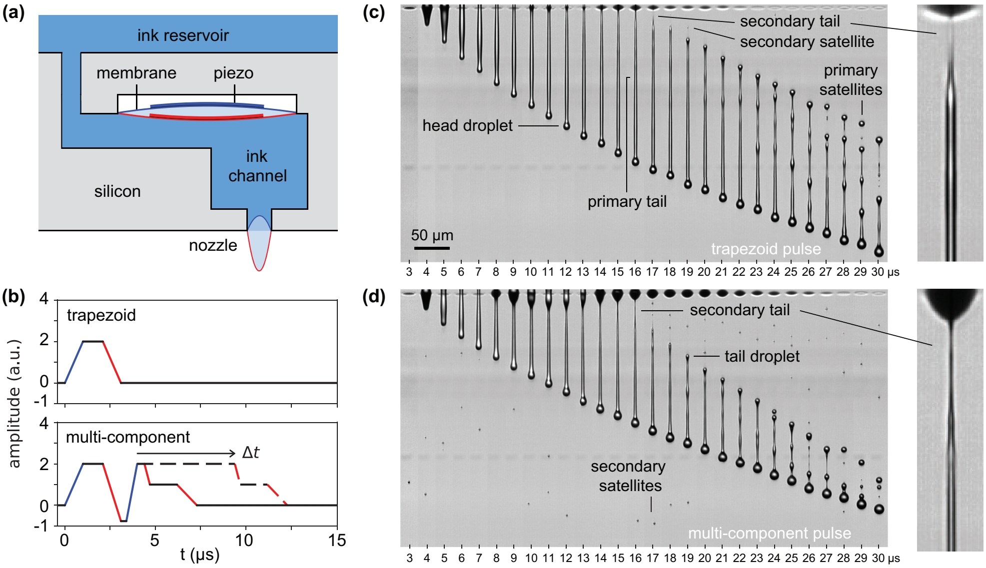

Figure 5.1: (a) Schematic drawing of an ink channel in a MEMS-based piezo-acoustic printhead. (b) Trapezoidal and multi-component piezo driving pulses. (c) Droplet formation driven by the trapezoidal pulse. (d) The length of the primary tail can be decreased through the use of a multi-component pulse. However, the amount of secondary satellites is increased dramatically. The employed imaging technique, iLIF [18], is described in section 5.2.2

the primary satellites is substantially lower than that of the head droplet, leading to differences in the arrival time of the droplets at the substrate. These differences in combination with the movement of the substrate with respect to the printhead result in misaligned deposition, leading to a decreased print quality [1, 17].

A known solution to this problem is the use of a multi-component piezo driving waveform of the type described in [17, 19]. Figure 5.1(b) (lower) presents the multi-component pulse that was used in this study, with the delay time Δt of the pulse's second actuation as control parameter. This type of waveform decreases the length of the primary tail at pinch-off and at the same time increases the velocity of the tail droplet, see Fig. 5.1(d). The additional component of the multi-component pulse shown in Fig. 5.1(b) first strongly retracts the meniscus to thin the primary tail, see the difference between Figs. 5.1(c) and 5.1(d) at 5 µs, and thereby speeds up contraction of the primary tail after pinch-off. Subsequently, it pushes the meniscus far out of the nozzle out of resonance with the channel acoustics and in two steps, to prevent ejection of a droplet, see Fig. 5.1(d) from 8 µs to 12 µs. As a result, the tail droplet is formed at larger distance from the nozzle, thereby shortening the primary tail length. Moreover, the head droplet is slowed down more in the beginning of the drop formation process and less towards pinch-off, which causes the distance from the head droplet to the nozzle exit at pinch-off to be smaller. This difference in head droplet position, which is visible in Figs. 5.1(c) and 5.1(d) at 16 µs, again leads to a shorter primary tail length at pinch-off. Apart from the advantage of a shorter primary tail that contracts faster, the use of this multi-component pulse has the disadvantage of generating substantially larger amounts of micron-sized satellite droplets, so-called secondary satellites; compare Figs. 5.1(c) and 5.1(d). The secondary satellites have little inertia and are therefore easily dragged along by the local airflows induced by the fast moving components in the printer machine. The resulting mist of secondary satellite droplets settles throughout the machine, thereby polluting the inkjet printer.

Secondary satellites result from the breakup of a secondary tail that forms microseconds before pinch-off between the meniscus and the primary tail [1, 20], see Figs. 5.1(c) and 5.1(d). The secondary tail formation starts with the appearance of a neck between the meniscus and the primary tail. The radius of curvature of the neck is small compared to that of the meniscus which results in a large pressure gradient that drives a flow of ink from the neck towards the meniscus [1]. As a result, the neck thins and a secondary tail forms [18, 20, 21] that is stretched, and thus stabilized [22, 23], by the opposing movement of the meniscus and the primary tail drop, to a final radius on the order of 1 µm, see Figs. 5.1(c) and 5.1(d) (15-18 µs).

To date, little is known about the influence of the ink properties and the meniscus motion on the secondary tail formation and breakup and how these can be optimized to minimize the number of secondary satellites in drop-on-demand inkjet printing. Pinch-off studies in continuous inkjet and dripping drop experiments have revealed fluid structures named 'microthread' and 'secondary neck' that appear to be similar to the secondary tail observed in drop-on-demand inkjet printing [24–26]. It has been shown that the final length of these microthreads and secondary necks increases with an increase in liquid viscosity η. The increase in thread length relates to an increase in the viscous length scale $L_\eta = \eta^2/\rho\gamma$ below which viscous damping plays a dominant role, as compared to surface tension-driven pinch-off and Rayleigh-Plateau breakup [25, 27]. Therefore it is expected that the secondary tail length in piezo-driven drop-on-demand inkjet printing also increases with an increase in ink viscosity. Apart from a secondary neck, a cascade of the secondary neck with ever thinner diameters, thus forming new necks, has been observed in the breakup of a drop falling from a faucet [25]. Such a cascade was attributed to noise, e.g. vibrations and thermal noise on the neck of which the profile can be described by the similarity solution of Eggers [28]. The order at which the formation of necks stops due to breakup is expected to depend on the noise amplitude. Whether tertiary and higher order necks are present in the final stage of the breakup of an inkjet is not known. This may be partly due to the challenge involved in the visualization of sub-micron threads that are stretched at rates of the order of 10 m/s. On the other hand, the existence of higher order necks in drop-on-demand inkjet printing is non-trivial since inkjet printing is a highly dynamic process with a liquid meniscus that is actively driven as compared to the static dripping drop experiment. Moreover, the inkjet nozzle diameter is typically one order of magnitude smaller than nozzles employed in the present literature studies on microthread and neck formation.

Here, the challenge of imaging the dynamics of a microscopic secondary tail at nanoseconds temporal resolution is solved by employing single-flash stroboscopic laser-induced fluorescence imaging [18] (iLIF). iLIF was introduced allowing high-intensity incoherent ultrashort light flash exposure times below 10 ns. First, secondary tail formation driven by the trapezoidal pulse and by the multi-component pulse are compared. Second, the delay time Δt of the second component of the multi-component pulse is varied to study its effect on the number of secondary satellites. Finally, secondary tail formation is studied for two different ink viscosities to verify the hypothesized decrease in secondary tail length with a decrease in ink viscosity.

5.2 Experimental methods

5.2.1 Printhead and ink

The printhead used in this study has cylindrical nozzles with a diameter of 14 µm and a length of 10 µm, see Fig. 5.1(a). Droplets with an approximate volume of 1 picoliter (6.2 µm radius) were produced at a velocity of 6.8 m/s measured at an axial distance of 500 µm from the nozzle. Iso Bornyl Acrylate (IBOA, Sigma Aldrich) was used as a model ink as it is a single-component liquid with a viscosity and surface tension similar to those of more complex inks that are used in commercial inkjet printing, i.e. 7 mPa·s and 35 mN/m at 25°C. The viscosity and surface tension of IBOA were measured using a parallel plate rheometer (Anton Paar, MCR 302) and a bubble pressure tensiometer (Sita T60), respectively. Resistive heating elements and temperature sensors were incorporated throughout the printhead to accurately control and monitor the ink temperature. The default operating temperature and corresponding ink viscosity and surface tension were 20.9 ± 0.2°C, 8.02 ± 0.06 mPa·s, and 35.7 ± 0.1 mN/m, respectively.

5.2.2 Imaging setup

The single-flash stroboscopic imaging setup, described in detail by van der Bos *et al.* [21], consisted of a microscope connected to a 20× magnifying objective (Edmund Optics, 59878, M-Plan-APO, NA 0.42) and to a 1× magnification tube lens (InfiniTube$^{\text{TM}}$). A PIV camera (PCO Sensicam QE) was used to capture images and it was controlled from a personal computer. The resulting optical resolution was 362 nm/pixel. To prevent motion blur, illumination was provided by a Laser-Induced

Fluorescence (iLIF) system [18] consisting of a 7 ns pulsed laser (Litron Nano-S, dual cavity Nd:YAG, λ = 532 nm, 65 mJ) that illuminated a fluorescent plate in a highly efficient diffuser (Lavision, part nr. 1108417 and 1003144), resulting in an incoherent 8 ns illumination pulse with a mean wavelength of 577 nm. A lens with a numerical aperture equal to that of the microscope objective condensed the light pulse onto the imaging plane of the microscope. The timing of the illumination flash with respect to the start of the piezo-driving waveform was varied with nanosecond precision through the use of a programmable pulse-delay generator (Berkeley Nucleonics Corp., BNC 575).

5.2.3 Experimental procedure

For each experimental setting, two image sequences were captured. First, the formation of the secondary tail, and the corresponding meniscus motion, were stroboscopically imaged at a temporal resolution of 100 ns over the duration of 30 µs, starting from the beginning of the piezo actuation pulse. Secondly, the size distribution of the secondary satellites was imaged by capturing images at a constant delay of 23 µs with respect to the start of the actuation pulse. In all experiments, the secondary tail had broken up within these 23 µs, and in almost every image the primary tail was still intact. Since the breakup of the secondary tail is random and highly sensitive to noise, 1000 images of 1000 different drop formations were captured for each experimental setting. The printhead was operated at a continuous jetting frequency of 10 kHz where every 6000^{th} droplet formation was imaged to allow sufficient data transfer-time to the personal computer.

In the first experiment, the secondary tail formation and secondary satellite size distribution for the trapezoidal pulse and the multi-component pulse were compared, foremost to study the effect of the meniscus motion amplitude on secondary tail formation. Both piezo driving waveforms are plotted in Fig. 5.1(b). In this experiment, the multi-component pulse with $\Delta t = 0.4$ µs was used.

In the second experiment, Δt of the multi-component pulse was varied over a range from 0.4 µs to 9.4 µs in steps of 1 µs, primarily to determine the influence of the timing of the meniscus retraction on secondary tail formation. To extend the Δt range, a second measurement series was performed for a Δt range from 0.4 µs to 14.4 µs in steps of 1 µs. However, only 100 images of the secondary satellite droplets were captured for each Δt setting, instead of 1000 in the first case.

In the third experiment, the role of ink viscosity on secondary tail formation and secondary satellite size was measured. To this end, the ink temperature was increased from 20.9 ± 0.2°C to 32.0 ± 0.4°C. The ink viscosity thereby decreased from 8.02 ± 0.06 mPa·s to 5.58 ± 0.07 mPa·s. At both viscosities, droplets were generated using the multi-component pulse with Δt = 0.4 µs. The ink temperature had significantly less influence on surface tension; it was measured to be 35.7 ± 0.1 mN/m

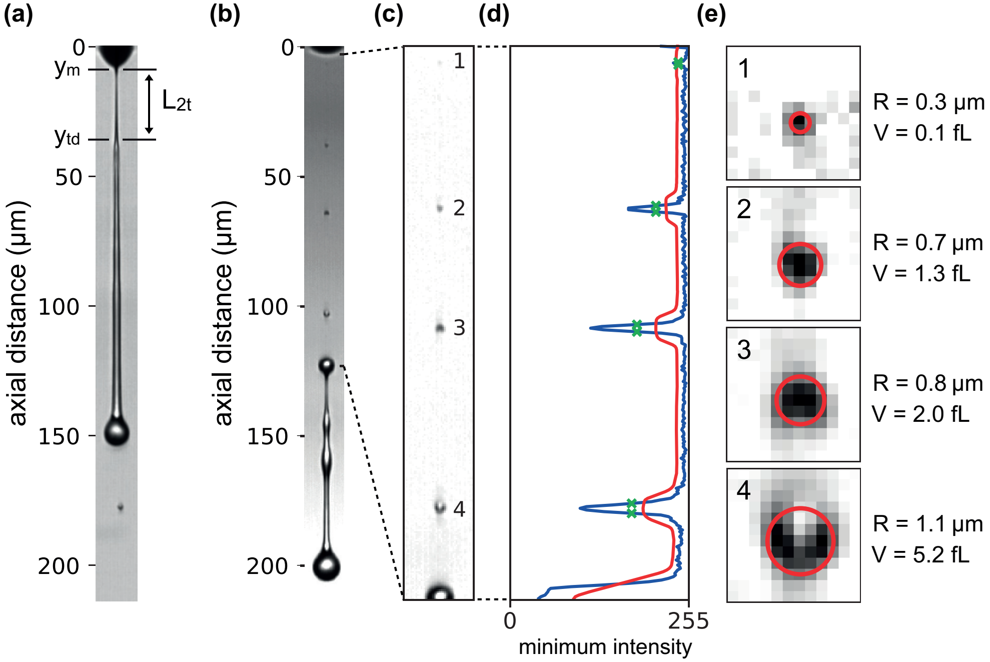

Figure 5.2: (a) The secondary tail length L_{2t} was measured from the inflection point in axial direction at the transition from tail drop to secondary tail y_{td} minus the meniscus position y_m. (b) From the droplet formation images, the secondary satellite position and size distribution were obtained. (c) First, the background intensity was equalized in axial direction, and the images were cropped. (d) Second, the minimum intensity profile was obtained and used to measure the secondary satellite sizes. (e) Examples of obtained droplet sizes (red circles).

and 32.8 ± 0.1 mN/m, at 20.9°C and 32.0°C, respectively.

5.2.4 Image analysis

The length of the secondary tail L_{2t} was measured as a function of time from the image sequences captured of the full drop formation processes at the different driving waveforms, i.e. the trapezoidal pulse and the multi-component pulse with different delay times Δt, and at the different viscosities. The maximum outward meniscus position y_m and the location of the end of the tail drop y_{td} were measured from the images, see Fig. 5.2(a). y_{td} was defined as the inflection point in axial direction at the transition from tail drop to secondary tail. The secondary tail diameter was on the order of the diffraction limit of the imaging system and could therefore not be quantitatively measured.

The secondary satellite size distribution was detected from the image sequences captured at a constant delay of 23 µs with respect to the start of the actuation pulse using an image processing algorithm programmed in the Python programming language (Python Software Foundation, https://www.python.org/). The main steps of the image processing algorithm are summarized in Figs. 5.2(b) to 5.2(e). First, in each raw image (Fig. 5.2(b)), the background intensity was equalized in axial direction. To this end, for each pixel-row the median pixel-intensity of the background was calculated, and for each image the maximum of these median values was determined. Then, the intensity of each pixel was multiplied by the image's maximum row-median-background-intensity divided by the local row-median-background-intensity. Subsequently, the images in each sequence were cropped according to a region of interest (ROI) that was chosen such that in each image the secondary satellites were located within the ROI. This is illustrated in Fig. 5.2(c). Then, for each pixel-row within a cropped image, the minimum intensity value was found to determine the minimum intensity profile, see the blue solid line in Fig. 5.2(d). The satellites were detected in this minimum intensity profile using a threshold based on the minimum intensity profile. The minimum intensity profile was smoothed using the `scipy savgol` filter of first order with a window length of 0.05 times the total profile length. The satellite detection threshold was set as the difference of the smoothed profile intensity values and the median of the profile intensity values, multiplied by 0.8 to prevent false negatives, and lowered by 10 on a scale of 0-255 to prevent false positives due to background noise, see solid red line in Fig. 5.2(d). The size of the detected satellites was measured from the width of the minimum intensity profile at half the distance between the minimum peak-intensity and the median of the minimum intensity profile, see green crosses in Fig. 5.2(d). Around the center location of the detected satellite droplets, the edge detection method was applied once more in the lateral direction. The satellite droplet size was then set to the minimum obtained in both directions, see red circles in Fig. 5.2(e). In the few images that the rear end of the primary tail was already broken up, and a primary satellite appeared within the ROI, the primary satellite was removed from the results based on its volume. For the employed printhead there is a clear division between primary and secondary satellites at a volume of 45 fL in the satellite size distribution, i.e. primary satellites were filtered out by excluding satellites with a volume $\geq$ 45 fL.

Figure 5.2(e) demonstrates the imaging challenge involved in the Mie scattering-dominated [29] imaging regime of micron-sized femtoliter droplets. The scattered light intensity is highly dependent on both the size of the satellite droplets and their position within the depth of field. Moreover, the minimum intensity profile depends on the background illumination intensity, and so does the detected droplet radius. Satellite droplet sizes measured using the minimum intensity profile method can therefore only be used to compare relative numbers. On top of that, all experiments on the same parameter study should be performed in a single measurement series, using the exact same focusing and illumination conditions.

A second sizing method that allows for background intensity-independent sizing of the droplets, based on the inflection point of the angle-averaged intensity profile of a detected satellite droplet [21], was also employed to analyze the captured images. However, its sizing results were found to be inferior to the minimum intensity profile method described above due to the non-axisymmetric pixel intensity of some of the detected droplets (Fig. 5.2(e-4)). Therefore, only the results obtained using the minimum intensity profile method are presented here.

5.3 Results

5.3.1 Trapezoidal pulse versus multi-component pulse

Figure 5.3(a) shows the image sequence of the secondary tail formation and breakup for the trapezoidal pulse with an interframe time of 1 µs. Figure 5.3(b) presents the same image sequence for the multi-component pulse with Δt = 0.4 µs.

Figure 5.3(c) displays the maximum outward meniscus position y_m (square markers) and the tail drop position y_{td} (triangular markers) as a function of time. The dashed vertical lines mark the appearance of the secondary tail, i.e. the moment at which the neck has thinned down sufficiently for its length to become measurable, while the solid vertical lines indicate the occurrence of secondary tail break up. The meniscus position plot of the multi-component pulse has a 5.1 times larger maximum value than that of the trapezoidal pulse, resulting in approximately 3 times higher meniscus velocity, see Fig. 5.3(d). Moreover, for the multi-component pulse the meniscus velocity during the lifetime of the secondary tail is approx. 4 times as large when it is negative, i.e. retracting. For the trapezoidal pulse, the tail drop formation starts at a later time, and closer to the nozzle than the one of the multi-component pulse, see Fig. 5.3(c). This can also be observed from Fig. 5.3(e) where the secondary tail length L_{2t} is plotted as a function of time. At the moment of secondary tail-breakup (solid vertical lines), L_{2t} is 2.2 times longer for the multi-component pulse than the one for the trapezoidal pulse. Furthermore, note that the lifetime of the secondary tail formed using the multi-component pulse is approx. 40% longer than the one formed using the trapezoidal pulse.

For both driving pulses, the size distribution of the secondary satellites is shown in Fig. 5.3(f). Droplet formation driven by the multi-component pulse results in a larger total number of secondary satellites (N_{tot} = 1648) as compared to the one driven by the trapezoidal pulse (N_{tot} = 550). Note that the volume distributions are bimodal with a minimum in droplet number near a volume of 4 fL. Also note that in particular the number of larger secondary satellites, with a volume $\geq$ 4 fL, is increased when the multi-component pulse is used instead of the trapezoidal pulse.

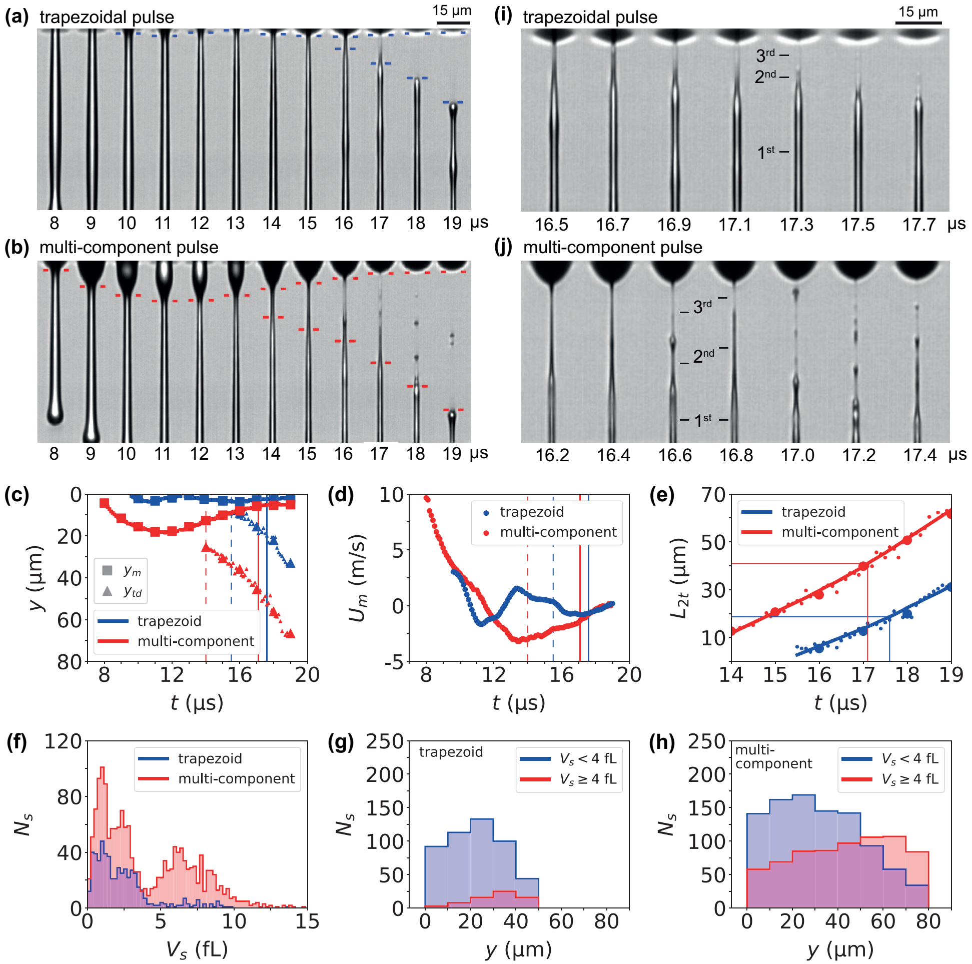

Figure 5.3: Secondary tail formation and breakup for (a) the trapezoidal pulse and (b) the multi-component pulse with Δt= 0.4 μs. The temporal resolution is 1 μs. (c) Meniscus position y_m and tail drop position y_{td} as function of time. The large markers in (c) and (e) correspond to the images in (a) and (b). The dashed and solid vertical lines indicate the secondary tail appearance and breakup, respectively. (d) Meniscus velocity over time. (e) Secondary tail length as function of time. (f) Secondary satellite volume distributions. Position distribution of the secondary satellites with a volume < 4 fL, and that of secondary satellites with a volume ≥ 4 fL, both generated using (g) the trapezoidal pulse and (h) the multi-component pulse. Image sequence of the secondary tail with a temporal resolution of 0.2 μs for (i) the trapezoidal pulse and (j) the multi-component pulse with Δt = 0.4 μs from Section 5.3.2, see also Fig. 5.5 and Fig. 5.7 for more details.

To investigate the origin of the bimodality of the secondary satellite size distributions obtained for the trapezoidal and for the multi-component pulse, the axial position of the secondary satellites y_s with volumes < 4 fL is plotted together with that of the secondary satellites ≥ 4 fL. Figure 5.3(g) shows the result for the trapezoidal pulse and Fig. 5.3(h) that for the multi-component pulse. The nozzle plate was located at $y = 0$. Note that for both pulses the satellite droplets located closer to the nozzle are smaller than those closer to the tail droplet.

The difference in the locations between the satellites with a volume < 4 fL and that with a volume ≥ 4 fL is further investigated by inspecting the secondary tail in more detail around its breakup, see Figs. 5.3(i) and 5.3(j). The figures show the stroboscopically imaged droplet formation process of 7 different droplets at a temporal resolution of 200 ns, driven by the trapezoidal pulse and by the multi-component pulse, respectively. Note that secondary tail formation is irregular in time. Also note that for the multi-component pulse the secondary tail cascades into a tertiary tail, which in some cases leads to the formation of a thick tail droplet on the secondary tail. Rayleigh breakup of the thinner tertiary tail, which occurs notably earlier than breakup of the secondary tail, will produce smaller satellites as compared to those of the secondary tail. Thus, the bimodality and the position-dependence of the droplet size distribution for the multi-component pulse in Figs. 5.3(f) and 5.3(h) results indeed from the presence of a thinner tail close to the nozzle, i.e. a tertiary tail. Whether or not for the trapezoidal pulse also a tertiary tail forms, is much less evident from the images in Fig. 5.3(i). However, the bimodality and position-dependence of the droplet size distribution for the trapezoidal pulse in Figs. 5.3(f) and 5.3(g) show that also for the trapezoidal pulse the secondary tail almost certainly cascades into a tertiary tail. Furthermore, it seems like most satellites originate from the tertiary tail.

To shed more light on the formation of a tertiary tail for the trapezoidal pulse, the secondary tail formation and breakup were imaged with a high-speed camera (Shimadzu HPV-X2) at 5 Mfps. This was done for a printhead with a 30 μm diameter nozzle and ink with a viscosity and surface tension of 10 mPa·s and 28 mN·m, respectively. More experimental details are given in the Appendix. The results of this experiment are summarized in Fig. 5.7, which has image sequences of 8 different droplet formations. Figure 5.7 clearly demonstrates the formation of a tertiary tail next to the secondary tail for the trapezoidal pulse. In addition, Fig. 5.7 also reveals the formation of a quaternary tail next to the tertiary tail. The formation of a quaternary tail, and subsequently quaternary satellites, may explain the bimodal distribution in Fig. 5.3(f) for the satellites with a volume < 4 fL, which has a minimum at approx. 1.5 fL. The image sequences in Fig. 5.7 also show that in most of the 8 recordings the satellites originate only from the tertiary and quaternary tail because the secondary tail contracts and merges with the primary tail droplet before it can break up. This may explain the relative low number of satellites with a volume ≥ 4 fL in Fig. 5.3(f)

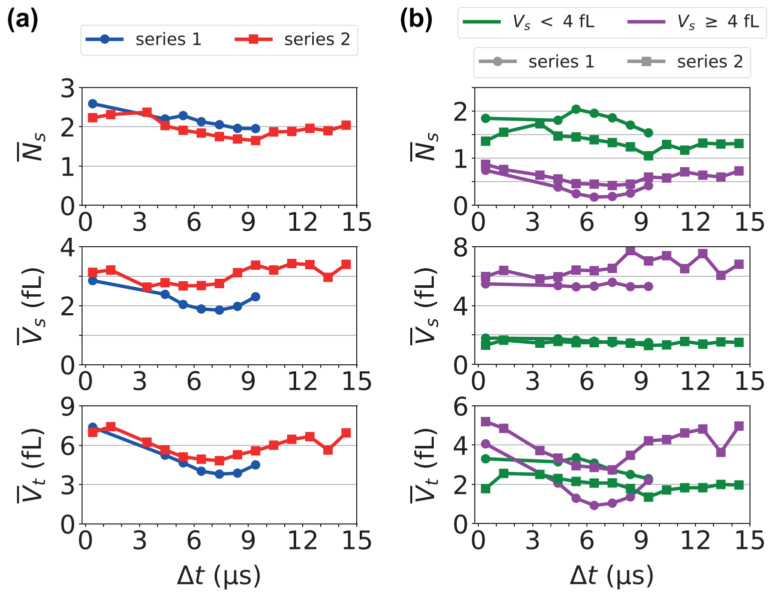

Figure 5.4: (a) Mean number of secondary satellites $\overline{N}_s$, mean secondary satellite volume $\overline{V}_s$, and mean total secondary satellite volume $\overline{V}_t$ as function of the delay time Δt of the multi-component pulse. Each data point of series 1 was obtained from 1000 events, while for series 2 this was 100 events. (b) Data from (a) where a distinction is made between secondary satellites with $V_s < 4$ fL and with $V_s \geq 4$ fL.

for the trapezoidal pulse compared to that for the multi-component pulse.

5.3.2 Multi-component pulse length

The delay time Δt of the multi-component pulse was varied from 0.4 µs up to 14.4 µs. The different pulse lengths did not alter the head drop velocity of 6.8 m/s. Per droplet formation, the mean number of secondary satellites $\overline{N}_s$, the mean secondary satellite volume $\overline{V}_s$, and the mean total secondary satellite volume $\overline{V}_t$ are plotted in Fig. 5.4(a). The data for measurement series 1, obtained from 1000 droplet formations per data point, is represented by the blue dots and the data for measurement series 2, obtained from 100 droplet formations per data point, is represented by the red squares. The absolute numbers of measurement series 1 and 2 are slightly different, but, the trend is the same. Data for $\Delta t = 2.4$ µs is not shown since at this Δt a second droplet was ejected after the main droplet.

The mean number of satellites per droplet formation $\overline{N}_s$ is at minimum for the pulse with $\Delta t = 9.4$ µs. However, the mean secondary satellite volume and the mean total secondary satellite volume per droplet formation are at minimum at $\Delta t = 7.4$ µs.

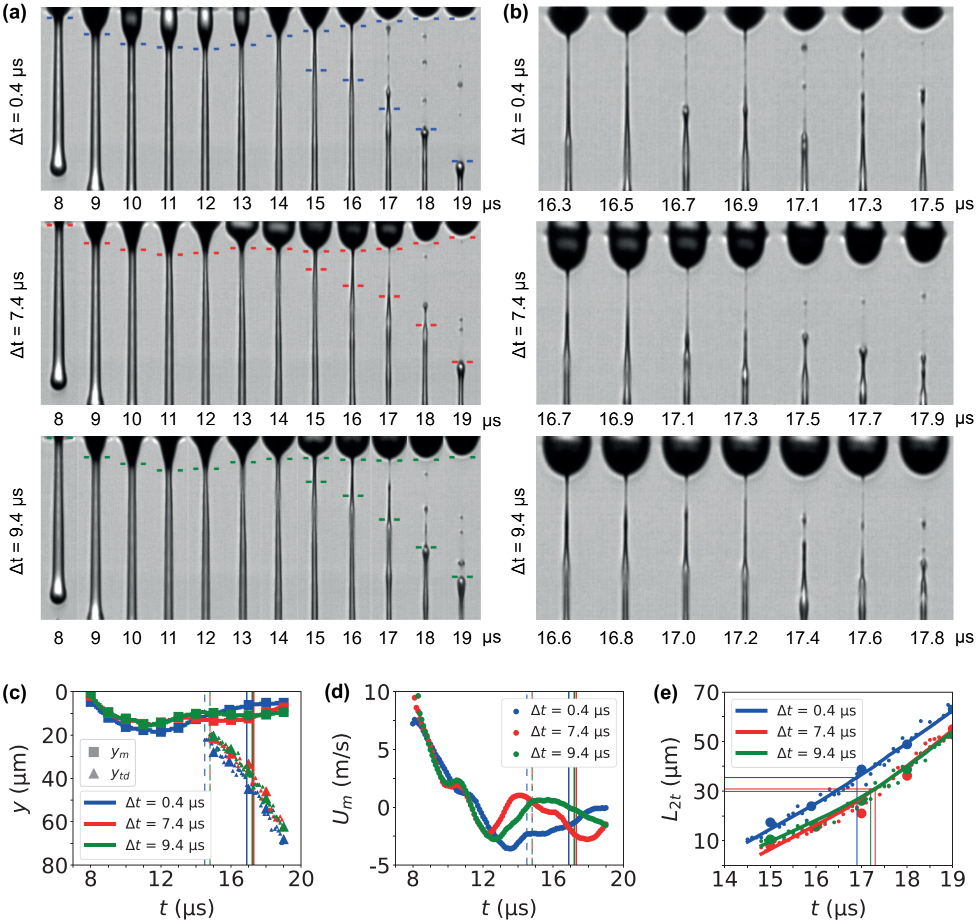

Figure 5.5: Secondary tail formation and breakup for multi-component pulses with delay times Δt of 0.4, 7.4, and 9.4 μs, (a) with a temporal resolution of 1 μs, and (b) with a temporal resolution of 0.2 μs. (c) Meniscus position y_m and tail drop position y_{td} as function of time. The larger markers in (c) and (e) correspond to the images in (a). The dashed and solid vertical lines indicate the secondary tail appearance and breakup, respectively. (d) Meniscus velocity over time. (e) Secondary tail length as function of time.

To investigate the observed difference in the location of the minima in $\overline{N}_s$, $\overline{V}_s$ and $\overline{V}_t$, the data of the measurement series are plotted again in Fig. 5.4(b). Now, a distinction is made between the larger satellites with a volume ≥ 4 fL (green), and the smaller satellites with a volume < 4 fL (magenta). Note that the minimum in $\overline{V}_t$ in Fig. 5.4(a) corresponds to the minimum in $\overline{N}_s$ of the larger satellites in Fig. 5.4(b), which dominate despite their smaller number because of their larger size, while the minimum in $\overline{N}_s$ in Fig. 5.4(a) corresponds to the minimum in $\overline{N}_s$ of the smaller satellites in Fig. 5.4(b), which dominate due to their larger number. This explains the difference between the location of the minima in $\overline{N}_s$ and $\overline{V}_t$ in Fig. 5.4(a).

For the multi-component pulses with Δt = 0.4, 7.4, and 9.4 μs, secondary tail formation and breakup are shown in Fig. 5.5(a) and 5.5(b). The meniscus position is plotted in Fig. 5.5(c). The maximum outward meniscus position for the pulses with Δt = 7.4 and 9.4 μs is 0.82 times smaller than that for the pulse with Δt = 0.4 μs. Furthermore, in contrary to the pulse with Δt = 0.4 μs, the meniscus positions of the pulses with Δt = 7.4 μs and Δt = 9.4 μs have a second local maximum in the meniscus position. The second local maximum in the meniscus positions results in a meniscus velocity that is positive during the start of the formation of the secondary tail, and, only slightly negative at the end of its existence, see Fig. 5.5(d). In contrary, for the pulse with Δt = 0.4 μs, the meniscus velocity is negative, or retracting, over the full lifetime of the secondary tail. The retracting meniscus stabilizes the secondary tail against Rayleigh-Plateau breakup by stretching it [22, 23] and therefore it is most likely causing the 20% longer secondary tail generated using the pulse with Δt = 0.4 μs as compared to those generated using the pulses with Δt = 7.4 and 9.4 μs, see Fig. 5.5(e).

5.3.3 Varying the ink viscosity

Figure 5.6(a) and 5.6(b) show image sequences of secondary tail formation and breakup for two different ink viscosities driven by the multi-component pulse with Δt = 0.4 μs. For an ink viscosity of 5.6 mPa·s, the maximum outward meniscus position is 1.25 times larger than that for an ink viscosity of 8.0 mPa·s, see Fig. 5.6(c). The meniscus velocity is very similar for both ink viscosities, see Fig. 5.6(d). The secondary tail length L_{2t} is plotted in Fig. 5.6(e) as a function of time. The breakup time of the secondary tail generated using the ink with the lower viscosity occurs 1.7 μs earlier in time. As a result, the maximum secondary tail length is 34% shorter for the low viscosity ink as compared to the one of the higher viscosity ink.

The secondary satellite volume distributions are plotted in Fig. 5.6(f). Both distributions are bimodal, and note that the change in viscosity did not affect the volume at which the distribution is minimum: it is near a volume of 4 fL, as before. Lowering the ink viscosity is observed to lower both the number and the size of the satellites > 4 fL. Nevertheless, an increase in the number of smaller satellites is observed with a decrease in ink viscosity. All in all, no large difference is observed in

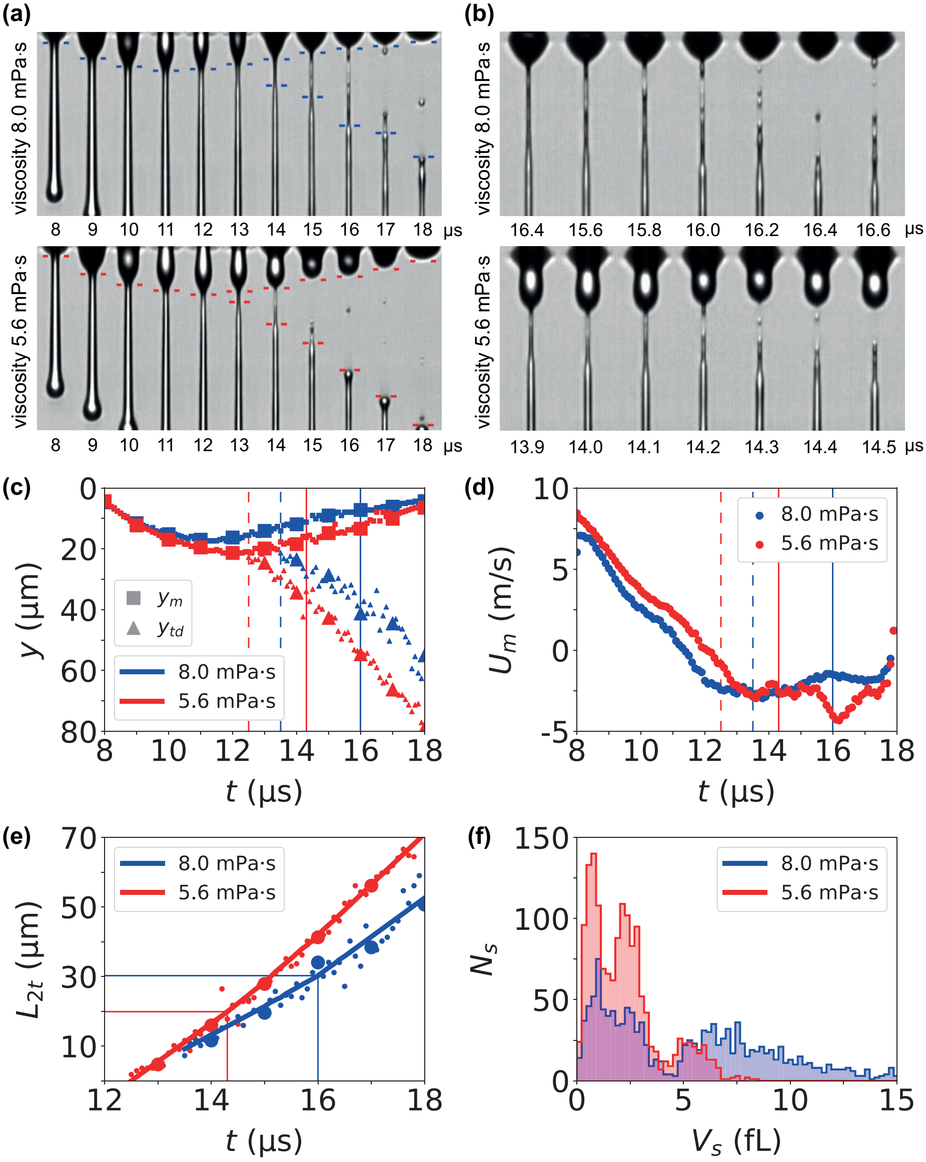

Figure 5.6: Secondary tail formation and breakup driven by the multi-component pulse with $\Delta t = 0.4$ μs at an ink viscosity of 8.0 mPa·s and 5.6 mPa·s, (a) with a temporal resolution of 1 μs, and (b) with temporal resolutions of 0.2 μs and 0.1 μs. (c) Meniscus position y_m and tail drop position y_{td} as function of time. The larger markers in (c) and (e) correspond to the images in (a). The dashed and solid vertical lines indicate the secondary tail appearance and breakup, respectively. (d) Meniscus velocity. (e) Secondary tail length as function of time. (f) Secondary satellite volume distributions.

the total number of secondary satellites per droplet formation for the two different ink viscosities studied here; they were 1388 and 1530 for an ink viscosity of 8.0 mPa·s and 5.6 mPa·s, respectively. However, more importantly, the mean secondary satellite size and the total secondary satellite volume both decrease with a decrease in ink viscosity.

5.4 Discussion

First, we discuss the remarkable stability of the sub-micron diameter secondary tail that can reach an aspect ratio as large as 40. Three stabilizing mechanisms are proposed here. Firstly, during secondary tail formation, a tail droplet with radius R_{td} forms on the primary tail. The Laplace pressure in the tail droplet is $2\gamma/R_{td}$ whereas that in the cylindrical secondary tail is γ/R_{2t}. Thus, when $2R_{2t} > R_{td}$ the secondary tail is fed by a flow of liquid from the tail droplet. Secondly, since the secondary tail diameter is typically smaller than the viscous length scale (L_η = 1.8 μm and 0.9 μm for the two ink viscosities used in this work) thinning of the secondary tail through the drainage of ink is inhibited. The third stabilizing mechanism results from the retraction of the meniscus towards the nozzle and the contraction of the primary tail droplet towards the head droplet. Their opposing movement stretches the secondary tail and thereby also the wavelengths of the instabilities on its profile. The faster the meniscus retracts and the primary tail droplet contracts, the shorter the existence of the instabilities and consequently, the more stable the tail is. To determine the relative importance of each mechanism in time, numerical simulations and accurate measurements, both in time and space, of the radial profile of the tail are required.

The observations presented in this work can be explained using the proposed stabilizing mechanisms. Regarding the driving waveform, the larger secondary tail length observed for the drop formation driven by the multi-component pulse, as compared to the one driven by the trapezoidal pulse, can be explained from the 4 times higher negative meniscus velocity (retracting meniscus) observed for the multi-component pulse which results in a increased stabilization of the secondary tail through stretching. Regarding the ink viscosity, the measured mean secondary satellite size decreased for an ink viscosity decrease. The decrease may result from a decrease of the viscous length scale. If the secondary tail thickness scales with the viscous length scale, this would result in smaller secondary satellites from the secondary tail of an inkjet generated with a lower viscosity. The shorter lifetime and lower stability of the secondary tail formed with the lower ink viscosity results from the decrease in viscous damping of the Rayleigh-Plateau instability.

The multi-component pulses with Δt = 7.4 µs and Δt = 9.4 µs resulted in the same secondary tail length at breakup. However, the total number of satellites was larger for the pulse with Δt = 7.4 µs and the total satellite volume was larger for the pulse with Δt = 9.4 µs. The differences are most likely caused by differences in the radial profile of the tail due to differences in meniscus motion and shape, which result in a different average length ratio between the secondary and tertiary tail. However, these could not be resolved due to the diffraction-limited imaging resolution and due to the irregularity in time of the secondary and tertiary tail formation process.

Future work may focus on the numerical modeling of the secondary tail formation process, potentially allowing for a more quantitative understanding of the physical mechanisms that result in secondary- and tertiary tail formation in drop-on-demand inkjet printing. It would be of interest to address, e.g., the cascade in terms of the ratio of the tail thicknesses between successive cascades.

5.5 Conclusions

In this experimental study on droplet formation in drop-on-demand inkjet printing we studied the formation of a secondary tail with a diameter on the order of 1 µm between the primary tail and the meniscus, in the last microseconds before pinch-off. The influence of the driving waveform and viscosity on secondary tail formation was investigated. We thereby observed, for the first time, the existence of tertiary and quaternary tails in drop-on-demand inkjet printing. The secondary-, tertiary-, and quaternary tails break up and form femtoliter satellite droplets. The size distribution of the sub-micron diameter satellites can be measured in-flight using 8 ns laser-induced fluorescence light pulses. The multi-component pulse results in a meniscus motion with 4 times higher retracting velocity during the lifetime of the secondary tail. The higher stretching rate stabilizes the secondary tail to a maximum length that was 2.2 times larger than the one formed using a trapezoidal pulse. By increasing the length of the multi-component pulse, the retracting meniscus motion can be damped out which was shown to decrease the secondary tail length and thereby the total volume of secondary satellites. A further reduction in secondary satellite volume was achieved through a reduction of the ink viscosity. These new pieces of insight may help in the design of piezo driving waveforms and inks for minimized machine pollution due to secondary satellite droplets.

5.A High-speed recordings of tertiary tail formation and breakup

The formation of a secondary and tertiary tail in piezo-acoustic inkjet printing for the trapezoidal pulse was recorded in more detail using a high-speed imaging setup and a different printhead. The ink channel that was used had a Helmholtz resonance frequency of 133 kHz, and had a cylindrical nozzle with a diameter and length of 30 µm. As ink a non-colored version of the CrystalPoint$^{\text{TM}}$ technology [30] was used, which is a hot melt ink that is jetted at 130°C. At this temperature the ink's viscosity, density, and surface tension are 10 mPa·s, 1080 kg/m^3, and 28 mN·m respectively. The trapezoidal pulse had a rise- and fall time of 1.5 µs, and a high time of 2.0 µs. The droplets were jetted at a velocity of 9.0 m/s. The high-speed imaging setup consisted of an Olympus transmitted light microscope with a 50× microscope objective (SLMPLN50x, N.A. 0.35, W.D. 18 mm) and a 2× magnification lens (U-ECA), a Shimadzu HPV-X2 high-speed camera (10 Mfps, 256 frames, 400×250 pixels, 30 µm pixel size) and a xenon flash light source, resulting in a spatial resolution of 300 nm/pixel. The high-speed camera was operated at an exposure time of 110 ns and framerate of 5 Mfps. The printhead, camera, and light source were triggered with nanosecond precision using a programmable pulse-delay generator (Berkeley Nucleonics Corp., BNC 575). In each experiment the 1000th droplet formation was imaged.

The formation and breakup of a tertiary tail was recorded for 8 different droplet formations. These recordings are summarized in the image sequences in Fig. 5.7. Note that these results not only demonstrate the formation of a tertiary tail during droplet formation with a trapezoidal pulse, but also reveal the formation of a quaternary tail. Furthermore, note that in most cases the secondary tail contracts into the primary tail droplet before it can break up, so that only satellites from the tertiary- and quaternary tail are left.

References

[1] H. Wijshoff, "The dynamics of the piezo inkjet printhead operation", Physics Reports **491**, 77–177 (2010).

[2] S. D. Hoath, *Fundamentals of Inkjet Printing: The Science of Inkjet and Droplets* (Wiley-VCH Verlag GmbH & Co. KGaA) (2015).

[3] T. Shimoda, K. Morii, S. Seki, and H. Kiguchi, "Inkjet printing of light-emitting polymer displays", Inkjet Printing of Functional Materials **28**, 821–827 (2003).

[4] C. Jiang, L. Mu, J. Zou, Z. He, Z. Zhong, L. Wang, M. Xu, J. Wang, J. Peng, and Y. Cao, "Full-color quantum dots active matrix display fabricated by ink-jet printing", Science China Chemistry **60**, 1349–1355 (2017).

[5] T. Eggenhuisen, Y. Galagan, E. Coenen, W. Voorthuijzen, M. Slaats, S. Kommeren, S. Shanmuganam, M. Coenen, R. Andriessen, and W. Groen, "Digital fabrication of organic solar cells by inkjet printing using non-halogenated solvents", Solar Energy Materials and Solar Cells **134**, 364–372 (2015).

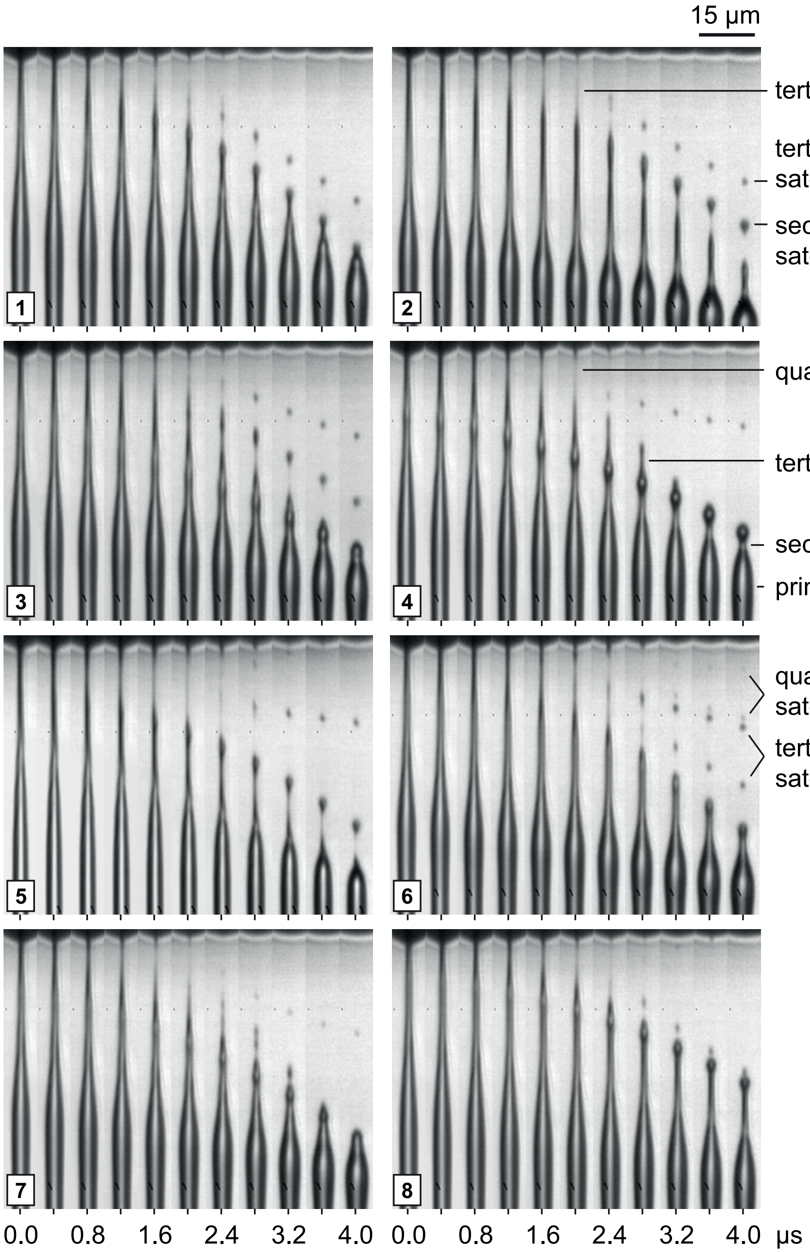

Figure 5.7: High-speed recordings of tertiary- and quaternary tail formation and breakup for 8 different droplet formations with a trapezoidal pulse at a 30 µm diameter nozzle. The time given below the image sequences is with respect to the first frame of each image sequence. The temporal resolution is 0.4 µs.

[6] S. Hashmi, M. Ozkan, J. Halme, K. Misic, S. Zakeeruddin, J. Paltakari, M. Grätzel, and P. Lund, "High performance dye-sensitized solar cells with inkjet printed ionic liquid electrolyte", Nano Energy **17**, 206–215 (2015).

[7] A. Simaite, F. Mesnilgrente, B. Tondu, P. Souères, and C. Bergaud, "Towards inkjet printable conducting polymer artifical muscles", Sensors and Actuators B: Chemical **229**, 425–433 (2016).

[8] R. Daly, T. Harrington, G. Martin, and I. Hutchings, "Inkjet printing for pharmaceutics - a review of research and manufacturing", International Journal of Pharmaceutics **494**, 554–567 (2015).

[9] S. Hewes, A. Wong, and P. Searson, "Bioprinting microvessels using and inkjet printer", Bioprinting **7**, 14–18 (2017).

[10] M. Nakamura, A. Kobayashi, F. Takagi, A. Watanabe, Y. Hiruma, K. Ohuchi, Y. Iwasaki, M. Horie, I. Morita, and S. Takatani, "Biocompatible inkjet printing technique for designed seeding of individual living cells", Tissue Engineering **11**, 1658–1666 (2005).

[11] G. Villar, A. Graham, and H. Bayley, "A tissue-like printed material", Science **340**, 48–52 (2013).

[12] B. Derby, "Additive manufacture of ceramic components by inkjet printing", Engineering **1**, 113–123 (2015).

[13] C. Menzel, A. Bibl, and P. Hoisington, "MEMS solutions for precision microfluidic dispensing application", Technical Report, Fujifilm Dimatix Inc. (2004).

[14] A. van der Bos, T. Segers, R. Jeurissen, M. van den Berg, H. Reinten, H. Wijshoff, M. Versluis, and D. Lohse, "Infrared imaging and acoustic sizing of a bubble inside a micro-electro-mechanical system piezo ink channel", Journal of Applied Physics **110**, 034503 (2011).

[15] B.-H. Kim, H.-S. Lee, S.-W. Kim, P. Kang, and Y.-S. Park, "Hydrodynamic responses of a piezoelectric driven MEMS inkjet print-head", Sensors and Actuators A: Physical **210**, 131–140 (2014).

[16] H. von Helmholtz, *On the sensations of tone as a physiological basis for the theory of music* (London, New York: Longmans, Green, and Co.) (1895).

[17] N. Morita, T. Hamazaki, and T. Ishiyama, "Observation on satellite behavior by double-pulse driving for high-speed inkjet", Journal of Imaging Science and Technology **60**, 40503 (2016).

[18] A. van der Bos, A. Zijlstra, E. Gelderblom, and M. Versluis, “iLIF: illumination by laser-induced fluorescence for single flash imaging on a nanoseconds timescale”, Experiments in Fluids **51**, 1283–1289 (2011).

[19] H. Gan, X. Shan, T. Eriksson, B. Lok, and Y. Lam, “Reduction of droplet volume by controlling actuating waveforms in inkjet printing for micro-pattern formation”, Journal of Micromechanics and Microengineering **19**, 055010 (2009).

[20] H. Wijshoff, “Drop formation mechanisms in piezo-acoustic inkjet”, Proceedings Nanotech 2007 **3**, 448–451 (2007).

[21] A. van der Bos, M.-J. van der Meulen, T. Driessen, M. van den Berg, H. Reinten, H. Wijshoff, M. Versluis, and D. Lohse, “Velocity profile inside piezoacoustic inkjet droplets in flight: comparison between experiment and numerical simulation”, Physical Review Applied **1**, 014004 (2014).

[22] I. Frankel and D. Weihs, “Stability of a capillary jet with linearly increasing axial velocity (with application to shaped charges)”, Journal of Fluid Mechanics **155**, 289–307 (1985).

[23] S. L. Dizès and E. Villermaux, “Capillary jet breakup by noise amplification”, Journal of Fluid Mechanics **810**, 281–306 (2017).

[24] T. Kowaleski, “On the separation of droplets from a liquid jet”, Fluid Dynamics Research **17**, 121–145 (1996).

[25] X. Shi, M. Brenner, and S. Nagel, “A cascade of structure in a drop falling from a faucet”, Science **265**, 219–222 (1994).

[26] M. Brenner, X. Shi, and S. Nagel, “Iterated instabilities during droplet fission”, Physical Review Letters **73**, 3391–3394 (1994).

[27] J. Eggers and E. Villermaux, “Physics of liquid jets”, Reports on Progress in Physics **71**, 036601 (2008).

[28] J. Eggers, “Universal pinching of 3D axisymmetric free-surface flow”, Physical Review Letters **71**, 3458–3460 (1993).

[29] H. van de Hulst, *Light Scattering by Small Particles* (Dover Publications Inc. New York) (1981).

[30] Océ Technologies B.V., For more information on Océ CrystalPoint technology see `https://www.oce.com/products/crystalpoint/`.

6

Conclusions and Outlook

The entrainment of air bubbles and the formation of satellite droplets are undesirable in piezo inkjet printing as they limit the printing reliability, printing quality, and production rate. The underlying processes and physical mechanisms were investigated both by using high-speed visualization setups, tailor-made printheads, and by applying boundary integral simulations.

6.1 Conclusions

In Chapter 2 bubble entrainment was visualized in a commercially available single glass nozzle printhead using 8 ns single-flash stroboscopic imaging with illumination by laser-induced fluorescence (iLIF). The mechanism by which a bubble can pinch off from the acoustically driven meniscus was investigated for various piezo driving conditions. From analysis of the meniscus and the piezo resonance modes it was determined that the meniscus was driven by a slosh mode of the printhead, and a piezo longitudinal resonance mode that was driven by the rising and falling edges of the rectangular piezo driving pulse. The formation and closure of a central air cavity in the meniscus leads to bubble pinch-off, and was observed to be the result of the following meniscus shape deformation process: upon retraction of the meniscus two well-timed accelerations of the concave meniscus in outward direction, away from the ink channel, resulted in the formation of a central outward-moving liquid jet followed by the formation of a toroidal outward-moving liquid jet. Upon the formation of the toroidal jet, the central jet recoiled inward and formed an air cavity, which was then enclosed by the outward-moving toroidal jet. The two physical mechanisms responsible for both jet formation events are the geometrical focusing of the flow at the concave meniscus, and the inhomogeneous pressure gradient along the concave meniscus.

In Chapter 3 a shortwave infrared (SWIR) imaging setup was developed to visualize the channels and nozzles in a silicon MEMS-based printhead. An experimental printhead was modified to facilitate SWIR imaging, and was used to study the dynamics of entrained air bubbles. The translation, growth, and interaction of bubbles shortly after entrainment were visualized at a temporal resolution of 20 ms. The steady-state dynamics of fully grown bubbles was visualized at a temporal resolution of 0.5 µs using stroboscopic imaging. The recordings revealed several new details of the bubble entrainment process, including the presence and interaction of multiple bubbles. The bubbles collected in the corners of the feedthrough at the nozzle plate, where they would either stably coexist or merge into one bubble as a result of Ostwald ripening.

In Chapter 4, for the first time, bubble entrainment was visualized in a silicon-based printhead. For this purpose an experimental printhead was produced containing a silicon-based functional acoustic part and a glass nozzle plate with feedthroughs and nozzles. Furthermore a real-time ink channel acoustics monitoring system was used, with the piezo acting as a sensor to trigger the high-speed imaging at the moment of stochastic bubble entrainment. It was discovered that dirt particles are captured in a vortical flow above the nozzle during the regular ink jetting process. These dirt particles trigger bubble nucleation upon interaction with the oscillating meniscus. After nucleation the bubble moves into the ink channel and separates from the dirt particle. Then, depending on the initial bubble position and the combination of acoustic forces and convective ink flow in the ink channel, the bubble either returns to the nozzle within a few actuation cycles, where it is ejected with droplet formation, or it translates to a corner where it is permanently entrained. An entrained bubble grows by rectified diffusion, can split up into more bubbles, and disturbs the ink channel acoustics and thereby the jet length and velocity.

In Chapter 5 secondary tail formation and breakup were studied by measuring the meniscus position and secondary tail length as a function of time, and by measuring the size distribution of the femtoliter satellite droplets formed at secondary tail breakup. The meniscus motion, controlled through the piezo driving waveform, and the ink viscosity were both found to affect the secondary tail length and the satellite size distribution. By reducing the meniscus retraction velocity during the existence of the secondary tail, the secondary tail length and the total secondary satellite volume can be decreased as the stretching stabilized the tail against Rayleigh-Plateau instabilities. A further decrease in the secondary tail length and in the total secondary satellite volume is feasible through a decrease in ink viscosity as it decreases the delay of the Rayleigh-Plateau breakup by viscous effects. Finally, for the first time also tertiary- and quaternary tails were observed, as well as the corresponding tertiary- and quaternary satellites.

6.2 Outlook

The stability of an acoustically driven meniscus is not only relevant for the problem of bubble entrainment, as discussed in Chapter 2, but also to the problem of jet angle errors. Directional jetting instabilities can be the result of geometrical defects, but might also be the result of Rayleigh-Taylor instability or parametrically driven meniscus instability, as detailed in Chapter 3 of the PhD thesis of Mark-Jan van der Meulen (2015). To experimentally study such instabilities, 3D meniscus profiles need to be obtained at microscopic lengthscale and at microsecond temporal resolution. For this purpose a digital holographic microscope (DHM) was acquired. In the stroboscopic imaging mode the DHM is capable of making recordings as shown in Fig. 6.1, where axisymmetric modes are visible on the meniscus. In the same way non-axisymmetric modes, related to jetting angle errors, can be visualized. The recordings therefore demonstrate that the DHM can be a powerful tool for future investigations into the stability of an acoustically driven meniscus.

The measurements with the SWIR imaging setup in Chapter 3 have shown that multiple bubbles can be present after bubble entrainment. In preliminary experiments it was observed that for experiments with a single bubble per corner, the channel acoustics main frequency, measured using the piezo as sensor, depended on the number of bubbles and the bubble position, and not so much on the bubble radius or total bubble volume. It would be of interest to perform more detailed experiments to verify this observation and to explain this observation by developing an acoustic model of the ink channel that includes the effect that multiple entrained air bubbles and their locations have on the printhead acoustics.

The experiments with the experimental silicon-based printhead with glass nozzle plate in Chapter 4 have revealed that a vortical flow in front of the nozzle plays a crucial role in the stochastic bubble entrainment process. This vortical flow captures dirt particles that may at some point in time trigger bubble nucleation. Furthermore, it partly determines the convective flow trajectory and path of an entrained air bubble, and thereby has an influence on whether an entrained bubbles is ejected with droplet formation after a few actuation cycles, or whether it is permanently entrained. It would therefore be of great interest, both from fundamental and application point of view, to model this vortical flow and its interaction with an acoustically driven dirt particle and bubble. Such a model could be used both to study the relevant physical mechanism as well as to determine the ideal printhead design and operating parameters to prevent stochastic bubble entrainment. Preferably no dirt particles should be entrained in front of the nozzle, but at the same time any entrained bubble should be directed to return

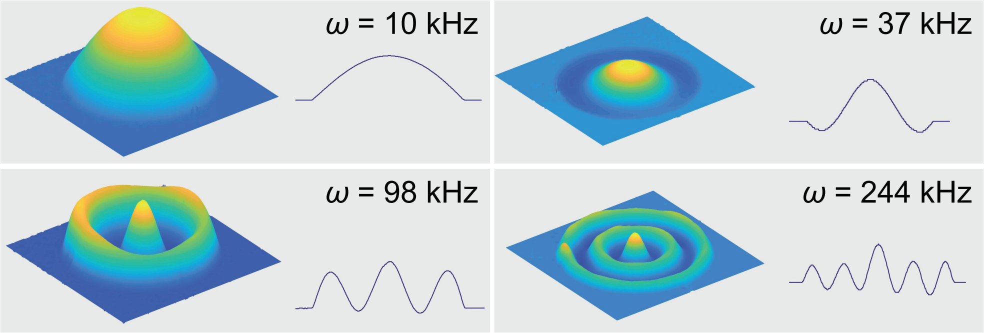

Figure 6.1: Stills from stroboscopic recordings by a reflection digital holographic microscope. The oscillating meniscus was recorded in a 70 µm diameter Microdrop inkjet nozzle (ADK-501) of which the piezo was driven by a low-amplitude sinusoidal waveform with frequencies ω indicated in the images. Each image shows the reconstructed 3D profile of the meniscus, and a 2D profile taken along a line through the center of this 3D profile.

to the nozzle as quickly as possible, so it that is ejected with droplet formation.

In addition to its use in the research on stochastic bubble entrainment, the experimental silicon-based printhead with glass nozzle plate opens a whole new world to the inkjet research. Processes in the nozzle and feedthrough that to date could only be studied numerically, are now accessible to experimental analysis. For example, the refill mechanism of the nozzle can be studied in more detail. This is of interest as under specific operating conditions the nozzle does not get sufficiently refilled, leading to gradual retraction of the meniscus into the nozzle over the course of several piezo actuations. Another example is selective evaporation of the more volatile, low-viscosity components in the ink in the nozzle when the jetting is temporarily halted. As a consequence a high-viscosity mixture forms in the nozzle that hinders droplet formation when the jetting is resumed. As a final example the glass nozzle printhead can be used to study the dynamics of the actuator in more detail. The glass nozzle plate enables direct optical access to the membrane in the ink chamber, and the dynamics of the membrane can be imaged and analyzed in detail and in-situ using the DHM.

The investigation on the secondary tail in Chapter 5 has revealed the formation of a cascade of even smaller tails. In future experimental studies such cascades could be further characterized by measuring the ratios between the tail diameters. If some trends are visible in these ratios, for example as function of meniscus motion or ink viscosity, this could further direct the research to the most relevant mechanisms involved. A necessary requirement for such experiments is that the tail diameters can be measured accurately. To increase this accuracy, a nozzle with a larger diameter could be used, or illumination with a shorter wavelength. To determine the relative influence of the mechanisms through which the meniscus motion and ink viscosity affect the process, numerical simulations need to be performed. Several numerical codes exist that can accurately model droplet formation, however, they should be two-way coupled to an acoustic model that describes the driving by the piezo actuation, and minute noise components should be introduced to finally describe the formation and breakup of the cascade of tails.

Summary

Piezo inkjet printing is used in high-end digital printers to deposit micron-sized droplets on-demand onto a substrate at high precision and reliability. The printing quality and reliability can be compromised by bubble entrainment and satellite formation. Bubbles that are entrained in the ink channel disturb or even stop droplet formation, and satellite droplets that are formed during the jetting process pollute the print and the printing machine. In this thesis bubble entrainment and satellite formation were experimentally visualized and characterized to investigate the underlying physical mechanisms.

In Chapter 2 bubble pinch-off from an acoustically driven meniscus in a printhead with a 70 μm diameter glass nozzle was studied for various acoustic driving waveforms. The piezo actuation pulse sets into motion a slosh mode of the printhead, resulting in a large amplitude meniscus motion with a frequency on the order of 10 kHz. It also actuates a piezo longitudinal resonance mode, which introduces a low-amplitude 100 kHz component to the meniscus motion. The slosh mode, piezo longitudinal resonance mode, and the falling edge of the rectangular piezo driving pulse destabilize the retracted concave meniscus when propelled outward, by jet formation due to a combination of geometrical focusing of the flow and an inhomogeneous pressure gradient field. Two well-timed outward accelerations of the meniscus result in the formation of a central jet surrounded by a toroidal jet. A phase mismatch of the oscillatory behavior of the two jets leads to the enclosure of an air cavity leading to bubble entrainment through pinch-off. It is shown that, next to pulse timing, the driving pressure is a control parameter of the entrainment process and that the threshold for bubble pinch-off can be increased by suppressing the piezo longitudinal resonance mode by waveform design.

In Chapter 3 entrained air bubbles were visualized in a micrometer scale ink channel inside a silicon chip of a MEMS-based piezo-acoustic inkjet printhead. As silicon is semi-transparent for optical imaging with shortwave infrared (SWIR) light, a highly sensitive SWIR imaging setup was developed which exploited the optical window of silicon at 1550 nm. Infrared recordings of entrained bubbles are presented, showing rich phenomena of acoustically driven bubble dynamics inside the printhead.

In Chapter 4 bubble entrainment, translation, and growth in an experimental silicon-based printhead with glass nozzle plate were studied using high-speed imaging

triggered by changes in the ink channel acoustics. The experimental printhead was produced using unconventional production methods, resulting in dirt particle polluted ink channels with a higher bubble entrainment probability than regular printheads. It was found that dirt particles trigger bubble nucleation upon their interaction with the oscillating meniscus. The entrained bubble was used as a sensitive pressure sensor with which channel pressure profiles could be measured, namely from fitting the measured radial bubble dynamics to the Rayleigh-Plesset equation. The ink jet length increase of 24% after bubble entrainment was shown to be a result of the bubble-induced decrease of the channel resonance frequency. We also traced the acoustically driven bubble inside the ink channel. It translates towards the channel wall due to a combination of acoustic radiation forces and convective ink flow. Next, the ink velocity field was characterized using particle tracking velocimetry. The vortical flow next to the oscillating meniscus was shown to trap dirt particles, thereby increasing the particle-to-meniscus interaction probability. Both cavitation on a particle during the rarefaction pressure wave and direct contact of a particle with the meniscus during fast advancement and retraction of the meniscus were identified as possible mechanisms through which bubbles can nucleate.

In Chapter 5 the role of the meniscus motion and ink viscosity on secondary tail formation and its breakup in the picoliter droplet formation process of a MEMS piezo-acoustic inkjet printhead were studied experimentally using single-flash stroboscopic imaging at a temporal resolution of 100 ns through 8 ns laser-induced fluorescence illumination. First a trapezoidal pulse and a multi-component pulse were compared to investigate the influence of the meniscus motion on the secondary tail and its satellites. The multi-component pulse produces an approximately four times larger meniscus retraction velocity during the lifetime of the secondary tail than the trapezoidal pulse, resulting in increased stretching and stabilization of the secondary tail. The maximum secondary tail length for the multi-component pulse was found to be 2.2 times larger than for the trapezoidal pulse, leading to a 3.0 times larger number of satellites. By increasing the length of the multi-component pulse, the retracting meniscus motion can be postponed and damped out which was shown to decrease the secondary tail length and thereby the total volume of secondary satellites. A further reduction in secondary satellite volume was achieved through a reduction of the ink viscosity, which decreased the mean satellite volume. Finally, a cascade of the secondary tail into a tertiary tail was observed for the first time in inkjet printing. The cascade results in a bimodal satellite size distribution, where the satellites with a volume ≥ 4 fL are located closer to the primary tail droplet, while satellites with a volume < 4 fL and are located closer to the nozzle.

Samenvatting

Piezo inkjet printen wordt gebruikt in high-end printers om on-demand en met grote nauwkeurigheid en betrouwbaarheid micrometer druppels te deponeren op een substraat. De kwaliteit en betrouwbaarheid van het printproces kunnen worden aangetast door het invangen van luchtbellen en de vorming van satellietdruppels. Ingevangen luchtbellen verstoren de druppelvorming en kunnen uitval van nozzles veroorzaken. Satellietdruppels vervuilen de afdrukken en de printer. Het invangen van luchtbellen en de vorming van satellietdruppels zijn in dit proefschrift op experimentele wijze zichtbaar gemaakt en gekarakteriseerd om onderliggende fysische mechanismen te onderzoeken.

In hoofdstuk 2 is de afsplitsing van een luchtbel vanaf een akoustisch aangedreven meniscus onderzocht in een printkop met een 70 µm diameter glazen nozzle. Dit is gedaan voor verschillende piezo-aandrijfpulsen. De piezo-aandrijfpuls slaat een klotsmodus van de printkop aan, wat leidt tot een 10 kHz meniscusbeweging met een grote amplitude. Daarnaast slaat het ook de lengtemodus van de piezo aan, welke een 100 kHz component met kleine amplitude toevoegt aan de meniscusbeweging. De klotsmodus van de printkop, lengtemodus van de piezo, en de neergaande flank van de rechthoekige aandrijfpuls destabiliseren de teruggetrokken holronde meniscus wanneer ze deze naar buiten versnellen. Deze destabilisatie is het gevolg van jetvorming door een combinatie van geometrische focussering van de vloeistofstroming en een niet-homogeen drukgradientveld. Twee goed getimede naar buiten gerichte versnellingen van de vloeistof leiden tot de vorming van een centrale jet, gevolgd door de vorming van een toroidale jet. Het faseverschil tussen de twee oscillerende jets leidt tot de insluiting van een luchtcaviteit en het invangen van een bel door afsplitsing de caviteit. Uit de metingen blijkt dat naast the timing van de aandrijfpuls ook de druk van de aandrijfpuls een controleparameter is voor het invangproces van de bel. Verder blijkt dat de drempel voor het afsplitsen van een bel verhoogd kan worden door de lengtemodus van de piezo te onderdrukken door middel van aanpassingen aan de aandrijfpuls.

In hoofdstuk 3 zijn ingevangen luchtbellen zichtbaar gemaakt in een micrometer groot inktkanaal in een silicum chip van een piezo-akoustische inkjetprintkop. Vanwege de semi-transparantie van silicum voor optische beeldvorming met infrarood licht van korte golflengte is er een beeldvorming opstelling ontwikkeld die zeer gevoelig is voor dit type infrarood licht met een golflengte van 1550 nm. De infraroodopnames van ingevangen bellen laten rijke fenomenen zien van akoustisch aangedreven bellen in de printkop.

In hoofdstuk 4 is het invangen, verplaatsen, en groeien van bellen bestudeerd in een experimenteel silicium printkop met glazen nozzleplaat. Hiervoor is gebruik gemaakt van hogesnelheidsbeeldvorming dat getriggerd werd door veranderingen in de akoustiek van het inktkanaal. Voor de productie van de experimentele printkop zijn onconventionele productiemethoden gebruikt, waardoor de inktkanalen veel vuildeeltjes bevatten en de kans op het invangen van luchtbellen veel groter was dan dat bij reguliere printkoppen. De metingen hebben laten zien dat vuildeeltjes het invangen van bellen triggeren door hun interactie met de oscillerende meniscus. De ingevangen bel is gebruikt als druksensor voor het meten van de drukprofielen in het inktkanaal door de radiële beldynamica te fitten aan de Rayleigh-Plesset vergelijking. De 24% toename van de druppellengte na het invangen van de bel was het gevolg van een afname van de resonantiefrequentie van het inktkanaal door de aanwezigheid van de bel. Het traject van de akoustisch aangedreven bel in het inktkanaal is ook in kaart gebracht. De bel verplaatste zich naar de kanaalwand onder invloed van een combinatie van akoustische stralingskrachten en convectieve inktstroming. Vervolgens is het inktsnelheidsveld gemeten met behulp van snelheidmeting door middel van het volgen van deeltjes (particle tracking velocimetry). De wervelende stroming naast de oscillerende meniscus vangt deeltjes in, en vergroot daarmee de kans op interactie tussen vuildeeltjes en de meniscus. Zowel cavitatie op een deeltje tijdens een akoustische verdunningsdrukgolf, als direct contact tussen een deeltje en de meniscus tijdens het snel heen en weer bewegen van de meniscus zijn mogelijke mechanismen voor nucleatie van een bel.

In hoofdstuk 5 zijn de rol van de meniscusbeweging en die van de inktviscositeit op de vorming en opbreking van de secundaire staart experimenteel bestudeerd tijdens picoliter druppelvorming van een piezo-akoustische inkjetprintkop. Hiervoor zijn stroboscopische opnames gemaakt met een tijdresolutie van 100 ns, gebruikmakend van 8 ns durende lichtflitsen van een lasergedreven fluorescente lichtbron. Eerst zijn een trapezium puls en een puls bestaande uit meerdere componenten vergeleken om de invloed van de meniscusbeweging op de secundaire staart en zijn satellieten te bestuderen. De terugtreksnelheid van de meniscus tijdens het bestaan van de secundaire staart is ongeveer vier keer zo groot voor de meerdere-componenten puls dan voor de trapezium puls. Dit zorgt voor een grotere oprekking en stabilisering van de secundaire staart bij de meerdere-componenten puls. De maximale secundaire staartlengte voor de meerdere-componenten puls was 2,2 keer groter dan die voor de trapezium puls, met als resultaat een 3,0 keer grotere hoeveelheid satellieten. Door middel van verlenging van de meerdere-componenten puls kan de terugtrekkende meniscusbeweging worden vertraagd en uitgedempt. Dit leidde tot kortere secundaire staart en een afname van het totale volume van de secundaire satellieten. Een verdere vermindering van het totale volume van de secundaire satellieten is bewerkstelligd door een verlaging van de inktviscositeit, welke het gemiddelde volume van secundaire satellieten verkleinde. Tot slot is voor het eerst in inkjet printen een cascade waargenomen van de secundaire staart naar een tertiaire staart. De cascade veroorzaakte een bimodale verdeling in de satelliet grootte verdeling, waarbij de satellieten met een volume ≥ 4 fL dichter bij de primaire staartdruppel gelegen zijn, en de satellieten met een volume < 4 fL dichter bij de nozzle gelegen zijn.

Acknowledgements

The work in this thesis is part of the research program ”High Tech Systems and Materials” (HTSM) with project number 12802, and part of the Industrial Partnership Program number i43, of the Dutch Technology Foundation (STW) and the Foundation for Fundamental Research on Matter (FOM), which are part of the Netherlands Organisation for Scientific Research (NWO). The research was co-financed by Océ Technologies B.V., University of Twente, and Eindhoven University of Technology. The work was carried out at the Physics of Fluids group of the Faculty of Science and Technology of the University of Twente, and at Océ Technologies B.V. in Venlo.

I would like to thank my promotors Michel and Detlef, and my assistant promotor Tim, for their outstanding guidance and support during my PhD. Thank you for the wise advices and detailed feedback on my work, and thank you for your personal approach which made me feel very welcome in the group. I very much enjoyed the opportunities to test and use the most advanced imaging toys in the world, such as the HPV-X2 camera with a maximum recording rate of 10 Mfps, and the Digital Holographic Microscope.

Also a big thanks to my supervisors/collaborators at Océ: Hans, Marc, Herman, Arjan, and Youri, who were always open to share their latest discoveries with me and have in depth discussions on the experimental methods and the physics. Furthermore a huge thanks to the technicians and engineers at Océ and Philips who assisted with the production of the experimental printheads, in particular Henk Simons, Norbert Lamers, Jos Lemmen, Henk Stolk, and Maikel Huygens from Océ and Theo Michielsen and Ton Nellissen from Philips. I also would like to thank all the other employees of Océ who helped me finding my way at Océ and provided me with new ideas, technical assistance, and feedback along the way, among which Igor Shklyarevskiy, Frans Blom, Tom Huijgen, Bert Morelissen, Koos Agricola, Jan Simons, Roel Heijnen, Willem-Jan van Harskamp, Robin Leus, Rob Koper, and Eelco Schillings. Also thanks to Wybo Wagenaar from Inifite for his Ansys-Fluent simulations on secondary tail formation.

I would like to thank my colleagues in the inkjet program for the great collaborations and interesting discussions. In particular I would like to thank my predecessor Mark-Jan for giving me a good start by taking me along with his experiments and visits to Océ. Furthermore I would like to thank Roger for sharing his knowledge during in depth discussions on possible physical explanations for my experimental observations.

I would like to thank Yaxing for the inspiring results on bubble entrainment. Finally, I would like to thank Maaike for the great experimental collaboration, and I wish her and Yogesh good luck on their PhD projects.

I am grateful to Wilco and Devaraj for introducing me to the boundary integral code and supporting me during the development of the numerical setups for my research. This code also led me to a collaboration with Álvaro Moreno Soto and Tom on coalescing bubbles*, and to one with Loreto and David on jet formation in a Needle-free injection system. Thank you for the nice collaboration and the great results. I also would like to thank Kees Venner and his students for the very interesting experimental collaboration on lubrication of bearings using inkjet printing.

The research would not have been possible without the help of the support staff. Great thanks to Bas for his help with the production of the electronic systems for the experimental setups, with configuring the servers on which I ran boundary integral simulations, and with ordering equipment. Also a great thanks to Gert-Wim and Martin for their help with the production of the experimental setups, and to Joanita for her help with the practical issues and administrative tasks surrounding the PhD.

The Physics of Fluids group is full of great minds with a great variety of skills. I would like to thank the Professors, Postdocs and PhDs who helped me building the experimental setups, testing new imaging systems, analysing data, running simulations, and understanding the physics. It was a great pleasure to work in such a rich environment. In particular I would like to thank my paranymphs Pascal and Robin. Pascal for being a mentor in many different situations, for his many practical advises in the lab, and for sharing his great amount of enthusiasm. Robin for sharing his knowledge on physics and software relevant to my research, and for the fun conversations during the many rides back to Tiel. Also a special thanks to Guillaume for all his help on solving experimental issues, and for the collaboration on researching acoustically driven bubbles and the collaboration on the testing of the Digital Holographic Microscope. Finally, a big thanks to my office mates and the lunch group who made my time at PoF a very pleasant one. Thanks for all the fun an interesting conversations.

Grote dank en liefde voor mijn familie die me door dik en dun hebben gesteund. Pap en Mam, bedankt dat ik altijd bij jullie terecht kon voor ondersteuning en advies. Bindikt en Beike, bedankt dat ik bij jullie mocht logeren in het begin van mijn PhD. Menno bedankt voor het delen van lief en leed van jou PhD-traject, en succes met de het leggen van de laatste hand aan jou promotie-onderzoek. Ik wil mijn schoonouders, Cor en Anja, bedanken voor de gastvrijheid die ik altijd op de boerderij heb mogen ervaren, en ik wil met name Anja bedanken voor de enorme ondersteuning de afgelopen jaren. Tot slot wil Janneke en Eliza bedanken voor de liefde die ik elke dag van ze mag ontvangen.

---

*Published as Á. Moreno Soto, T. Maddalena, A. Fraters, D. van der Meer, and D. Lohse, "Coalescence of diffusively growing gas bubbles", Journal of Fluids Mechanics **846**, 143-165 (2018)

About the author

Arjan Fraters was born on November 21st, 1987, in Wageningen, the Netherlands. He graduated from high school (Gymnasium) at ”Het Nieuwe Lyceum” in Bilthoven in 2006. In the same year he started studying Aerospace Engineering at the TU Delft. During his studies he was member of the student association Delft Aerospace Rocket Engineering (DARE), where he initiated and led a project on the design, production and testing of a hybrid rocket engine for the launch of the Stratos II rocket to 50 km altitude. Furthermore he worked at Advanced Lightweight Engineering (ALE) in Delft on the design of a dry filament wounded tank for the CHATT project, an EU project on the development of composite cryogenic tanks for hypersonic vehicles. In 2014 he received his master’s degree in the Space Engineering department on the ”Flooding limit and flame holding instability in high mass flux hybrid rocket engines”.[†] Thereafter he started his PhD research in the Physics of Fluids group, on the subject of bubble entrainment in piezo-acoustic inkjet printing . This project was supervised by Prof. dr. Michel Versluis, Prof. dr. Detlef Lohse, and Dr. Tim Segers, and was conducted in close cooperation with Océ Technologies B.V.

[†] Published as A. Fraters and A. Cervone, ”Experimental characterization of combustion instabilities in high-mass-flux hybrid rocket engines”, Journal of Propulsion and Power **32**, 958-966 (2016)